論文 / 著書情報
Article / Book Information

題目(和文)	初期太陽系における核合成起源 Sr・Nd 同位体不均質性
Title(English)	Nucleosynthetic Sr and Nd isotope heterogeneities in the early Solar System
著者(和文)	深井稜汰
Author(English)	Ryota Fukai
出典(和文)	学位:博士(理学), 学位授与機関:東京工業大学, 報告番号:甲第11058号, 授与年月日:2019年3月26日, 学位の種別:課程博士, 審査員:横山 哲也,中本 泰史,綱川 秀夫,奥住 聡,石川 晃
Citation(English)	Degree:Doctor (Science), Conferring organization: Tokyo Institute of Technology, Report number:甲第11058号, Conferred date:2019/3/26, Degree Type:Course doctor, Examiner:,,,,
学位種別(和文)	博士論文
Type(English)	Doctoral Thesis

Doctor thesis

Nucleosynthetic Sr and Nd isotope heterogeneities in the early Solar System

（初期太陽系における核合成起源 Sr・Nd 同位体不均質性）

Ryota FUKAI

Yokoyama laboratory

Department of Earth and Planetary Sciences

Tokyo Institute of Technology

Thesis summary

In Chapter 1, we review the background of (i) nucleosynthesis for trans-iron elements, (ii) carrier grains of trans-iron elements that contributed to the Solar System, and (iii) nucleosynthetic isotope anomalies observed in meteorites.

In Chapter 2, we have developed a technique that enables high-precision Nd isotopic analysis with thermal ionization mass spectrometry (TIMS) to detect nucleosynthetic isotope variability in whole-rock meteorites. To achieve high-precision analysis, we investigated the long-term fluctuation in high-precision Nd isotope measurements. Comprehensive measurements of a standard material JNdi-1 (n = 76) were conducted by applying three distinct methods (static, dynamic, and multistatic) during an eight-month analytical period. We found the dynamic method the most effective to minimize the influence of Faraday cup degradation, although a marginal isotopic shift was observed even for data obtained by the dynamic method throughout the entire analytical period. Our dynamic method allows to determine $^{142}Nd/^{144}Nd$, $^{148}Nd/^{144}Nd$, and $^{150}Nd/^{144}Nd$ ratios simultaneously. The reproducibilities of $^{142}Nd/^{144}Nd$, $^{148}Nd/^{144}Nd$, and $^{150}Nd/^{144}Nd$ ratios were ±4.1, ±6.3, and ±8.8 ppm (2 SDs), respectively, which are 1.5–4.1 times better than those obtained in previous studies.

In Chapter 3, we further investigated the secondary instrumental fractionation in TIMS instrument, which cannot be ignored in the extraordinary high-precision Nd isotope measurements. We performed multiple Nd isotope measurements (n = 125) for a standard material JNdi-1 with the dynamic method. We found small but resolvable fluctuations in the obtained $^{142}Nd/^{144}Nd$, $^{148}Nd/^{144}Nd$, and $^{150}Nd/^{144}Nd$ ratios of JNdi-1

that cannot be eliminated by the normal mass fractionation correction using the $^{146}Nd/^{144}Nd$ ratio, most likely due to the secondary instrumental fractionation induced by the accumulation of materials (e.g., H_3PO_4 activator) emitted from measured samples onto the surface of ion lens assemblage. The secondary instrumental fractionation observed in the $^{142}Nd/^{144}Nd$ ratio can be corrected using the simultaneously measured $^{150}Nd/^{144}Nd$ ratio. After the second-order correction, the reproducibilities of $^{142}Nd/^{144}Nd$ ratio have been improved from ±5.6 ppm to ±4.2 ppm (2 SDs).

In Chapter 4, we present high-precision Nd isotope compositions for whole-rock ordinary and carbonaceous chondrites determined with our method described in Chapters 2 and 3. The ordinary chondrites had uniform and non-terrestrial $\mu^{142}Nd$, $\mu^{148}Nd$, and $\mu^{150}Nd$ values, with data that plot along the mixing line between *s*-process endmember and terrestrial components in $\mu^{150}Nd$ versus $\mu^{148}Nd$, $\mu^{142}Nd$ versus $\mu^{148}Nd$, and $\mu^{142}Nd$ versus $\mu^{150}Nd$ diagrams. In contrast, the carbonaceous chondrites were characterized by larger anomalies in their $\mu^{142}Nd$, $\mu^{148}Nd$, and $\mu^{150}Nd$ values compared to ordinary chondrites. Importantly, the data for carbonaceous chondrites plot along the *s*-process and terrestrial mixing line in a $\mu^{150}Nd$ versus $\mu^{148}Nd$ diagram, whereas they have systematically lower $\mu^{142}Nd$ values than the *s*-process and terrestrial mixing line in $\mu^{142}Nd$ versus $\mu^{148}Nd$ and $\mu^{142}Nd$ versus $\mu^{150}Nd$ diagrams. This shift likely results from the incorporation of calcium- and aluminum-rich inclusions (CAIs), indicating that the Nd isotopic variability in the ordinary and CAI-subtracted carbonaceous chondrites was caused solely by the heterogeneous distribution of *s*-process nuclides. The Nd isotope dichotomy between bulk aliquots of ordinary and carbonaceous chondrites can be

related to the presence of Jupiter, which may have separated two isotopically distinct reservoirs that were present in the solar nebula. After correcting for *s*-process anomalies and CAI contributions to the Nd isotopes observed in the chondrites, we obtained a μ^{142}Nd value (−2.4 ± 4.8 ppm) that was indistinguishable from the terrestrial value. Our results corroborate the interpretation that a missing reservoir (e.g., a hidden enriched mantle reservoir, erosional loss of crust) is not required to explain the observed differences in ^{142}Nd/^{144}Nd ratios between chondrites and terrestrial materials.

In Chapter 5, we conducted high-precision Sr and Nd isotopic measurements for bulk aliquots of chondrites by applying a complete sample digestion technique. Our new high-precision data indicate that enstatite and ordinary chondrites possess uniform and small, but resolvable, Sr and Nd isotopic deviations from terrestrial rocks. In contrast, we found Sr isotopic variations across different classes of carbonaceous chondrites (CM, CO, and CV), of which the data points deviate from the *s*-process mixing line in the Sr–Nd isotopic space. This shift likely resulted from the incorporation of CAIs into carbonaceous chondrite parent bodies. The planetary-scale Sr and Nd isotopic heterogeneities among terrestrial rocks, enstatite, ordinary, and CAI-subtracted carbonaceous chondrites point to the heterogeneous distribution of *s*-process enriched materials in the early Solar System, which was most likely caused by the global nebular thermal processing. On the other hand, the Sr and Nd isotopic variation observed across CAI-subtracted carbonaceous chondrites cannot be explained solely by the nebular thermal processing. Rather, this isotopic variation was caused by the involvement of *s*-process-depleted silicate grains that repeatedly circulated in the early Solar System,

which were transferred and incorporated at varying degrees into the region where parent bodies of individual carbonaceous chondrites have formed. On the other hand, Sr and Nd isotopic compositions for CI chondrites were not explained by this disk evolutionary model, most likely due to the injection of supernovae materials and/or input of materials from the molecular cloud.

In Chapter 6, we introduce the future perspective on the issues that have been discussed in the previous chapters of this thesis.

Contents

Thesis summary 2

Chapter 1:
General introduction

1.1 Nucleosynthesis of trans-iron elements 11
1.1.1 *s*-process 12
1.1.2 *r*-process 14
1.1.3 *p*-process 16
1.2 Carrier grains of trans-iron elements 17
1.2.1 *s*-process carrier grains 18
1.2.2 *r*-process carrier grains 19
1.3 Nucleosynthetic isotope anomalies in meteorites 20
1.3.1 Oxygen isotope anomalies 20
1.3.2 Isotope anomalies of iron-peak elements (Ti, Cr, and Ni) 21
1.3.3 Isotope anomalies of trans-iron elements 22
1.3.4 Application of nucleosynthetic isotope anomalies 35
1.3.4.1 Taxonomy of meteorites 35
1.3.4.2 Tracking nebular processes 35
1.3.4.3 Decoding accretional history and building block of the planets 36
1.4 Objective of this thesis 37
References 39

Chapter 2:
Evaluation of the long-term fluctuation in isotope ratios measured by TIMS with the static, dynamic, and multistatic methods:
A case study for Nd isotope measurements

Abstract 52
2.1 Introduction 54
2.2 Experimental 57
2.2.1 Sample 57
2.2.2 Mass spectrometry 57
2.2.3 Data reduction 58
2.2.3.1 Static method 58
2.2.3.2 Dynamic method 59
2.3 Results and Discussion 63
2.3.1 Effect of Faraday cup deterioration in the static method 63
2.3.2 Comparison of the multistatic and dynamic methods 66
2.3.3 Isotopic shift in the dynamic method 72
2.3.4 Analytical reproducibilities of $^{148}Nd/^{144}Nd$ and $^{150}Nd/^{144}Nd$ ratios 75
2.4 Concluding remarks 78
References 80

Chapter 3:

Assessment of the secondary instrumental fractionation in TIMS: Implication for high-precision Nd isotope analysis of geochemical samples

Abstract 84
3.1 Introduction 85
3.2 Experimental 87
3.3 Results and Discussion 89
3.3.1 Fluctuation of Nd isotopic ratios obtained by the dynamic method 89
3.3.2 Covariation of $^{142}Nd/^{144}Nd$, $^{148}Nd/^{144}Nd$, and $^{150}Nd/^{144}Nd$ ratios 93
References 100

Chapter 4:

Neodymium isotope heterogeneity of ordinary and carbonaceous chondrites and the origin of non-chondritic ^{142}Nd compositions in the Earth

Abstract 102
4.1 Introduction 104
4.2 Experimental procedures 108
4.3 Results 114
4.3.1 Terrestrial samples 114
4.3.2 Ordinary and carbonaceous chondrites 116
4.4 Discussion 120
4.4.1 Ancient and recent redistributions of Nd and Sm in chondrites 120
4.4.2 Non-radiogenic Nd isotope anomalies in chondrites 122
4.4.3 μ^{142}Nd anomalies in chondrites 125
4.4.4 Origin of planetary-scale Nd isotope variability 130
4.4.5 Origin of non-chondritic ^{142}Nd/^{144}Nd ratios in terrestrial materials 133
4.5 Conclusion 136
References 138

Chapter 5:

Nucleosynthetic Sr–Nd isotope correlations in chondrites: Evidence for nebular thermal processing and dust transportation in the early Solar System

Abstract 146
5.1 Introduction 147
5.2 Experimental procedures 151
5.3 Results 156
5.3.1 Sr isotope measurements 159

5.3.1.1 Standard and terrestrial samples 159
5.3.1.2 Bulk chondrites 161
5.3.2 Nd isotope measurements 161
5.3.3 Concentration of trace elements 162
5.4 Discussion 163
5.4.1 Effect of terrestrial weathering to Sr isotopic measurements 164
5.4.2 Effect of acid digestion for presolar-grain-bearing samples 165
5.4.3 Correlation in Sr and Nd isotope anomalies 166
5.4.3.1 NCs 167
5.4.3.2 CCs 168
5.4.4 Nebular thermal processing and dust transportation 171
5.4.5 Isotopic anomalies of CI chondrites 176
5.5 Conclusion 179
References 181

Chapter 6:
Future perspective
6.1 Samples to investigate 190
6.2 Improvement of mass spectrometry 192
References 195

Conclusion **197**

Acknowledgment **199**

Chapter 1:
General introduction

This thesis focuses on the physical and chemical processes responsible for the evolution of the Solar System. These include the gravitational collapse of the molecular cloud core, transportation of materials in the solar nebula, and the formation of planets and planetesimals. Throughout this thesis, a specific emphasis is placed on the nucleosynthetic isotope anomalies recorded in meteorites that can be inferred from high-precision isotopic measurements for trans-iron elements in meteorites and their components. Here we introduce the basic information and knowledge about nucleosynthetic isotope anomalies in meteorites. First, we review stellar nucleosynthesis for trans-iron elements that occurred before the formation of the Solar System (Section 1.1). Secondly, we review dust grains formed after the stellar nucleosynthesis by which the synthesized trans-iron elements were delivered to the Solar System (Section 1.2). Finally, we review the results of observed nucleosynthetic isotopic anomalies among various planetary materials, especially for anomalies in trans-iron elements (Section 1.3), and suggest the objective of this thesis (Section 1.4).

1.1 Nucleosynthesis of trans-iron elements

The elements present in the Solar System have been formed via various nucleosynthetic reactions in the universe through the Galactic history. The elements that are heavier than Fe have been synthesized by neutron capture reaction (*s*- and *r*-processes); photo dissociation and/or proton capture reaction (*p*-process) (Burbidge et al., 1957) that occurred in stellar environments. The mechanism for *s*-, *r*-, and *p*-processes has been studied mainly based on the theoretical calculation and

observation for various stellar objects.

1.1.1 s-process

Slow neutron capture (*s*-process) is the dominant reaction of the nucleosynthetic process during Fe to Bi. In the *s*-process production, a seed nucleus (atomic number: Z, mass number: A) transforms to a heavier nucleus (atomic number: Z, mass number: A+1) by capturing a neutron. This process can be written as follows:

$$(Z, A) \rightarrow (Z, A+1) \rightarrow (Z, A+2) \rightarrow \ldots \qquad (1.1).$$

If (Z, A+2) is an unstable nucleus, β^- decay occurs to produce a nucleus with higher atomic number:

$$(Z, A+2) \rightarrow \beta^- \text{ decay} \rightarrow (Z+1, A+1) \rightarrow (Z+1, A+2) \rightarrow (Z+1, A+3) \rightarrow \ldots \qquad (1.2).$$

The abundances of nuclides produced by the *s*-process strongly depend on the neutron capture cross sections (σ). If (Z, A) has a large cross section, (Z, A+1) could be produced abundantly. Käppeler (1989) suggested that $\sigma \times N$ is generally constant in the most part of the *s*-process path (abundances of nuclei: N).

The *s*-process takes place in stars during the asymptotic giant branch (AGB) phase, the final evolutional part of low- to intermediate-mass stars ($0.1\ M_\odot \leq M \leq 8\ M_\odot$). Merrill (1952) observed the signature of an unstable element, Tc at the surface of AGB

stars, of which the isotopes are all short-lived nuclides and have been extinct in the present Solar System. This implies that the slow neutron capture reaction is ongoing in AGB stars. AGB stars have C/O core in the most inner part, surrounded by the H and He burning shells. In the intermediate of these two shells, another thin layer called the "^{13}C pocket" is evolved, which contains abundant ^{13}C synthesized by the reaction of ^{12}C + ^{1}H → ^{13}N → β^{+} decay → ^{13}C. In the ^{13}C pocket, neutrons (n) are generated via the process written below:

$$^{13}C + {}^{4}He \rightarrow {}^{16}O + n \qquad (1.3).$$

The generated neutrons react with heavy elements at the bottom of H and He burning shells during the "thermal pulse" stage that periodically occurs in AGB stars. Additionally, the convection called the "third dredge-up (TDU)" occurs in AGB stars, transferring the synthesized *s*-process elements to the surface of stars.

In the 1990s, the analytical precisions of neutron capture cross sections for isotopes around magic nuclei (N = 82) were improved by ~10 times. Based on the current cross section data and theoretical model accounting for the distribution of neutron exposures that occurred in general AGB stars (stellar model: Gallino et al., 1998), Arlandini et al. (1999) developed a new database for *s*-process abundances, which successfully explains the *s*-process relative abundances of Solar System (Anders and Grevesse, 1989) as well as the isotopic compositions of trans-iron elements in presolar grains, considered that the grains derived from AGB stars (Section 1.2). More

recently, the abundances of *s*-process nuclides and their contribution to the Solar System composition have been updated by Bisterzo et al. (2011), in which the galactic chemical evolution model by Travaglio et al. (2004), elements abundances in the Solar System updated by Lodders et al. (2009), and recent neutron cross sections derived from Karlsruhe Astrophysical Database of Nucleosynthesis in Stars (KaDONIS) database are included. The model by Bisterzo et al. (2011) was further updated by including the newly suggested galactic chemical evolution model, the dependence for the mass of AGB stars (low or intermediate), and the theory of branching points in *s*-process path (Bisterzo et al., 2014, 2015).

1.1.2 r-process

In contrast to the *s*-process, the explosive rapid neutron capture process is called the *r*-process. This process is a chain reaction in which successive neutron captures occur faster than the timescale of β^- decay, making it possible to synthesize the heaviest nuclides of Th and U. The solar abundances of *r*-process nuclides have been calculated by subtracting the abundances of *s*-process nuclides from those of the Solar System average (*r*-residual method: Arlandini et al., 1999). Although the *r*-process abundances have not been calculated directly by theoretical methods, the elemental abundances of *r*-nuclides estimated by this approach are in good agreement with those of old, low-metallicity stars where the contribution for *s*-process nucleosynthesis can be ignored (*r*-process universality: Sneden et al., 1996).

The nucleosynthetic sites for the *r*-process are still controversial. One of the

plausible candidates is the core-collapse supernova of massive stars (> 8 $M_{\odot}$). In this situation, high temperature and high density in the shock wave launched by core-collapse supernova could induce explosive *r*-process reaction with abundant neutrons. However, some theoretical models predict that core-collapse supernovae would not synthesize nuclides heavier than A = ~130 due to the reaction that consume neutrons by the reaction with electron neutrino (e.g., Wanajo, 2013). Alternatively, the magnetically rotational core-collapse supernovae were suggested as a candidate for *r*-process site in the early age of Galactic history (e.g., Nishimura et al., 2015).

Apart from core-collapse supernovae, the neutron star mergers have now become a potential nucleosynthetic site for heavy *r*-process nuclides (e.g., Argast et al., 2004). The observation of dwarf galaxies supported the production of heavy *r*-process nuclides by neutron star mergers (Tsujimoto et al., 2014). Because neutron star mergers are relatively rare processes in the galaxies, this phenomenon hardly occurred in dwarf galaxies. In fact, the deficits of *r*-process nuclides relative to the Solar System abundances were observed in this dwarf galaxy, suggesting that neutron star mergers are one of the hosts of *r*-process production. More recently, observations for the neutron star merger associated with the detection of gravitational wave were performed, suggesting the occurrence of *r*-process nucleosynthesis in neutron star merger events (e.g., Kasen et al., 2017). In more detail, the accompanied wave by the radiogenic decay of short-lived nuclei (kilonova) could provide the elemental abundances for heavy *r*-process nuclides.

1.1.3 p-process

Some heavy isotopes relatively enriched in protons (e.g., ^{92}Mo, ^{144}Sm, ^{180}Ta) could not be synthesized by the *s*- and *r*-processes. These isotopes are called "*p*-process" nuclides, of which *p* has a double meaning of "proton-captures" and "photo dissociation". The dominant reaction synthesizing the *p*-process nuclides is the *γ*-process (photo dissociation). In the *γ*-process, the seed nuclei synthesized via the *s*- and *r*-processes are irradiated by photons and then protons or neutrons are expelled from the nuclei. The *γ*-process most likely occurs during H and He burning shells in massive stars during core-collapse supernovae or thermonuclear supernovae (e.g., Rauscher e al., 2013).

However, a part of *p*-process nuclides synthesized by *γ*-process were underestimated to the isotopic abundances for the Solar System. The alternative process is proton capture reaction, including the *rp*-process, *pn*-process, and *νp*-process occurring in neutron stars and white dwarfs. Of these reactions, *rp*-process could not form the isotopes heavier than ^{130}Te, due to the shortage of reaction energy. In contrast, *pn*-process and *νp*-process could go through this stagnant point for the proton capture processes.

1.2 Carriers of trans-iron elements

In the universe, 92 elements are synthesized via various nucleosynthetic processes. In particular, trans-iron elements have been synthesized by the processes of neutron capture, photo dissociation, and proton capture (Section 1.1) before the formation of the Solar System. Tiny grains condensed at the end of the lifetime of stars (e.g., AGB stars, supernovae) reflect the consequence of nucleosynthetic processes occurred in the individual stellar environments. The Solar System integrated these grains during the early phase of its formation. The grains have been generally destroyed in the protoplanetary disk and subsequently condensed into new mineral phases as the temperature of nebular gas decreased. However, grains brought from the presolar stellar sites have been observed in some primitive meteorites (presolar grains).

Silicon carbide (SiC) is one of the most studied presolar grains at present. Because SiC grains have highly acid-resistant characteristics, the grains could be extracted as the residual materials of primitive meteorites during acid digestion protocols (Amari et al., 1994). Previous studies on presolar SiC grains reported isotopic compositions of major constituent elements (C and Si: compiled in Hynes and Gyngard, 2009) and noble gases (Ne, Kr, and Xe: e.g., Lewis et al., 1994). A series of studies on the isotopic compositions of presolar SiC grains have discovered that grains can be classified into several groups including mainstream, type-X, type-Y, type-Z, type-A+B, and nova origin.

Presolar graphite and diamond were firstly found in the separation protocols for the extraction of SiC grains (Amari et al., 1994). In contrast, presolar oxide, silicate, and

silicon nitride (Si_3N_4) were identified by the isotopic measurements for each mineral included in meteorites, due to the extremely different isotopic compositions from the other planetary materials. Presolar oxide grains (e.g., spinel, hibonite, corundum) were extensively identified by oxygen isotopic measurements and classified into four groups. Presolar silicate grains were most abundant presolar grains in meteorites, however, their isotopic compositions and structures were difficult to determine because the size of most presolar silicate grains are too small to perform isotopic analysis.

1.2.1 s-process carrier grains

The mainstream SiC grains found in primitive meteorites account for 90% of all types of presolar SiC. According to the results of spectroscopic observations regarding C and N isotope ratios, the mainstream SiC grains have been synthesized in the carbon-rich low-mass AGB stars (e.g., Lambert et al., 1986; Smith and Lambert, 1990). Consequently, the mainstream SiC has been considered as the major carrier of *s*-process nuclides contributed to the early Solar System. The isotopic analyses of heavy elements in mainstream SiC show clear excesses of *s*-process nuclides (e.g., Zinner et al., 1991; Yin et al., 2006). Furthermore, the isotopic ratios are consistent with the results of the theoretical calculations assuming *s*-process nucleosyntheses on low-mass AGB stars (e.g., Arlandini et al., 1999). Although the other types of SiC grains (type-Y, type-Z, and type-A+B) have been synthesized in AGB stars as well as the mainstream SiC, the stellar environments that formed these minor grains are considered to have different stellar metallicity from the sites producing mainstream SiC (Hoppe et al., 1998).

On the other hand, most of the presolar oxide grains are considered to be of AGB stars origin defined by the oxygen isotopic measurements, although there is no direct evidence of *s*-process carriers due to the absence of isotopic data for trans-iron elements in these grains.

1.2.2 r-process carrier grains

Unlike the case of mainstream SiC, presolar grains of *r*-process carriers have not been studied extensively. The type-X SiC grains were condensed most likely in supernovae, whereas the other types of SiC grains except for nova grains are considered to be originated from AGB stars. The type-X SiC show significantly different C, N, and Si isotopic compositions from the other types of SiC grains (Hynes and Gyngard, 2009). In addition, the Zr and Mo isotopic compositions for type-X SiC show the excess of *r*-process nuclides compared to the Solar System (Nicolussi et al., 1998).

A part of presolar oxides (corundum and spinel) possess isotopic signatures (e.g., O) that suggest the supernovae origin (e.g., Nittler et al., 1998; Gyngard et al., 2010). Low-density (LD) graphite grains also indicate their supernovae origin, supported by the excess of ^{44}Ti (radiogenic nuclei from ^{44}Ca) that were originated most likely from the nucleosynthetic processes in supernovae (Hynes and Gyngard, 2009). However, isotopic measurements for trans-iron elements in presolar oxide and graphite are limited. Therefore, it cannot be concluded that these grains have brought *r*-process nuclides to the Solar System.

1.3 Nucleosynthetic isotope anomalies in meteorites

A variety of submicron-size dust grains, produced before the onset of the Solar System formation (4.56 Ga) in different stellar environments, have contributed to the Solar System. The grains of different stellar origin evidently have diverse isotopic composition for most of the elements in the periodic table. Most of these grains have been destroyed via physicochemical processes (e.g., evaporation, condensation) in the protoplanetary disk and thoroughly mixed, resulting in isotopically homogeneous Solar System (e.g., Clayton et al., 1988). Nevertheless, bulk aliquots of chondrites, achondrites, and iron-meteorites possess distinct isotopic compositions for various heavy elements compared to those in bulk Earth. Although mass-dependent isotopic fractionation could be induced by various event including the evaporation and condensation in the molecular cloud and the protoplanetary disk, the observed variability of isotopic compositions for heavy elements in meteorites was caused by mass-independent isotopic fractionation due to the involvement of nucleosynthetic components that have been heterogeneously distributed in the early Solar System. We generally call this isotopic variation as "(nucleosynthetic) isotope anomaly".

1.3.1 Oxygen isotope anomalies

In addition to trans-iron elements, oxygen is known to show variable isotopic compositions in meteorites and their components that cannot be explained solely by mass-dependent isotopic fractionation (e.g., Clayton, 1993; Clayton and Mayeda, 1996; 1999). In the $^{17}O/^{16}O$ versus $^{18}O/^{16}O$ plots, both mass-dependent and mass-independent

isotopic fractionations can be observed. The terrestrial fractionation line (TFL) indicates the mass-dependent fractionation of the terrestrial O composition. The distance from the TFL (i.e., $\Delta^{17}O$) represents the extent of mass-independent isotopic fractionation. According to this plot, chondrites could be classified into several groups with $\Delta^{17}O > 0$ (ordinary chondrites), $\Delta^{17}O < 0$ (most of carbonaceous chondrites), and $\Delta^{17}O = \sim 0$ (enstatite chondrites, CI chondrites, and CM-CI mixture chondrites). It should be noted that carbonaceous chondrites possess $\Delta^{17}O$ variations across their subgroups (CI, CR, CM, CO, CV, CK, CB, and CH). The mass-independent O isotopic variation is most likely due to the existence of refractory components (calcium- and aluminum-rich inclusions (CAIs) and chondrules) residing specifically in carbonaceous chondrites, which have variable O isotope anomalies among single meteorites. The cause of O isotope anomalies has been implicated to the self-shielding effect of ultra-violet ray occurring in the early Solar System (Yurimoto and Kuramoto, 2004), rather than the involvement of various nucleosynthetic components. Because this effect depends on the distance from the central star, O isotopic variation could reflect the radial distribution of the parent bodies in the protoplanetary disk.

1.3.2 Isotope anomalies of iron-peak elements (Ti, Cr, and Ni)

Precise isotopic analyses conducted by new-generation (2005-) multicollector-inductively coupled plasma-mass spectrometry (MC-ICP-MS) and thermal ionization mass spectrometry (TIMS) instruments have contributed to detect nucleosynthetic isotopic anomalies in trans-iron elements including iron-peak elements (Ti, Cr, and Ni).

One of the most remarkable studies is high-precision Cr isotopic analysis for various types of meteorites. Well-resolved results of Cr isotopic measurements could discriminate different types of chondrites (carbonaceous chondrites, ordinary chondrites, and enstatite chondrites), as well as achondrites, iron-stony meteorites, and iron meteorites (Trinquier et al., 2007). The observed Cr isotopic anomalies within different types of meteorites have been induced most likely by the heterogeneous distribution of presolar tiny Cr-spinel grains within the protoplanetary disk (Dauphas et al., 2010; Qin et al., 2011). Other iron peak elements (Ti and Ni) also exhibit planetary-scale isotopic heterogeneities in bulk chondrites and differentiated meteorites (e.g., Regelous et al., 2008; Trinquier et al., 2009).

1.3.3 Isotope anomalies of trans-iron elements

Nucleosynthetic isotope anomalies of trans-iron elements, synthesized via the *s*-, *r*-, and *p*-processes, have been reported in various previous studies. Here we review the results of high-precision isotopic measurements of cosmochemical materials (bulk chondrites, bulk differentiates meteorites, and their components) for trans-iron elements; (i) Sr, (ii) Zr, (iii) Mo, Ru, and Pd, (iv) Te, (v) Ba, (vi) Nd and Sm, (vii) Hf, (viii) W, and (ix) Os and Pt. Throughout this chapter, the isotope ratios for meteorite samples are reported in μ notation, which represents part per 10^6 deviations from the mean values of terrestrial standards ($\mu^iM = (R_{sample}/R_{standard} - 1) \times 10^6$, $R = {}^iM/{}^jM$). The relative abundances of isotopes and the proportion to isotopes from three nucleosynthetic sources (*s*-, *r*-, and *p*-processes) were denoted in Table 1.1.

Table 1.1 *Relative abundances and proportion from three nucleosynthetic sources (s-, r-, and p-processes) of isotopes (modified from Arlandini et al., 1999).*

Isotopes	Relative abundances (%)	*s*-process (%)	*r*-process (%)	*p*-process (%)
^{84}Sr	0.56	0	0	100
^{86}Sr	9.86	47	0	-
^{87}Sr	7.00	50	0	-
^{88}Sr	82	92–100	-	-
^{90}Zr	51.45	72	28	0
^{91}Zr	11.22	96	4	0
^{92}Zr	17.15	93	7	0
^{94}Zr	17.38	100	0	0
^{96}Zr	2.80	55	-	-
^{92}Mo	14.77	0	0	100
^{94}Mo	9.23	1	0	99
^{95}Mo	15.90	55	45	0
^{96}Mo	5.54	100	0	0
^{97}Mo	9.56	59	41	0
^{98}Mo	24.19	76	24	0
^{100}Mo	9.67	4	96	0
^{98}Ru	1.87	0	0	100
^{99}Ru	12.76	28	72	0
^{100}Ru	12.60	95	0	5
^{101}Ru	17.06	15	85	0
^{102}Ru	31.55	43	57	0
^{104}Ru	18.62	3	97	0
^{102}Pd	1.02	0	0	100
^{104}Pd	11.14	100	0	0
^{105}Pd	22.33	14	86	0
^{106}Pd	27.33	51	49	0
^{108}Pd	26.46	65	35	0
^{110}Pd	11.72	4	96	0

Table 1.1 *Continued.*

Isotopes	Relative abundances (%)	*s*-process (%)	*r*-process (%)	*p*-process (%)
^{120}Te	0.09	0	0	100
^{122}Te	2.55	88	0	12
^{123}Te	0.89	89	0	11
^{124}Te	4.74	91	0	9
^{125}Te	7.07	20	80	0
^{126}Te	18.84	40	60	0
^{128}Te	31.74	2	98	0
^{130}Te	34.08	0	100	0
^{130}Ba	0.11	0	0	100
^{132}Ba	0.10	0	0	100
^{134}Ba	2.42	98	0	2
^{135}Ba	6.59	26	74	0
^{136}Ba	7.85	100	0	0
^{137}Ba	11.23	65	35	0
^{138}Ba	71.70	86	14	0
^{136}Ce	0.19	0	0	100
^{138}Ce	0.25	0	0	100
^{140}Ce	88.45	84	17	0
^{142}Ce	11.11	22	78	0
^{142}Nd	27.2	92	0	8
^{143}Nd	12.2	32	68	0
^{144}Nd	23.8	51	49	0
^{145}Nd	8.3	28	72	0
^{146}Nd	17.2	64	36	0
^{148}Nd	5.7	19	81	0
^{150}Nd	5.6	0	100	0

Table 1.1 *Continued.*

Isotopes	Relative abundances (%)	*s*-process (%)	*r*-process (%)	*p*-process (%)
^{144}Sm	3.07	0	0	100
^{147}Sm	14.99	21	79	0
^{148}Sm	11.24	97	0	3
^{149}Sm	13.82	13	88	0
^{150}Sm	7.38	100	0	0
^{152}Sm	26.75	23	77	0
^{154}Sm	22.75	1	99	0
^{152}Gd	0.2	9	0	91
^{154}Gd	2.18	95	0	5
^{155}Gd	14.8	6	94	0
^{156}Gd	20.47	17	83	0
^{157}Gd	15.65	11	89	0
^{158}Gd	24.84	27	73	0
^{160}Gd	21.86	1	99	0
^{156}Dy	0.06	0	0	100
^{158}Dy	0.09	0	0	100
^{160}Dy	2.33	87	0	13
^{161}Dy	18.89	6	94	0
^{162}Dy	25.47	16	84	0
^{163}Dy	24.9	4	96	0
^{164}Dy	28.26	24	76	0
^{162}Er	0.14	0	0	100
^{164}Er	1.6	83	0	17
^{166}Er	33.5	15	85	0
^{167}Er	22.87	9	91	0
^{168}Er	26.98	28	72	0
^{170}Er	14.91	7	93	0

Table 1.1 *Continued.*

Isotopes	Relative abundances (%)	*s*-process (%)	*r*-process (%)	*p*-process (%)
^{168}Yb	0.13	0	0	100
^{170}Yb	3.04	100	0	0
^{171}Yb	14.28	14	86	0
^{172}Yb	21.83	30	70	0
^{173}Yb	16.13	21	79	0
^{174}Yb	31.83	50	50	0
^{176}Yb	12.76	14	86	0
^{174}Hf	0.16	0	0	100
^{176}Hf	5.26	96	0	4
^{177}Hf	18.6	18	82	0
^{178}Hf	27.28	57	43	0
^{179}Hf	13.62	37	63	0
^{180}Hf	35.08	75	25	0
^{180}W	0.12	5	0	95
^{182}W	26.50	46	54	0
^{183}W	14.31	54	46	0
^{184}W	30.64	71	29	0
^{186}W	28.43	50	50	0
^{184}Os	0.02	0	0	100
^{186}Os	1.59	97	0	3
^{187}Os	1.96	82	0	18
^{188}Os	13.24	19	81	0
^{189}Os	16.15	4	95	0
^{190}Os	26.26	12	88	0
^{192}Os	40.78	1	99	0

Table 1.1 *Continued.*

Isotopes	Relative abundances (%)	*s*-process (%)	*r*-process (%)	*p*-process (%)
^{190}Pt	0.014	0	0	100
^{192}Pt	0.782	98	0	2
^{194}Pt	32.97	4	96	0
^{195}Pt	33.83	2	98	0
^{196}Pt	25.24	10	90	0
^{198}Pt	7.163	0	100	0

(i) Strontium

The lightest element produced exclusively in the *s*-, *r*-, and *p*-processes is Sr. Strontium has four stable isotopes (^{84}Sr, ^{86}Sr, ^{87}Sr, and ^{88}Sr), which are synthesized via the *p*-process (^{84}Sr), *s*-process (^{86}Sr, ^{87}Sr, and ^{88}Sr), and *r*-process (^{88}Sr). Weak *s*-process, occurring in the presupernovae phases of massive stars (> 8 $M_{\odot}$), also contributes to the synthesis for ^{86}Sr, ^{87}Sr, and ^{88}Sr. Andreasen and Sharma (2006) provided first results on Sr isotope anomalies (μ^{84}Sr) in carbonaceous chondrites, an ordinary chondrite, and an eucrite. Carbonaceous chondrites (Allende and Murchison meteorites) represented Sr isotopic compositions deviated from the terrestrial standard. Subsequent studies have reported Sr isotopic anomalies in CAIs, an ungrouped achondrite (NWA 2736), and other types of carbonaceous chondrites (Moynier et al., 2012; Hans et al., 2013; Paton et al., 2013; Yokoyama et al., 2015). The results of acid-leaching experiments indicate the extreme *s*-process enrichment in acid residual phases in primitive carbonaceous chondrites (Qin et al., 2011; Paton et al., 2013; Yokoyama et al., 2015). Previous works and the background on Sr isotope anomalies

are reviewed in Section 5.1 in more detail.

(ii) Zirconium

Zirconium is one of the most refractory elements. Zirconium has five stable isotopes (^{90}Zr, ^{91}Zr, ^{92}Zr, ^{94}Zr, and ^{96}Zr). Zr isotopes are mainly synthesized via the stellar nucleosynthesis of the *s*- and *r*-processes. Only ^{96}Zr is originated from multiple nucleosynthesis sources such as *s*- and *r*-processes, *p*-process in thermonuclear supernovae, neutron bursts in core-collapse supernovae, and lighter element particle process (LEPP) occurring in all massive stars (> 8 $M_{\odot}$). Due to its high-ionization potential, the isotopic analysis of Zr is difficult to perform with TIMS. Therefore, high-precision Zr isotope measurements were developed with ICP-MS (Schönbachler et al., 2004). Akram et al. (2013) performed a pioneering study for Zr isotope measurements for meteoritical samples (bulk carbonaceous chondrites and CAIs). CAIs extracted from carbonaceous chondrites showed the greatest extent of Zr isotope anomalies among bulk chondrites and their components. Subsequently, Akram et al. (2015) reported comprehensive data of Zr isotope anomalies in a variety of cosmochemical samples (All types of carbonaceous chondrites except for CH type, ordinary chondrites, enstatite chondrites, eucrites, and chondritic components). Whereas μ^{91}Zr and μ^{92}Zr were identical to terrestrial standards, a part of bulk carbonaceous chondrite samples represented positive μ^{96}Zr values.

(iii) Molybdenum, ruthenium, and palladium

Molybdenum, Ru, and Pd are characterized as siderophile (or highly siderophile) elements. Molybdenum has seven stable isotopes (^{92}Mo, ^{94}Mo, ^{95}Mo, ^{96}Mo, ^{97}Mo, ^{98}Mo, and ^{100}Mo) and Ru has seven stable isotopes (^{96}Ru, ^{98}Ru, ^{99}Ru, ^{100}Ru, ^{101}Ru, ^{102}Ru, and ^{104}Ru). These isotopes are synthesized via stellar nucleosynthesis of the *p*-process (^{92}Mo, ^{94}Mo, ^{96}Ru, and ^{98}Ru), *s*-process (^{94}Mo, ^{95}Mo, ^{96}Mo, ^{97}Mo, ^{98}Mo, ^{99}Ru, ^{100}Ru, ^{101}Ru, and ^{102}Ru), and *r*-process (^{95}Mo, ^{97}Mo, ^{98}Mo, ^{100}Mo, ^{99}Ru, ^{100}Ru, ^{102}Ru, and ^{104}Ru). High-precision Mo and Ru isotope analyses of cosmochemical samples have been conducted both by TIMS and MC-ICP-MS. Burkhardt et al. (2011) developed the analytical technique of the Mo isotope measurements with MC-ICP-MS and provided comprehensive data for Mo isotope compositions of various types of meteorites. More recently, the existence of fundamental "isotopic dichotomy" (Section 1.3.4) between carbonaceous chondrites and other types of meteorites (non-carbonaceous meteorites) was found in the diagram of Mo isotopes (e.g., μ^{94}Mo versus μ^{95}Mo), which was interpreted as the presence of separated Mo isotope reservoirs in the early Solar System (Budde et al., 2016; Kruijer et al., 2017). This observation was confirmed by subsequent studies published by the other research groups (Poole et al., 2017; Worsham et al., 2017).

Nucleosynthetic Ru isotope anomalies were also observed in most of bulk meteorites (Chen et al., 2010; Fischer-Gödde et al., 2015; Fischer-Gödde and Kleine, 2017). Dauphas et al. (2004) found that isotope anomalies in the Mo and Ru compositions are well-correlated among bulk chondrites and iron meteorites. This correlation well matches the theoretically predicted nucleosynthetic slopes in *s*-process

(e.g., Arlandini et al., 1999). Recently, Bermingham et al. (2018) refined these isotopic measurements for iron meteorites with the correction of the cosmic-ray exposures. Additionally, the Pd isotope measurements were developed with MC-ICP-MS, however, there are still limited number of reports on Pd isotope compositions in meteorites (Mayer et al., 2015; Ek et al., 2017).

(iv) Tellurium

Tellurium is classified as moderately volatile and chalcophile element. Tellurium has eight stable isotopes (^{120}Te, ^{122}Te, ^{123}Te, ^{124}Te, ^{125}Te, ^{126}Te, ^{128}Te, and ^{130}Te). Tellurium isotopes are produced by stellar nucleosynthesis of the *p*-process (^{120}Te), *s*-process (^{122}Te, ^{123}Te, ^{124}Te, ^{125}Te, and ^{126}Te), and *r*-process (^{125}Te, ^{126}Te, ^{128}Te, and ^{130}Te). Tellurium isotope compositions of bulk meteorites were first reported by Fehr et al. (2004). Whereas bulk meteorites (chondrites and differentiated meteorites) possess no resolvable Te isotopic anomalies (Fehr et al., 2004; Fehr et al., 2006; Fukami et al., 2014), presolar nanodiamond grains from carbonaceous chondrites show isotopic anomalies, which may have been produced by the neutron burst in supernovae (Richter et al., 1998; Maas et al. 2001).

(v) Neodymium and samarium

Neodymium and samarium are lithophile elements that belong to rare-earth elements (REEs). Neodymium has seven isotopes (^{142}Nd, ^{143}Nd, ^{144}Nd, ^{145}Nd, ^{146}Nd, ^{148}Nd, and ^{150}Nd) and Sm has seven isotopes (^{144}Sm, ^{147}Sm, ^{148}Sm, ^{149}Sm, ^{150}Sm, ^{152}Sm,

and ^{154}Sm). These isotopes are synthesized via stellar nucleosynthesis of the *p*-process (^{142}Nd and ^{144}Sm), *s*-process (^{142}Nd, ^{143}Nd, ^{144}Nd, ^{145}Nd, ^{146}Nd, ^{148}Nd, ^{147}Sm, ^{148}Sm, ^{149}Sm, ^{150}Sm, ^{152}Sm, and ^{154}Sm), and *r*-process (^{143}Nd, ^{144}Nd, ^{145}Nd, ^{146}Nd, ^{148}Nd, ^{150}Nd, ^{147}Sm, ^{149}Sm, ^{150}Sm, and ^{154}Sm). Boyet and Carlson (2005) first reported that bulk chondrites possess negative μ^{142}Nd values about –20 ppm. It should be noted that the isotopic anomalies could be caused both by the results of the radiogenic decay from short-lived ^{146}Sm and nucleosynthetic origins. Carlson et al. (2007) conducted additional Nd isotopic measurements for bulk carbonaceous chondrites, showing the existence of nucleosynthetic Nd variability among bulk chondrites. Previous works and the background on Nd isotope anomalies are reviewed in Section 4.1 in more detail. On the other hand, Andreasen and Sharma (2006) reported Sm isotopic anomalies for the *p*-process nuclide (^{144}Sm) in bulk Allende (CV) and Murchison (CM) meteorites, although the authors concluded that *s*- and *r*-processes Sm nuclides were homogeneously distributed among bulk chondrites and terrestrial rocks.

(vi) Barium

Barium is a lithophile element and relatively abundant in geochemical and cosmochemical samples. Barium has seven isotopes (^{130}Ba, ^{132}Ba, ^{134}Ba, ^{135}Ba, ^{136}Ba, ^{137}Ba, and ^{138}Ba) synthesized via the *p*-process (^{130}Ba and ^{132}Ba), *s*-process (^{134}Ba, ^{135}Ba, ^{136}Ba, ^{137}Ba, and ^{138}Ba), and *r*-process (^{135}Ba, ^{137}Ba, and ^{138}Ba). Because Ba is a typical *s*-process dominant element, Ba is a promising tracer for detecting the *s*-process nucleosynthesis sites in astronomical observations. Ranen and Jacobsen (2006) first

reported Ba isotope anomalies in bulk carbonaceous chondrites, whereas subsequent studies (Andreasen and Sharma, 2007; Carlson et al., 2007) showed that the extent of Ba anomalies in bulk meteorites was lower than were previously reported. These inconsistencies may be due to the incomplete acid digestion of presolar grains bearing chondrite samples. Subsequently, Bermingham et al. (2016) performed complete acid digestion for chondrite samples, suggesting only a part of carbonaceous chondrites possesses Ba isotopic anomalies.

(vii) Hafnium

Hafnium is known as a lithophile and refractory element. Hafnium has six stable isotopes (^{174}Hf, ^{176}Hf, ^{177}Hf, ^{178}Hf, ^{179}Hf, and ^{180}Hf). Hafnium isotopes are synthesized via the stellar nucleosynthesis of the *p*-process (^{174}Hf and ^{176}Hf), *s*-process (^{176}Hf, ^{177}Hf, ^{178}Hf, ^{179}Hf, and ^{180}Hf), and *r*-process (^{177}Hf, ^{178}Hf, ^{179}Hf, and ^{180}Hf). Sprung et al. (2010) showed that Hf isotope compositions of bulk meteorites were identical to terrestrial standards. Peters et al. (2017) reported intriguing results for the existence of Hf isotope anomalies in a minor *p*-process nuclides (^{174}Hf) only for CAIs extracted from carbonaceous chondrites.

(viii) Tungsten

Tungsten is a moderately siderophile element. Tungsten has five stable isotopes (^{180}W, ^{182}W, ^{183}W, ^{184}W, and ^{186}W). Tungsten isotopes are synthesized via the stellar nucleosynthesis of the *p*-process (^{180}W) and *s*- and *r*-processes (^{182}W, ^{183}W, ^{184}W, and

^{186}W). Kleine et al. (2004) first documented that W isotope compositions for *s*- and r-processes nuclides were homogeneous among bulk chondrites and differentiated meteorites. On the other hand, Qin et al. (2008) and subsequent studies (Holst et al., 2015; Kruijer et al., 2017) reported that iron meteorites possessed isotopically anomalous W compositions for *s*- and *r*-processes.

The evaluation of *p*-process heterogeneity is more difficult compared to the *s*- and *r*-processes in W isotopes, due to the minor abundance of ^{180}W (0.12 %). Schulz et al. (2013) documented that iron meteorites possess W isotopic anomalies on *p*-process nuclides. However, Cook et al. (2014) and Holst et al. (2015) argued that *p*-process nuclides were homogeneously distributed among the different classes of iron meteorites. This inconsistency may be due to the insufficient analytical precisions and the effect of the cosmic-ray exposures to W isotopes.

(ix) Osmium and platinum

Osmium and Pt are highly siderophile elements. Os has seven stable isotopes (^{184}Os, ^{186}Os, ^{187}Os, ^{188}Os, ^{189}Os, ^{190}Os, and ^{192}Os) and Pt has five stable isotopes (^{192}Pt, ^{194}Pt, ^{195}Pt, ^{196}Pt, and ^{198}Pt). These isotopes are synthesized via stellar nucleosynthesis of the *p*-process (^{184}Os and ^{186}Os), *s*-process (^{185}Os, ^{187}Os, ^{188}Os, ^{189}Os, ^{190}Os, ^{192}Os, ^{192}Pt, ^{194}Pt, ^{195}Pt, and ^{196}Pt), and *r*-process (^{188}Os, ^{189}Os, ^{190}Os, ^{192}Os, ^{194}Pt, ^{195}Pt, ^{196}Pt, and ^{198}Pt). Brandon et al. (2005) first performed high-precision Os isotope analysis for bulk chondrites. Several carbonaceous, an unequibillated enstatite, and ordinary chondrites showed the anomalous Os isotopic compositions. However, the authors

noticed that these results could be induced by incomplete acid digestion of presolar grains contained in primitive meteorites. Alternatively, Yokoyama et al. (2007, 2010) conducted alkali-fusion method for dissolving bulk chondrite samples, showing the measured samples have homogeneous Os isotopic compositions. In contrast to Os, there is still limited number of high-precision Pt isotopic data of bulk meteorites due to the difficulty in the correction for the cosmic-ray exposure. Hunt et al. (2017) reported the *p*-nuclide (^{190}Pt) was homogeneously distributed among different classes of iron meteorites.

1.3.4 Application of nucleosynthetic isotope anomalies

The nucleosynthetic isotope anomalies obtained from cosmochemical samples are powerful tracers for various kinds of researches in the field of planetary sciences. Here we introduce here three applications of nucleosynthetic isotope anomalies observed in meteorite samples: (i) taxonomy of meteorites, (ii) tracking nebular processes, and (iii) decoding accretional history and building blocks of planets.

1.3.4.1 Taxonomy of meteorites

The nucleosynthetic isotope anomalies of bulk meteorites can be used for the taxonomy of meteorite collection. Conventionally, O three-isotope plot is one of the powerful tools for the classification of meteorites. Warren (2011) updated the taxonomy of meteorites by applying the nucleosynthetic isotopic anomalies of O, Ti, Cr, and Ni. In Warren (2011), all the meteorites including chondrites and differentiated meteorites are classified into two groups: non-carbonaceous meteorites (NCs) group and carbonaceous chondrites (CCs) group. Kruijer et al. (2017) followed this approach in Mo isotope analysis and extended to the classification of iron meteorites.

1.3.4.2 Tracking nebular processes

The nucleosynthetic isotope anomalies of bulk meteorites provide the information of the physicochemical processes that occurred in the protoplanetary disk (solar nebula). The isotope heterogeneities among variety of meteorites possibly represent the evidence of nebular thermal processes, resulting the selective destruction of presolar grains (e.g.,

Trinquier et al., 2009). Alternatively, the input of materials from nearby core-collapse supernovae would cause the isotopic heterogeneity in the protoplanetary disk (e.g., Dauphas et al., 2010). The comprehensive solution to explain the isotope heterogeneities observed in a variety of elements has not been established yet.

1.3.4.3 Decoding accretional history and building block of the planets

The nucleosynthetic isotope anomalies of bulk meteorites are useful for the determination of building block materials for the rocky planets in the Solar System (Mercury, Venus, Earth, and Mars). One of the main research topics in the community of cosmochemistry is to decoding the building block of the proto-Earth. Conventionally, it has been considered that the Earth is chemically and isotopically identical to the average of the Solar System. In fact, CI chondrite, chemically unfractionated carbonaceous chondrite, shows nearly identical O isotopic composition to the terrestrial component (e.g., Clayton and Mayeda, 1999). However, in terms of nucleosynthetic isotope anomalies for heavy elements (e.g., Ti, Cr), the most plausible building block of the Earth is enstatite chondrite like material. Nucleosynthetic isotope anomalies of siderophile elements in meteorites (e.g., Mo, Ru) suggest that the only meteorite that shows isotopic compositions unresolvable from terrestrial rocks is IAB iron meteorite (e.g., Bermingham and Walker, 2017). A similar discussion can be made regarding the building blocks of Moon (e.g., Dauphas et al., 2014), Mars (e.g., Borg et al., 2016), and possibly Mercury and Venus (e.g., Fischer-Gödde and Kleine, 2017).

1.4 Objective of this thesis

Construction of an evolutionary model that explains the history of the Solar System is one of the biggest goals in the field of planetary sciences. Chemical and isotopic records from planetary materials (e.g., planets, satellites, asteroids, comets) provide direct evidences that can track the physicochemical processes that occurred in the early Solar System. Among extraterrestrial materials, chondritic meteorites, which derived from parent bodies that have not experienced melting, are the remnants of rocky planetesimals that accreted before the formation of planets. Therefore, chemical and isotopic compositions of chondrites provide vital information to constrain the original building blocks of planets and the nebular processes including evaporation, condensation, and transportation.

The objective of this thesis is to construct an evolutionary model of the early Solar System by means of nucleosynthetic isotopic anomalies recorded in bulk chondrites. In particular, we focus on isotopic anomalies of heavy lithophile elements (Sr and Nd) to track the physicochemical process of silicate dusts that are main components for circumstellar disk of young stars (e.g., van Boekel et al., 2005). To assess the physicochemical environment in the early Solar System, we first developed a procedure for high-precision Nd isotope measurements with TIMS (Chapters 2 and 3). Next, we applied the developed method for high-precision Nd isotope analyses on various types of bulk ordinary and carbonaceous chondrites, coupled with an aggressive sample digestion technique (Chapter 4). Subsequently, we performed high-precision Sr isotope analyses on the same sample aliquots of chondrite of which the Nd isotope anomalies

were obtained in Chapter 4 (Chapter 5). Finally, we introduce the future perspective on the issues that have been discussed in the previous chapters of this thesis (Chapter 6).

References

Akram, W., Schoenbaechler, M., Sprung, P., Vogel, N., 2013. Zirconium-Hafnium isotope evidence from meteorites for the decoupled synthesis of light and heavy neutron-rich nuclei. Astrophysical Journal 777.

Akram, W., Schonbachler, M., Bisterzo, S., Gallino, R., 2015. Zirconium isotope evidence for the heterogeneous distribution of s-process materials in the solar system. Geochimica et Cosmochimica Acta 165, 484-500.

Amari, S., Lewis, R.S., Anders, E., 1994. Interstellar grains in meteorites. 1. Isolation of SiC, graphite, and diamond - size distributions of SiC and graphite. Geochimica et Cosmochimica Acta 58, 459-470.

Anders, E., Grevesse, N., 1989. Abundances of the elements - Meteoritic and Solar. Geochimica et Cosmochimica Acta 53, 197-214.

Andreasen, R., Sharma, M., 2006. Solar nebula heterogeneity in p-process samarium and neodymium isotopes. Science 314, 806-809.

Andreasen, R., Sharma, M., 2007. Mixing and homogenization in the early solar system: Clues from Sr, Ba, Nd, and Sm isotopes in meteorites. Astrophysical Journal 665, 874-883.

Argast, D., Samland, M., Thielemann, F.K., Qian, Y.Z., 2004. Neutron star mergers versus core-collapse supernovae as dominant r-process sites in the early Galaxy. Astronomy & Astrophysics 416, 997-1011.

Arlandini, C., Kappeler, F., Wisshak, K., Gallino, R., Lugaro, M., Busso, M., Straniero, O., 1999. Neutron capture in low-mass asymptotic giant branch stars: Cross sections and abundance signatures. Astrophysical Journal 525, 886-900.

Bermingham, K.R., Mezger, K., Scherer, E.E., Horan, M.F., Carlson, R.W., Upadhyay, D., Magna, T., Pack, A., 2016. Barium isotope abundances in meteorites and their implications for early Solar System evolution. Geochimica et Cosmochimica Acta 175, 282-298.

Bermingham, K.R., Walker, R.J., 2017. The ruthenium isotopic composition of the oceanic mantle. Earth and Planetary Science Letters 474, 466-473.

Bermingham, K.R., Worsham, E.A., Walker, R.J., 2018. New insights into Mo and Ru isotope variation in the nebula and terrestrial planet accretionary genetics. Earth and Planetary Science Letters 487, 221-229.

Bisterzo, S., Gallino, R., Kappeler, F., Wiescher, M., Imbriani, G., Straniero, O., Cristallo, S., Gorres, J., deBoer, R.J., 2015. The branchings of the main s-process: their sensitivity to alpha-induced reactions on ^{13}C and ^{22}Ne and to the uncertainties of the nuclear network. Monthly Notices of the Royal Astronomical Society 449, 506-527.

Bisterzo, S., Gallino, R., Straniero, O., Cristallo, S., Kappeler, F., 2011. The s-process in low-metallicity stars - II. Interpretation of high-resolution spectroscopic observations with asymptotic giant branch models. Monthly Notices of the Royal Astronomical Society 418, 284-319.

Bisterzo, S., Travaglio, C., Gallino, R., Wiescher, M., Kappeler, F., 2014. Galactic chemical evolution and solar s-process abundances: Dependence of the ^{13}C-pocket structure. Astrophysical Journal 787.

Borg, L.E., Brennecka, G.A., Symes, S.J.K., 2016. Accretion timescale and impact history of Mars deduced from the isotopic systematics of martian meteorites. Geochimica et Cosmochimica Acta 175, 150-167.

Boyet, M., Carlson, R.W., 2005. ^{142}Nd evidence for early (> 4.53 Ga) global differentiation of the silicate Earth. Science 309, 576-581.

Brandon, A.D., Humayun, M., Puchtel, I.S., Leya, I., Zolensky, M., 2005. Osmium isotope evidence for an s-process carrier in primitive chondrites. Science 309, 1233-1236.

Budde, G., Burkhardt, C., Brennecka, G.A., Fischer-Gödde, M., Kruijer, T.S., Kleine, T., 2016. Molybdenum isotopic evidence for the origin of chondrules and a distinct genetic heritage of carbonaceous and non-carbonaceous meteorites. Earth and Planetary Science Letters 454, 293-303.

Burbidge, E.M., Burbidge, G.R., Fowler, W.A., Hoyle, F., 1957. Synthesis of the elements in stars. Reviews of Modern Physics 29, 547-650.

Burkhardt, C., Kleine, T., Oberli, F., Pack, A., Bourdon, B., Wieler, R., 2011. Molybdenum isotope anomalies in meteorites: Constraints on solar nebula evolution and origin of the Earth. Earth and Planetary Science Letters 312, 390-400.

Carlson, R.W., Boyet, M., Horan, M., 2007. Chondrite barium, neodymium, and samarium isotopic heterogeneity and early earth differentiation. Science 316, 1175-1178.

Chen, J.H., Papanastassiou, D.A., Wasserburg, G.J., 2010. Ruthenium endemic isotope effects in chondrites and differentiated meteorites. Geochimica et Cosmochimica Acta 74, 3851-3862.

Clayton, R.N., 1993. Oxygen isotopes in meteorites. Annual Review of Earth and Planetary Sciences 21, 115-149.

Clayton, R.N., Hinton, R.W., Davis, A.M., 1988. Isotopic variations in the rock-forming elements in meteorites. Philosophical Transactions of the Royal Society a-Mathematical Physical and Engineering Sciences 325, 483-501.

Clayton, R.N., Mayeda, T.K., 1996. Oxygen isotope studies of achondrites. Geochimica et Cosmochimica Acta 60, 1999-2017.

Clayton, R.N., Mayeda, T.K., 1999. Oxygen isotope studies of carbonaceous chondrites. Geochimica et Cosmochimica Acta 63, 2089-2104.

Cook, D.L., Kruijer, T.S., Leya, I., Kleine, T., 2014. Cosmogenic ^{180}W variations in meteorites and re-assessment of a possible ^{184}Os–^{180}W decay system. Geochimica et Cosmochimica Acta 140, 160-176.

Dauphas, N., Chen, J.H., Zhang, J.J., Papanastassiou, D.A., Davis, A.M., Travaglio, C., 2014. ^{48}Ca isotopic anomalies in bulk chondrites and achondrites: Evidence for a uniform isotopic reservoir in the inner protoplanetary disk. Earth and Planetary Science Letters 407, 96-108.

Dauphas, N., Davis, A.M., Marty, B., Reisberg, L., 2004. The cosmic molybdenum-ruthenium isotope correlation. Earth and Planetary Science Letters 226, 465-475.

Dauphas, N., Remusat, L., Chen, J.H., Roskosz, M., Papanastassiou, D.A., Stodolna, J., Guan, Y., Ma, C., Eiler, J.M., 2010. Neutron-rich chromium isotope anomalies in nanoparticles. Astrophysical Journal 720, 1577-1591.

Ek, M., Hunt, A.C., Schonbachler, M., 2017. A new method for high-precision palladium isotope analyses of iron meteorites and other metal samples. Journal of Analytical Atomic Spectrometry 32, 647-656.

Fehr, M.A., Rehkaemper, M., Halliday, A.N., Schoenbaechler, M., Hattendorf, B., Guenther, D., 2006. Search for nucleosynthetic and radiogenic tellurium isotope anomalies in carbonaceous chondrites. Geochimica et Cosmochimica Acta 70, 3436-3448.

Fehr, M.A., Rehkamper, M., Halliday, A.N., 2004. Application of MC-ICPMS to the precise determination of tellurium isotope compositions in chondrites, iron meteorites and sulfides. International Journal of Mass Spectrometry 232, 83-94.

Fischer-Gödde, M., Burkhardt, C., Kruijer, T.S., Kleine, T., 2015. Ru isotope heterogeneity in the solar protoplanetary disk. Geochimica et Cosmochimica Acta 168, 151-171.

Fischer-Gödde, M., Kleine, T., 2017. Ruthenium isotopic evidence for an inner Solar System origin of the late veneer. Nature 541, 525-527.

Fukami, Y., Yokoyama, T., 2014. Precise tellurium isotope analysis by negative thermal ionization mass spectrometry (N-TIMS). Journal of Analytical Atomic Spectrometry 29, 520-528.

Gallino, R., Arlandini, C., Busso, M., Lugaro, M., Travaglio, C., Straniero, O., Chieffi, A., Limongi, M., 1998. Evolution and nucleosynthesis in low-mass asymptotic giant branch stars. II. Neutron capture and the s-process. Astrophysical Journal 497, 388-403.

Hans, U., Kleine, T., Bourdon, B., 2013. Rb-Sr chronology of volatile depletion in differentiated protoplanets: BABI, ADOR and ALL revisited. Earth and Planetary Science Letters 374, 204-214.

Holst, J.C., Paton, C., Wielandt, D., Bizzarro, M., 2015. Tungsten isotopes in bulk meteorites and their inclusions-Implications for processing of presolar components in the solar protoplanetary disk. Meteoritics & Planetary Science 50, 1643-1660.

Hoppe, P., Kocher, T., Eberhardt, P., Amari, S., Lewis, R.S., 1998. Carbon- and nitrogen-isotopic compositions of individual, submicrometer-sized presolar silicon carbide grains. Meteoritics & Planetary Science 33, A71-A71.

Hunt, A.C., Ek, M., Schonbachler, M., 2017. Platinum isotopes in iron meteorites: Galactic cosmic ray effects and nucleosynthetic homogeneity in the p-process isotope ^{190}Pt and the other platinum isotopes. Geochimica et Cosmochimica Acta 216, 82-95.

Hynes, K. M., and F. Gyngard., 2009. The Presolar Grain Database. Lunar and Planetary Science Conference, 40.

Käppeler, F., Beer, H., Wisshak, K., 1989. s-process nucleosynthesis - nuclear physics and the classical model. Reports on Progress in Physics 52, 945-1013.

Kasen, D., Metzger, B., Barnes, J., Quataert, E., Ramirez-Ruiz, E., 2017. Origin of the heavy elements in binary neutron-star mergers from a gravitational-wave event. Nature 551, 80-84.

Kleine, T., Mezger, K., Palme, H., Munker, C., 2004. The W isotope evolution of the bulk silicate Earth: constraints on the timing and mechanisms of core formation and accretion. Earth and Planetary Science Letters 228, 109-123.

Kruijer, T.S., Burkhardt, C., Budde, G., Kleine, T., 2017. Age of Jupiter inferred from the distinct genetics and formation times of meteorites. Proceedings of the National Academy of Sciences of the United States of America 114, 6712-6716.

Lambert, D.L., Gustafsson, B., Eriksson, K., Hinkle, K.H., 1986. The chemical composition of carbon stars. 1. Carbon, Nitrogen, and Oxygen in 30 cool carbon stars in the galactic disk. Astrophysical Journal Supplement Series 62, 373-425.

Lewis, R.S., Amari, S., Anders, E., 1994. Interstellar grains in meteorites. 2. SiC and its noble gases. Geochimica Et Cosmochimica Acta 58, 471-494.

Lodders, K., H. Palme, H-P. Gail., 2009. 4.4 Abundances of the elements in the Solar System. Solar system. Springer, 712-770.

Maas, R., Loss, R.D., Rosman, K.J.R., Lewis, R.S., Huss, G.R., Lugmair, G.W., 2001. Isotope anomalies in tellurium and palladium from Allende nanodiamonds. Meteoritics & Planetary Science 36, 849-858.

Mayer, B., Wittig, N., Humayun, M., Leya, I., 2015. Palladium isotopic evidence for nucleosynthetic and cosmogenic isotope anomalies in IVB iron meteorites. Astrophysical Journal 809.

Merrill, P.W., 1952. Spectroscopic observations of stars of class-S. Astrophysical Journal 116, 21-26.

Moynier, F., Day, J.M.D., Okui, W., Yokoyama, T., Bouvier, A., Walker, R.J., Podosek, F.A., 2012. Planetary-scale strontium isotopic heterogeneity and the age of volatile depletion of early solar system materials. Astrophysical Journal 758.

Nicolussi, G.K., Pellin, M.J., Lewis, R.S., Davis, A.M., Amari, S., Clayton, R.N., 1998. Molybdenum isotopic composition of individual presolar silicon carbide grains from the Murchison meteorite. Geochimica et Cosmochimica Acta 62, 1093-1104.

Nishimura, N., Takiwaki, T., Thielemann, F.K., 2015. The r-process nucleosynthesis in the various jet-like explosions of magnetorotational core-collapse supernovae. Astrophysical Journal 810.

Paton, C., Schiller, M., Bizzarro, M., 2013. Identification of an ^{84}Sr-depleted carrier in primitive meteorites and implications for thermal processing in the solar protoplanetary disk. Astrophysical Journal Letters 763.

Peters, S.T.M., Munker, C., Pfeifer, M., Elfers, B.M., Sprung, P., 2017. Distribution of p-process ^{174}Hf in early solar system materials and the origin of nucleosynthetic

Hf and W isotope anomalies in Ca-Al rich inclusions. Earth and Planetary Science Letters 459, 70-79.

Poole, G.M., Rehkamper, M., Coles, B.J., Goldberg, T., Smith, C.L., 2017. Nucleosynthetic molybdenum isotope anomalies in iron meteorites - new evidence for thermal processing of solar nebula material. Earth and Planetary Science Letters 473, 215-226.

Qin, L.P., Dauphas, N., Wadhwa, M., Markowski, A., Gallino, R., Janney, P.E., Bouman, C., 2008. Tungsten nuclear anomalies in planetesimal cores. Astrophysical Journal 674, 1234-1241.

Qin, L., Carlson, R.W., Alexander, C.M.O.D., 2011. Correlated nucleosynthetic isotopic variability in Cr, Sr, Ba, Sm, Nd and Hf in Murchison and QUE 97008. Geochimica et Cosmochimica Acta 75, 7806-7828.

Qin, L., Nittler, L.R., Alexander, C.M.O., Wang, J., Stadermann, F.J., Carlson, R.W., 2011. Extreme ^{54}Cr-rich nano-oxides in the CI chondrite Orgueil - Implication for a late supernova injection into the solar system. Geochimica et Cosmochimica Acta 75, 629-644.

Ranen, M.C., Jacobsen, S.B., 2006. Barium isotopes in chondritic meteorites: Implications for planetary reservoir models. Science 314, 809-812.

Rauscher, T., Dauphas, N., Dillmann, I., Froehlich, C., Fueloep, Z., Gyuerky, G., 2013. Constraining the astrophysical origin of the p-nuclei through nuclear physics and meteoritic data. Reports on Progress in Physics 76.

Regelous, M., Elliott, T., Coath, C.D., 2008. Nickel isotope heterogeneity in the early Solar System. Earth and Planetary Science Letters 272, 330-338.

Richter, S., Ott, U., Begemann, F., 1998. Tellurium in presolar diamonds as an indicator for rapid separation of supernova ejecta. Nature 391, 261-263.

Schulz, T., Munker, C., Peters, S.T.M., 2013. p-process ^{180}W anomalies in iron meteorites: Nucleosynthetic versus non-nucleosynthetic origins. Earth and Planetary Science Letters 362, 246-257.

Smith, V.V., Lambert, D.L., 1990. The chemical composition of red giants. 3. Further CNO isotopic and s-process abundances in thermally pulsing asymptotic giant branch stars. Astrophysical Journal Supplement Series 72, 387-416.

Sneden, C., McWilliam, A., Preston, G.W., Cowan, J.J., Burris, D.L., Armosky, B.J., 1996. The ultra metal poor, neutron capture rich giant star CS 22892-052. Astrophysical Journal 467, 819-840.

Schönbächler, M., Rehkämper, M., Lee, D. C., & Halliday, A. N., 2004. Ion exchange chromatography and high precision isotopic measurements of zirconium by MC-ICP-MS. Analyst, 129 (1), 32-37.

Sprung, P., Scherer, E.E., Upadhyay, D., Leya, I., Mezger, K., 2010. Non-nucleosynthetic heterogeneity in non-radiogenic stable Hf isotopes: Implications for early solar system chronology. Earth and Planetary Science Letters 295, 1-11.

Travaglio, C., Gallino, R., Arnone, E., Cowan, J., Jordan, F., Sneden, C., 2004. Galactic evolution of Sr, Y, and Zr: A multiplicity of nucleosynthetic processes. Astrophysical Journal 601, 864-884.

Trinquier, A., Birck, J.L., Allegre, C.J., 2007. Widespread ^{54}Cr heterogeneity in the inner solar system. Astrophysical Journal 655, 1179-1185.

Trinquier, A., Elliott, T., Ulfbeck, D., Coath, C., Krot, A.N., Bizzarro, M., 2009. Origin of nucleosynthetic isotope heterogeneity in the solar protoplanetary disk. Science 324, 374-376.

Tsujimoto, T., Shigeyama, T., 2014. enrichment history of r-process elements shaped by a merger of neutron star pairs. Astronomy & Astrophysics 565.

van Boekel, R., Min, M., Waters, L., de Koter, A., Dominik, C., van den Ancker, M.E., Bouwman, J., 2005. A 10 μm spectroscopic survey of Herbig Ae star disks: Grain growth and crystallization. Astronomy & Astrophysics 437, 189-208.

Wanajo, S., 2013. The r-process in proto-neutron-star wind revisited. Astrophysical Journal Letters 770.

Warren, P.H., 2011. Stable-isotopic anomalies and the accretionary assemblage of the Earth and Mars: A subordinate role for carbonaceous chondrites. Earth and Planetary Science Letters 311, 93-100.

Worsham, E.A., Bermingham, K.R., Walker, R.J., 2017. Characterizing cosmochemical materials with genetic affinities to the Earth: Genetic and chronological diversity within the IAB iron meteorite complex. Earth and Planetary Science Letters 467, 157-166.

Yin, Q.-Z., Lee, C.-T.A., Ott, U., 2006. Signatures of the s-process in presolar silicon carbide grains: Barium through hafnium. Astrophysical Journal 647, 676-684.

Yokoyama, T., Alexander, C.M.O.D., Walker, R.J., 2010. Osmium isotope anomalies in chondrites: Results for acid residues and related leachates. Earth and Planetary Science Letters 291, 48-59.

Yokoyama, T., Fukami, Y., Okui, W., Ito, N., Yamazaki, H., 2015. Nucleosynthetic strontium isotope anomalies in carbonaceous chondrites. Earth and Planetary Science Letters 416, 46-55.

Yokoyama, T., Rai, V.K., Alexander, M.O.D., Lewis, R.S., Carlson, R.W., Shirey, S.B., Thiemens, M.H., Walker, R.J., 2007. Osmium isotope evidence for uniform distribution of s- and r-process components in the early solar system. Earth and Planetary Science Letters 259, 567-580.

Yurimoto, H., Kuramoto, K., 2004. Molecular cloud origin for the oxygen isotope heterogeneity in the solar system. Science 305, 1763-1766.

Zinner, E., Amari, S., Lewis, R.S., 1991. s-process Ba, Nd, and Sm in presolar SiC from the Murchison meteorite. Astrophysical Journal 382, L47-L50.

Chapter 2:
Evaluation of the long-term fluctuation in isotope ratios measured by TIMS with the static, dynamic, and multistatic methods:
A case study for Nd isotope measurements

based on Fukai, R., Yokoyama, T., and Kagami, S. (2017) IJMS, 414, 1.

Abstract

High-precision Nd isotope measurements is widely applied to geochemical and cosmochemical samples. To achieve isotope ratio measurements at a level of sub-5 ppm analytical precision, we investigated the long-term fluctuation in high-precision Nd isotope measurements by using a modern thermal ionization mass spectrometer (Triton *Plus*). Comprehensive measurements of a standard material JNdi-1 (n = 76) were conducted by applying three distinct (static, dynamic, and multistatic) methods during an eight-month analytical period, which was further divided into seven short analytical campaigns. The reproducibilities of $^{142}Nd/^{144}Nd$ ratios for campaigns 1–4 were ±23, ±6.4, and ±17 ppm (2 SDs) for the static (Jump 1), dynamic, and multistatic methods, respectively. After the replacement of six out of nine Faraday cups (campaigns 5–7), the reproducibilities of $^{142}Nd/^{144}Nd$ ratios were improved to ±18, ±4.1, and ±5.4 ppm (2 SDs) for the static, dynamic, and multistatic methods, respectively. This implies that high-precision Nd isotope analysis with not only the static but also the multistatic method is susceptible to the deterioration of Faraday cups. We found the dynamic method the most effective to minimize the influence of Faraday cup degradation, although a marginal isotopic shift was observed even for data obtained by the dynamic method throughout the entire analytical period. In addition to $^{142}Nd/^{144}Nd$, our dynamic method allows to determine $^{148}Nd/^{144}Nd$ and $^{150}Nd/^{144}Nd$ ratios precisely. The reproducibilities of $^{148}Nd/^{144}Nd$ and $^{150}Nd/^{144}Nd$ ratios for campaigns 5–7 were ±6.3 and ±8.8 ppm, respectively, which are 1.5–4.1 times better than those obtained in previous studies. Our new dynamic method is suited for the detection of nucleosynthetic Nd

isotope anomalies in meteorite samples.

2.1 Introduction

The advent of new-generation mass spectrometers in the last decade has greatly accelerated research in geosciences and analytical chemistry. Isotope ratio measurements at a level of sub-5 ppm analytical precision (2 SD) are now possible with modern instruments of thermal ionization mass spectrometry (TIMS) and inductively coupled plasma-mass spectrometry (ICP-MS) (e.g., for Nd, W: Caro et al., 2006; Touboul and Walker, 2012). In isotope analysis with TIMS and ICP-MS, the stability of physical devices forming part of the instrument is crucial for obtaining highly precise and accurate isotope ratios. Technological innovations in mass spectrometers involve further advancements in the performance of physical devices including the ion source, mass analyzer, and ion detectors, leading to dramatic improvements in the precision of isotope ratios. Out of all such physical devices, the stability of the Faraday cup detector is one of the most important factors that directly controls the precision of the measured isotope ratios. A well-known problem with Faraday cup detectors, which compromises precise and accurate isotope ratio measurements, is the systematic change in Faraday cup efficiencies accompanying their heavy use (Makishima and Nakamura, 1991; Thirlwall, 1991; Carlson, 2014; Yokoyama et al., 2015). This is caused by the long-term accumulation of strong ion beams in the Faraday cup interior, which is made of graphite, generating a coating on the surface of the graphite interior where emissions of secondary charged particles are no longer suppressed (Carlson, 2014). As a few secondary charged particles can escape from the Faraday cup interior, the number of electrons passing through the amplifier from the ground is reduced from those

corresponding to neutralizing the total number of incoming ions, which results in the deterioration of the Faraday cup efficiency.

The problem of Faraday cup deterioration was much greater in 1990s when the performance of Faraday cups was inferior to that of more recently-designed ones. Even with the improved Faraday cups, however, cup aging is problematic for current geochemical applications with ultra-high-precision isotope ratio measurements (Carlson, 2014; Yokoyama et al., 2015). This problem is especially prominent in the most frequently used isotope measurement technique, called the "static method," in which ion beams with different masses are simultaneously acquired using multiple Faraday cups fixed to certain positions, because the extent of Faraday cup deterioration in individual cups is independent and different in each case. By contrast, the "dynamic multicollection" method was developed to minimize the effect of cup deterioration. This method was first introduced by Lenz and Wendt (1976), followed by the studies of radiogenic isotopes (e.g., $^{87}Sr/^{86}Sr$, $^{143}Nd/^{144}Nd$: Thirlwall, 1991; Wendt and Hasse, 1998). In addition, the "multistatic" method is becoming more common in recent mass spectrometric measurements, where multiple isotopic ratios measured by the static multicollection are averaged (e.g., Caro et al, 2006; Brandon et al., 2009).

Ultra-high-precision Nd isotope analysis is becoming increasingly important in geochemistry and cosmochemistry (e.g., Roth et al., 2014; Boyet et al., 2015). Neodymium is an ideal element for evaluating the long-term fluctuation in isotope ratios caused by Faraday cup deterioration, because it has seven isotopes that can be monitored by multiple Faraday cups, and several studies have reported long-term

instrumental fluctuation in standard Nd isotope ratios. In an early Nd isotope study using an older-generation TIMS instrument (VG-354; Thermo Fischer Scientific, USA), the reproducibility of the standard $^{143}Nd/^{144}Nd$ ratio obtained in the four-year consecutive measurements with the dynamic method was approximately six times better than that obtained with the static method (Thirlwall, 1991). In the case of modern TIMS instruments (e.g., Triton; Thermo Fischer Scientific), a systematic increase in the standard $^{142}Nd/^{144}Nd$ ratio determined by the static method has been observed (Boyet and Carlson, 2007; Carlson, 2014). By contrast, Nd isotope ratios obtained with the dynamic method have usually been shown no drift during the entire analytical periods (O'Neil et al., 2008; Roth et al., 2014).

In this study, we performed Nd isotope measurements with the static, dynamic, and multistatic methods using a modern TIMS instrument (Triton *Plus*, Thermo Fischer Scientific) over an eight-month period, during which a number of measurements (n = 76) were conducted to directly compare the three analytical protocols in detail for the first time. In addition, the distinct characteristics of mass-dependent isotopic fractionation correction (exponential or power law) with the dynamic method were examined. Furthermore, we propose a new two-jump dynamic method that can obtain $^{142}Nd/^{144}Nd$, $^{148}Nd/^{144}Nd$, and $^{150}Nd/^{144}Nd$ ratios simultaneously.

2.2 Experimental

2.2.1 Sample

To evaluate the performance of Nd isotope analysis with TIMS instrument, we repeatedly analyzed a Nd isotope standard JNdi-1 that was dissolved in 6.4 M HCl (EL grade; Mitsubishi Chemical, Japan).

2.2.2 Mass spectrometry

All isotope measurements were performed by TIMS instrument (Triton *Plus*) at the Tokyo Institute of Technology. The instrument was equipped with nine Faraday cups linked to 10^{11} Ω resistors, three electron multipliers, and two compact discrete dynodes.

Neodymium isotopes were collected with two different axial fields, Jumps 1 and 2 (Table 2.1), within a single measurement run. To achieve precise peak overlap of individual Nd isotopes in the dynamic method, we applied the "zoom optics" system provided with Triton *Plus*—which is controlled by two electrodes (focus and dispersion quads).

Table 2.1 *Cup configuration of Nd isotope measurement with TIMS.*

	L4	L3	L2	L1	C	H1	H2	H3	H4
Jump 1	^{140}Ce	^{142}Nd	^{143}Nd	^{144}Nd	^{145}Nd	^{146}Nd	^{147}Sm	^{148}Nd	^{150}Nd
Jump 2		^{140}Ce		^{142}Nd	^{143}Nd	^{144}Nd	^{145}Nd	^{146}Nd	^{148}Nd

2.2.3 Data reduction

Here we introduce the equations that were used for data reduction in the static, dynamic, and multistatic methods. The protocol described here can be applied not only to high-precision analysis with TIMS but also to multicollector (MC) -ICP-MS analysis and the analysis using few amounts of samples (< 10 ng: e.g., Harvey and Baxter, 2009). First, we evaluate the extent of Faraday cup degradation by the following equation:

$$V = \alpha IR \quad (2.1)$$

where V is the beam intensity (volts) monitored by a voltmeter equipped with an amplifier, α is the Faraday cup efficiency, I is the ion current entering the cup, and R is the gain factor for the amplifier. The α value is regarded as unity when the cup is fresh. Importantly, the α values cannot be determined by the gain calibration of amplifiers, implying that the variability of α values among different cups causes the shift in isotope ratios determined by multiple Faraday cups.

2.2.3.1 Static method

The exponential law is a common approach to correcting for the mass-dependent isotopic fractionation, which occurs during TIMS analysis. With the exponential law, the corrected $^{142}Nd/^{144}Nd$ ratio, $(^{142}Nd/^{144}Nd)_{corr.}$, is obtained by the following equation assuming a reference isotope ratio of $(^{146}Nd/^{144}Nd)_{ref.} = 0.7219$:

$$\left(\frac{^{142}\mathrm{Nd}}{^{144}\mathrm{Nd}}\right)_{corr.} = \left(\frac{^{142}\mathrm{Nd}}{^{144}\mathrm{Nd}}\right)_{obs.} \left\{\frac{\left(\frac{^{146}\mathrm{Nd}}{^{144}\mathrm{Nd}}\right)_{ref.}}{\left(\frac{^{146}\mathrm{Nd}}{^{144}\mathrm{Nd}}\right)_{obs.}}\right\}^{f_1} \qquad (2.2)$$

$$f_1 = \frac{\ln\left(\frac{m_{142}}{m_{144}}\right)}{\ln\left(\frac{m_{146}}{m_{144}}\right)} \cong -1.014 \qquad (2.3)$$

where m_{142}, m_{144}, and m_{146} are the isotope masses for ^{142}Nd, ^{144}Nd, and ^{146}Nd, respectively. Note that Eq. 2.2 ignores the effect of Faraday cup aging. Previous studies using the static method tried to avoid the problem of cup aging by analyzing a Nd standard, with a known isotopic composition, together with the sample of interest for normalizing the obtained results.

2.2.3.2 Dynamic method

In the dynamic method, equations for corrections of mass-dependent isotopic fractionation can be simply represented by the power law. Following the description in Carlson (2014), (^{142}Nd/^{144}Nd)$_{corr.}$ ratios can be noted as below with the two-jump configuration (Table 2.1), where the observed ^{142}Nd/^{144}Nd and ^{146}Nd/^{144}Nd ratios are determined by Jump 2 and Jump 1 measurements, respectively, using only two Faraday cups (L1 and H1):

$$\left(\frac{^{142}\mathrm{Nd}}{^{144}\mathrm{Nd}}\right)_{corr.} = \frac{\left(\frac{V_{142}}{V_{144}}\right)_{Jump\,2} \times \left(\frac{V_{146}}{V_{144}}\right)_{Jump\,1}}{\left(\frac{^{146}\mathrm{Nd}}{^{144}\mathrm{Nd}}\right)_{ref.}} \qquad (2.4).$$

In contrast to the static method, the Faraday cup efficiencies are completely canceled out. Coupling this equation with Eq. 2.2 gives the equation for the exponential law correction, as described by Carlson (2014):

$$\left(\frac{^{142}\mathrm{Nd}}{^{144}\mathrm{Nd}}\right)_{corr.} = \left(\frac{V_{142}}{V_{144}}\right)_{Jump\ 2} \left\{\frac{\left(\frac{^{146}\mathrm{Nd}}{^{144}\mathrm{Nd}}\right)_{ref.}}{\left(\frac{V_{146}}{V_{144}}\right)_{Jump\ 1}}\right\}^{f_1} \left(\frac{\alpha_{H1}}{\alpha_{L1}}\right)^{1+f_1} \qquad (2.5)$$

$$\left(\frac{\alpha_{H1}}{\alpha_{L1}}\right)^{1+f_1} = \left(\frac{\alpha_{H1}}{\alpha_{L1}}\right)^{-0.014} \qquad (2.6).$$

Unlike the equation with the power law correction, Faraday cup efficiencies are not completely canceled out in this equation, although the last term would not significantly affect the precision of measurement within a realistic range of cup degradation (Thirlwall and Anczkiewicz, 2004).

In this study, we applied the concept of the dynamic method for the determination of $^{148}Nd/^{144}Nd$ and $^{150}Nd/^{144}Nd$ ratios (Wendt and Hasse, 1998; Thirlwall and Anczkiewicz, 2004). In the case of $(^{148}Nd/^{144}Nd)_{corr.}$, we followed the method of Thirlwall and Anczkiewicz (2004) in which the observed $^{146}Nd/^{144}Nd$ and $^{148}Nd/^{146}Nd$ ratios obtained in the Jump 2 and Jump 1 measurements (Table 2.1), respectively, were involved in the calculation:

$$\left(\frac{^{148}\mathrm{Nd}}{^{144}\mathrm{Nd}}\right)_{corr.} = \left(\frac{^{146}\mathrm{Nd}}{^{144}\mathrm{Nd}}\right)_{ref.} \left(\frac{^{148}\mathrm{Nd}}{^{146}\mathrm{Nd}}\right)_{obs.} \left\{\frac{\left(\frac{^{144}\mathrm{Nd}}{^{146}\mathrm{Nd}}\right)_{ref.}}{\left(\frac{^{144}\mathrm{Nd}}{^{146}\mathrm{Nd}}\right)_{obs.}}\right\}^{f_2}$$

$$= \left(\frac{^{146}\mathrm{Nd}}{^{144}\mathrm{Nd}}\right)_{ref.} \left(\frac{V_{148}}{V_{146}}\right)_{Jump\ 1} \left\{\frac{\left(\frac{V_{146}}{V_{144}}\right)_{Jump\ 2}}{\left(\frac{^{146}\mathrm{Nd}}{^{144}\mathrm{Nd}}\right)_{ref.}}\right\}^{f_2} \left(\frac{\alpha_{H1}}{\alpha_{H3}}\right)^{1+f_2} \qquad (2.7)$$

$$f_2 = \frac{\ln\left(\frac{m_{148}}{m_{146}}\right)}{\ln\left(\frac{m_{144}}{m_{146}}\right)} \cong -0.987 \qquad (2.8).$$

Likewise, we can derive the equation for the determination of (^{150}Nd/^{144}Nd)$_{corr.}$ as follows:

$$\left(\frac{^{150}\mathrm{Nd}}{^{144}\mathrm{Nd}}\right)_{corr.} = \left(\frac{^{150}\mathrm{Nd}}{^{144}\mathrm{Nd}}\right)_{obs.} \left\{\frac{\left(\frac{^{148}\mathrm{Nd}}{^{142}\mathrm{Nd}}\right)_{corr.}}{\left(\frac{^{148}\mathrm{Nd}}{^{142}\mathrm{Nd}}\right)_{obs.}}\right\}^{f_3}$$

$$= \left(\frac{V_{150}}{V_{144}}\right)_{Jump\ 1} \left\{\frac{\left(\frac{^{148}\mathrm{Nd}}{^{144}\mathrm{Nd}}\right)_{corr.} \Big/ \left(\frac{^{142}\mathrm{Nd}}{^{144}\mathrm{Nd}}\right)_{corr.}}{\left(\frac{V_{148}}{V_{142}}\right)_{Jump\ 2}}\right\}^{f_3} \left(\frac{\alpha_{L1}}{\alpha_{H4}}\right)^{1-f_3} \qquad (2.9)$$

$$f_3 = \frac{\ln\left(\frac{m_{150}}{m_{144}}\right)}{\ln\left(\frac{m_{148}}{m_{142}}\right)} \cong 0.987 \qquad (2.10).$$

Thirlwall and Anczkiewicz (2004) proposed a similar equation for deriving the ^{150}Nd/^{144}Nd ratio with the dynamic method wherein the authors adopted the mean ^{148}Nd/^{144}Nd ratio of a standard material that was separately determined in their long-term measurements. However, their procedure cannot be applied to samples that have ^{148}Nd/^{144}Nd ratios distinct from the standard material (e.g., meteorites, return mission samples). Our approach, however, solves this problem; Eq. 2.9 includes (^{142}Nd/^{144}Nd)$_{corr.}$ and (^{148}Nd/^{144}Nd)$_{corr.}$ values that are given by Eqs. 2.5 and 2.7 derived from an identical measurement, respectively. It should be noted that the analytical error

of ($^{150}Nd/^{144}Nd)_{corr.}$ covaries with those of ($^{142}Nd/^{144}Nd)_{corr.}$ and ($^{148}Nd/^{144}Nd)_{corr.}$ ratios.

2.3 Results and Discussion

The performance of Nd isotope analysis using TIMS instrument was evaluated by repeated measurements of the isotope standard JNdi-1 conducted over eight months (*n* = 76; November 2014–June 2015). The entire analytical period was further divided into seven analytical campaigns, each of which spanned up to two months. The analytical reproducibilities described in this section are two standard deviations (2 SDs) unless noted otherwise.

2.3.1 Effect of Faraday cup deterioration in the static method

First, we compare the results of repeated measurements with the static and dynamic methods. As mentioned earlier, the analytical reproducibilities of isotope measurements with the static method are strongly affected by the deterioration of Faraday cups. Our TIMS instrument has been used continuously since its installation in March 2010, and significant degradation of Faraday cup efficiencies has been observed for some cups (Yokoyama et al., 2015). The aged graphite shells in the nine Faraday cups of our instrument were replaced at different times; three cups before the start of this study (April 2014: C, H1, and H2) and the remaining six cups during the course of this study (April 2015: L4, L3, L2, L1, H3, and H4). Therefore, it was not possible to obtain Nd isotope ratios in the static method using all fresh Faraday cups.

Fig. 2.1 shows the fluctuation in $^{142}Nd/^{144}Nd$ ratio obtained with the static and dynamic methods during the entire analytical period. Prior to the replacement of the six Faraday cups in April 2015, the overall reproducibilities for the static method

throughout campaigns 1–4 were ±23 ppm in Jump 1 measurements and ±21 ppm in Jump 2 measurements. These reproducibilities were inferior to those reported in previous studies obtained by the static method (Boyet and Carlson, 2005; Andreasen and Sharma, 2006; Gannoun et al., 2011), evidently due to the systematic shifts in Nd isotope ratio caused by the deterioration of Faraday cups in our instrument. The overall reproducibilities of static Nd isotope ratios throughout campaigns 5–7 were generally comparable (±18 ppm, Jump 1; ±23 ppm, Jump 2) to those in campaigns 1–4; however, the short-term reproducibilities in campaigns 5–7 were to some extent stabilized after the Faraday cup replacement (Table 2.2). The typical internal precision of the static method (±3–6 ppm) is superior to the reproducibility of the measurements during the entire analytical period.

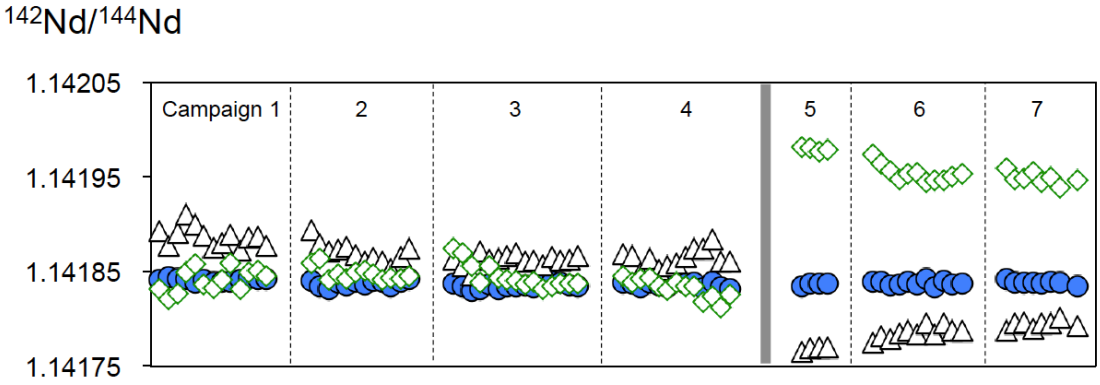

Fig. 2.1 *Fluctuation in Nd isotope ratios obtained by the dynamic method (Jump 1: open triangles; Jump 2: open diamonds) in the repeated analysis for JNdi-1 during analytical campaigns 1–7. Those obtained by the dynamic method (filled circles) are plotted for comparison. Dashed lines divide individual analytical campaigns, and the bold line indicates the timing of the replacement of six Faraday cups in April 2015.*

Table 2.2 *Mean $^{142}Nd/^{144}Nd$ ratios and reproducibilities (2 SDs) of the repeated analysis for JNdi-1 measured by the dynamic (exponential law and power law), multistatic, and static methods. Analytical reproducibilities (2 SDs) are denoted as ppm order.*

Campaign	N	Term	*Dynamic (exponential)*		*Dynamic (power)*		*Multistatic*		*Static Jump 1*		*Static Jump 2*	
			Mean	2 SD	Mean	2 SD	Mean	2 SD	Mean	2 SD	Mean	2 SD
Before Faraday cup replacement												
1	13	Nov. '14	1.141841	3	1.141807	10	1.141863	18	1.141886	19	1.14184	21
2	12	Dec. '14–Jan. '15	1.141837	5.5	1.141821	22	1.141859	14	1.14187	19	1.141847	12
3	15	Feb. '15	1.141835	5.1	1.141818	24	1.141853	11	1.141862	10	1.141844	23
4	13	Mar. '15	1.141836	5.9	1.141807	15	1.141848	10	1.141864	17	1.141832	17
Total	53	Nov. '14–Mar. '15	1.141837	6.4	1.141813	21	1.141856	17	1.14187	23	1.141841	21
After Faraday cup replacement												
5	4	Apr. '15	1.141836	3.1	1.141808	9	1.141873	2.3	1.141768	4	1.141979	3.2
6	11	Jun. '15	1.141837	4.8	1.141808	8.5	1.141869	5.3	1.141785	11	1.141953	15
7	8	Jun. '15	1.141838	3.4	1.14181	8.5	1.141872	4.6	1.141794	7.1	1.141948	11
Total	23	Apr. '15–Jun. '15	1.141837	4.1	1.141809	8.3	1.14187	5.4	1.141785	18	1.141956	23
Total	76	Nov. '14–Jun. '15	1.141837	5.8	1.141812	19	1.14186	19	1.141844	72	1.141876	95

After the replacement of six Faraday cups, the mean $^{142}Nd/^{144}Nd$ values obtained by the static method drastically shifted from the values obtained through campaigns 1–4 (Fig. 2.1). In addition, the isotope ratios obtained from Jumps 1 and 2 measurements were clearly distinct from each other, and neither matched the dynamic method. The inconsistency is most likely caused by the deterioration of three Faraday cups (C, H1, and H2), which were not replaced in April 2015, but a year earlier, before the initiation of Nd isotope measurements in this study. Roth et al. (2013) and Carlson (2014)

demonstrated similar long-term measurements for $^{142}Nd/^{144}Nd$ including nine (all) Faraday cup replacements. They showed that the $^{142}Nd/^{144}Nd$ ratio obtained just after the nine Faraday cup replacements was consistent with the value obtained at the time of installation. During campaigns 5–7, the isotope ratios obtained with the static method showed a linear decline in Jump 1 and increase in Jump 2. This result suggests that the observed isotopic shift represents the time-related deterioration of Faraday cups.

Our results suggest that high-precision Nd isotope analysis at a sub-10 ppm level with the static method cannot be achieved when all Faraday cups are not fresh. On the other hand, the values obtained from the dynamic method showed much lower fluctuation during the entire analytical period (Sections 2.3.2 and 2.3.3). Thus, measurements of $^{142}Nd/^{144}Nd$ values using the dynamic method are strongly recommended unless all Faraday cups are fresh, as previously mentioned (Thirlwall and Anczkiewicz, 2004; Boyet and Carlson, 2007; O'Neil et al., 2008; Roth et al., 2013).

2.3.2 Comparison of the multistatic and dynamic methods

In some previous studies, the analytical reproducibilities of Nd isotope analyses by the dynamic method were directly compared with those obtained by the static method (Thirlwall, 1991; Avanzinelli et al., 2005; Boyet and Carlson 2007; O'Neil et al., 2008; Roth et al., 2013). Likewise, Brandon et al. (2009) compared the reproducibilities of Nd isotope analyses obtained by the multistatic and static methods. All these studies concluded that the dynamic or multistatic method achieved reproducibilities superior to those of the static method. However, no previous studies have directly compared the

results of Nd isotope measurements by the dynamic and multistatic methods operated under the same analytical conditions.

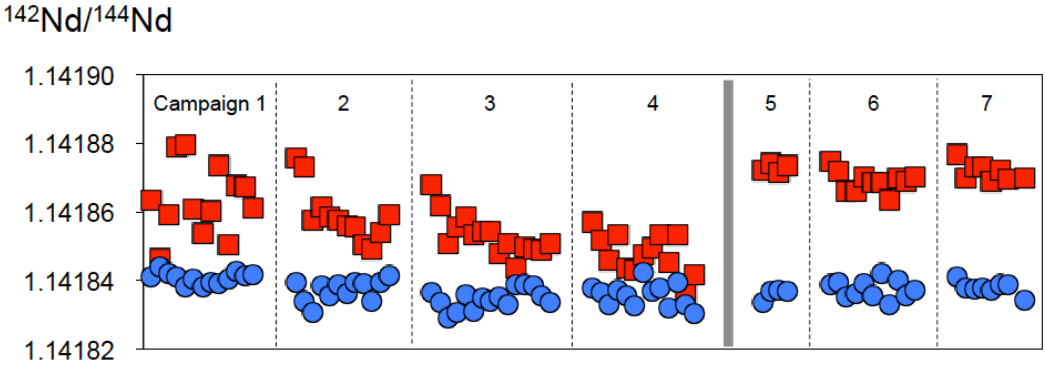

Fig. 2.2 *Fluctuation in Nd isotope ratios obtained by the multistatic method (filled squares) and dynamic method (filled circles) in the repeated analysis for JNdi-1 during analytical campaigns 1–7. Dashed and bold lines are the same as those in Fig. 2.1.*

We compared the results of isotope measurements with the dynamic and multistatic methods by the two-jump cup configuration. The analytical reproducibilities and $^{142}Nd/^{144}Nd$ values, averaged in each analytical campaign, with the dynamic and multistatic methods are presented in Table 2.2. Fig. 2.2 shows the isotopic fluctuation of $^{142}Nd/^{144}Nd$ obtained by both multistatic and dynamic methods during the entire analytical period. In the case of the multistatic method, a gradual decline in Nd isotope ratios could be observed before April 2015, while the extent of fluctuation was reduced after the replacement of six Faraday cups. Consequently, the reproducibility of $^{142}Nd/^{144}Nd$ in campaigns 5–7 with the multistatic method (±5.4 ppm) was three times better than that in campaigns 1–4 (±17 ppm). By contrast, the reproducibility of

$^{142}Nd/^{144}Nd$ with the dynamic method in campaigns 5–7 (±4.1 ppm) improved by a factor of 1.6 relative to that in campaigns 1–4 (±6.4 ppm). The results show that the multistatic method is more susceptible to the aging of the Faraday cups as compared to the dynamic method in the case the Faraday cups that were not canceled by the multistatic method (L3 and H3 for $^{142}Nd/^{144}Nd$ ratio) have deteriorated. It should be noted that the typical internal precision obtained by the multistatic method was ±1–3 ppm, which is superior to that obtained by the static method. This implies that the multistatic method can reduce the effect of Faraday cup aging within each measurement, resulting in the improvement of reproducibility as compared with the static method.

As described earlier, we define the Faraday cup efficiency α as a simplified form of Eq. 2.1. The excellent long-term reproducibility of $^{142}Nd/^{144}Nd$ with the dynamic method implies that the last term including α in Eq. 2.5 can be ignored, that is, Eq. 2.6 is approximated to be unity. This supports the validity of Eq. 2.1.

The clear differences between the reproducibilities obtained by three analytical modes, the static, dynamic, and multistatic methods, can be explained by the propagation of analytical errors accompanying the Faraday cup deterioration. Here, we introduce a parameter M, which represents parts per 10^6 deviation from an "apparent" isotope ratio ($R_{app.}$) obtained by ignoring Faraday cup deterioration from the true isotope ratio (R_{true}):

$$M = (R_{app.} / R_{true} - 1) \times 10^6 \qquad (2.11).$$

In the case of ^{142}Nd/^{144}Nd measurement with the static method, M can be determined as follows:

$$M_{142/144}^{static} = \left\{\left(\frac{\alpha_{L3}}{\alpha_{L1}}\right)\left(\frac{\alpha_{L1}}{\alpha_{H1}}\right)^{f_1} - 1\right\}\times 10^6 \qquad (2.12).$$

Likewise, $M_{142/144}^{dynamic}$ and $M_{142/144}^{multistatic}$ are expressed as follows:

$$M_{142/144}^{dynamic} = \left\{\left(\frac{\alpha_{L1}}{\alpha_{H1}}\right)^{1+f_1} - 1\right\}\times 10^6 \qquad (2.13)$$

$$M_{142/144}^{multistatic} = \left[\frac{1}{2}\left\{\left(\frac{\alpha_{L3}}{\alpha_{L1}}\right)\left(\frac{\alpha_{L1}}{\alpha_{H1}}\right)^{f_1} + \left(\frac{\alpha_{L1}}{\alpha_{H1}}\right)\left(\frac{\alpha_{H1}}{\alpha_{H3}}\right)^{f_1}\right\} - 1\right]\times 10^6 \qquad (2.14).$$

For comparison, we determined $M_{142/144}$ for the case of the three-jump multistatic method of Caro et al. (2006):

$$M_{142/144}^{3-line} = \left[\frac{1}{3}\left\{\left(\frac{\alpha_{L3}}{\alpha_{L1}}\right)\left(\frac{\alpha_{L1}}{\alpha_{H1}}\right)^{f_1} + \left(\frac{\alpha_{L2}}{\alpha_{CC}}\right)\left(\frac{\alpha_{CC}}{\alpha_{H2}}\right)^{f_1} + \left(\frac{\alpha_{L1}}{\alpha_{H1}}\right)\left(\frac{\alpha_{H1}}{\alpha_{H3}}\right)^{f_1}\right\} - 1\right]\times 10^6 \quad (2.15).$$

Fig. 2.3 shows the variation in $M_{142/144}$ as a function of α_{L1}. The $M_{142/144}^{static}$ value increases from 0 to 600 ppm along with the change in α_{L1} from 1 to 0.9997. By contrast, the variations for $M_{142/144}^{multistatic}$ and $M_{142/144}^{3-line}$ are much reduced to 150 ppm and 100 ppm, respectively, at α_{L1} = 0.9997. As displayed in Fig. 2.3b, similar results are obtained for $M_{142/144}^{static}$, $M_{142/144}^{multistatic}$, and $M_{142/144}^{3-line}$ along with the change in α_{H1}.

These results suggest that $M_{142/144}$ in the multistatic method is several times less susceptible to the fluctuation in Faraday cup degradation when compared to the static method, resulting in the observed improvement in the reproducibilities for Nd isotope ratios in the multistatic method. Nonetheless, $M_{142/144}^{multistatic}$ and $M_{142/144}^{3-line}$ values exceed 10 ppm when α_{L1} < 0.9999, and are thus, significantly larger than the reproducibility of $^{142}Nd/^{144}Nd$ measurements (<10 ppm) in the multistatic method obtained in this study and previous studies. Note that Yokoyama et al. (2015) demonstrated that the α value of a Faraday cup became less than 0.9995 after consecutive measurements of Sr isotope ratios for more than four years.

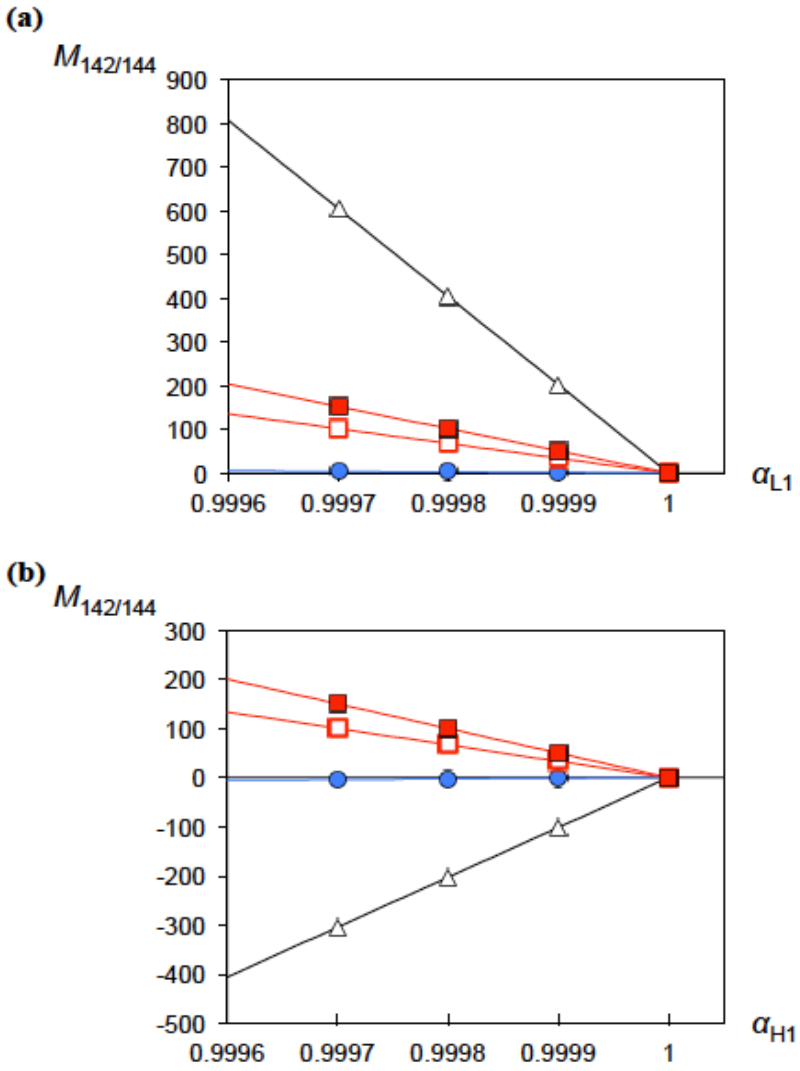

Fig. 2.3 *Relationship between $M_{142/144}$ and Faraday cup efficiencies of (a) α_{L1} and (b) α_{H1}. M stands for parts per 10^6 deviation of apparent $^{142}Nd/^{144}Nd$ ratio ($R_{app.}$) obtained by ignoring Faraday cup deterioration from the true isotope ratio (R_{true}). Symbols are the same as those in Figs. 2.1–2.2 (static: open triangles, dynamic: filled circles, two-jump multistatic: filled squares). Open squares represent the case of three-jump multistatic method by Caro et al. (2006).*

On the other hand, the variation in $M_{142/144}^{dynamic}$ is markedly small, being only 4 ppm at α_{L1} = 0.9997, suggesting that the dynamic method can almost completely cancel

the effect of Faraday cup degradation. This helps to improve both the reproducibility and accuracy of the Nd isotope measurement compared to the static and multistatic methods, because α would fluctuate within a single analytical campaign once the degradation of Faraday cups had begun.

Several previous studies (Caro et al., 2006; Bennett et al., 2007; Devaille et al., 2007; Brandon et al., 2009; Devaille et al., 2009) have performed Nd isotope measurements with the three-jump multistatic method and reported an excellent reproducibility of ±2 ppm for $^{142}Nd/^{144}Nd$ ratio. The isotopic shift during long-term isotope measurements has not been reported in these studies; however, we infer that the three-jump multistatic method can also be affected by Faraday cup deterioration. To conclude, such a high-precision measurement can be achieved with the static and multistatic methods only when Faraday cups for collecting ^{142}Nd, ^{144}Nd, and ^{146}Nd are fresh ($\alpha \approx 1$).

2.3.3 Isotopic shift in the dynamic method

As discussed above, the dynamic method is considered to be the most effective to cancel out the degradation of the Faraday cups. However, with long-term measurements, isotope ratios obtained by the dynamic method showed a time-related shift (Fig. 2.4a). The largest isotopic drift was observed between campaigns 1 and 3, indicating a 4.2 ppm shift over three months. The difference between the isotopic ratios obtained in campaigns 1 and 2–7 are significant and was statistically confirmed by the *t*-test ($p < 0.05$). One possible cause for the isotopic shift is that the dynamic method can be

affected by the Faraday cup deterioration. This trend is similar to the isotopic shift observed in the static (Section 2.3.1) and multistatic methods (Section 2.3.2) due to the Faraday cups degradation. This is evidently caused by the degradation of Faraday cups because Eq. 2.5, the equation for the dynamic method with fractionation correction by the exponential law, includes the term for Faraday cup efficiencies.

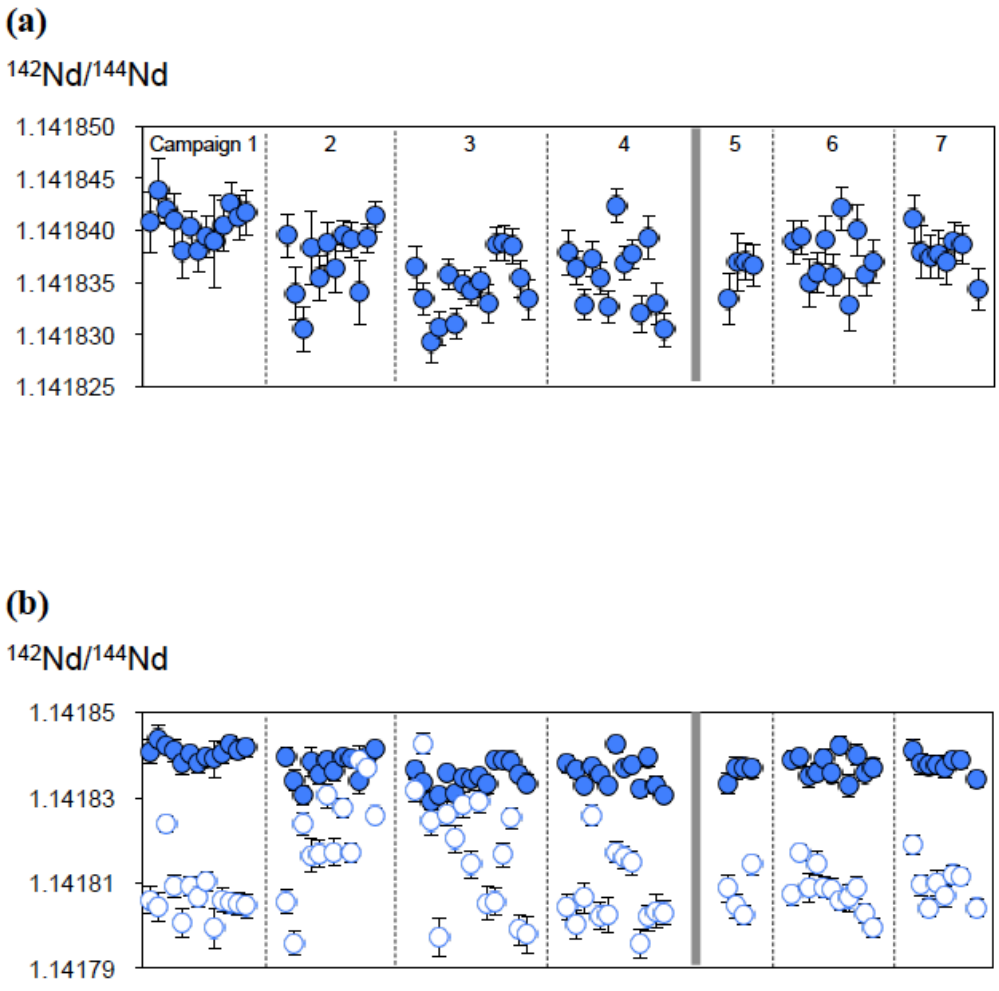

Fig. 2.4 *Fluctuation in Nd isotope ratios obtained by the dynamic method with (a) the exponential law and (b) the power law (open circles). In (b), those obtained by the exponential law (filled circles) are plotted for comparison.*

Alternatively, the observed isotopic shift could be induced by the incomplete correction for mass-dependent isotopic fractionation during measurement. In contrast to the exponential law correction, the dynamic method with the power law correction mathematically cancels out the Faraday cup efficiencies completely (Eq. 2.4). As shown in Fig. 2.4b and Table 2.2, we also calculated Nd isotope ratios with the power law correction using this equation. In the power law correction, campaign 1 showed the best reproducibility among the campaigns before Faraday cup replacement (Campaigns 1–4). This trend implies that mass-dependent isotopic fractionation was relatively stable in campaign 1, thereby inducing the isotopic shift with the calculation by the exponential law.

To conclude, for high-precision Nd isotope analysis, ensuring that the Faraday cups are as fresh as possible is recommended, and that they avoid the unusual mass-dependent isotopic fractionation caused by the sample loading and ion source condition, even for measurements with the dynamic method, in order to avoid a small but resolvable shift in isotope ratios caused by the Faraday cup deterioration. Finally, we plot the $^{142}Nd/^{144}Nd$ ratios obtained by the dynamic method with the power law correction (open circles) and with the exponential law correction (filled circles) against the raw $^{146}Nd/^{144}Nd$ ratio observed in a single isotope measurement in Fig. 2.5. A clear negative correlation is observed for the case of the power law correction, while the $^{142}Nd/^{144}Nd$ ratio with the exponential law is constant irrespective of the variation in the $^{146}Nd/^{144}Nd$ ratio. This strongly suggests that the exponential law is more appropriate than the power law correction, which is consistent with previous studies (Thirlwall and

Anczkiewicz, 2004; Avanzinelli et al., 2005).

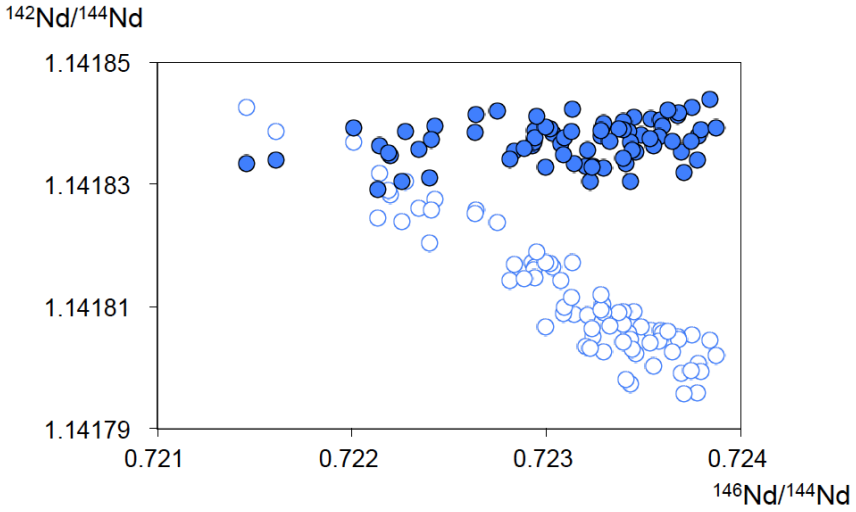

Fig. 2.5 *Plots of $^{142}Nd/^{144}Nd$ ratio obtained with the dynamic method versus the observed $^{146}Nd/^{144}Nd$ ratio. Symbols are the same as in Fig. 2.4.*

2.3.4 Analytical reproducibilities of $^{148}Nd/^{144}Nd$ and $^{150}Nd/^{144}Nd$ ratios

In addition to $^{142}Nd/^{144}Nd$, the two-jump cup configuration for Nd isotope measurements can obtain $^{148}Nd/^{144}Nd$ and $^{150}Nd/^{144}Nd$ ratios with the dynamic method simultaneously. We performed the long-term (over eight months) isotope measurements of $^{148}Nd/^{144}Nd$ and $^{150}Nd/^{144}Nd$ ratios, as well as $^{142}Nd/^{144}Nd$ ratio, with the dynamic method. The analytical reproducibilities during the entire analytical period were ±5.3 ppm for $^{148}Nd/^{144}Nd$ and ±14 ppm for $^{150}Nd/^{144}Nd$. After replacing the Faraday cups in April 2015, we obtained a 1.7 times better reproducibility (±8.8 ppm) in $^{150}Nd/^{144}Nd$ compared to those obtained before the Faraday cups' replacement (±15 ppm).

This method with the power law for $^{148}Nd/^{144}Nd$ and $^{150}Nd/^{144}Nd$ ratios was first introduced by Wendt and Haase (1998), however, no results regarding the long-term

reproducibilities were reported, because these isotope ratios were not essentially useful for the isotope measurements of terrestrial rocks. Recently, nucleosynthetic Nd isotope anomalies of bulk meteorites relative to terrestrial rocks have been reported (Boyet and Carlson, 2005; Andreasen and Sharma, 2006; Carlson et al., 2007; Gannoun et al., 2011). These previous studies conducted $^{148}Nd/^{144}Nd$ and $^{150}Nd/^{144}Nd$ ratio measurements with the static method. The reproducibilities of these ratios for a long period have not been reported in previous studies. The reproducibilities for $^{148}Nd/^{144}Nd$ and $^{150}Nd/^{144}Nd$ ratios obtained by the static method in previous studies and by the dynamic method in this study are compared in Table 2.3. After Faraday cup replacement (n = 23), reproducibilities are generally 1.5–4.1 times better than those obtained in previous studies.

Table 2.3 *Mean $^{148}Nd/^{144}Nd$ and $^{150}Nd/^{144}Nd$ ratios and reproducibilities (2 SDs) of the repeated analysis for JNdi-1 measured with the dynamic method, compared to those obtained by the previous studies with the static method.*

Campaign	N		$^{148}Nd/^{144}Nd$		$^{150}Nd/^{144}Nd$	
			Mean	2 SD (ppm)	Mean	2 SD (ppm)
This study (Dynamic)						
Before Faraday cup replacement						
1	13	Nov. '14	0.241581	4.2	0.236455	8.5
2	12	Dec. '14 – Jan. '15	0.241581	4.0	0.236454	13
3	15	Feb. '15	0.241580	4.6	0.236452	11
4	13	Mar. '15	0.241581	3.3	0.236453	13
Total	53	Nov. '14 – Mar. '15	0.241581	4.9	0.236453	15
After Faraday cup replacement						
5	4	Apr. '15	0.241580	2.6	0.236453	6.1
6	11	Jun. '15	0.241581	4.9	0.236454	7.7
7	8	Jun. '15	0.241581	5.6	0.236455	10
Total	23	Apr. '15 – Jun. '15	0.241581	6.3	0.236454	8.8
Total	76	Nov. '14 – Jun. '15	0.241581	5.3	0.236453	14
Previous studies (Static)						
Boyet and Carlson (2005)	8		0.241577	17	0.236445	21
Andreasen and Sharma (2006)	23		0.241578	11	0.236447	16
Carlson et al. (2007)	15		0.241583	12	0.236456	13
Gannoun et al. (2011)	18		0.241587	26	0.236462	21

2.4 Concluding Remarks

In this study, we investigated the influence of Faraday cup deterioration on the high-precision Nd isotope measurements with TIMS by using the static, dynamic, and multistatic methods. Throughout this study, we reached the following four conclusions.

(1) The analytical reproducibilities obtained in the static method were inferior to those reported in previous studies due to the Faraday cups deterioration. Our results suggest that high-precision Nd isotope analysis at a sub-10 ppm level (2 SD) with the static method cannot be achieved when all Faraday cups are not fresh.

(2) The Nd isotope ratios obtained by the multistatic method were more susceptible to the Faraday cups deterioration compared to those obtained by the dynamic method.

(3) In the long-term measurements, Nd isotope ratios obtained by the dynamic method showed a small but resolvable shift. Our results were the first ones to show that Nd isotope measurements by the dynamic method with exponential law can be affected by Faraday cup deterioration or incomplete mass-dependent isotopic fractionation correction at the sub-10 ppm level.

(4) In addition to the $^{142}Nd/^{144}Nd$ ratio, the two-jump cup configuration for Nd isotope measurements provided $^{148}Nd/^{144}Nd$ and $^{150}Nd/^{144}Nd$ ratios with the dynamic

method simultaneously. The reproducibilities for $^{148}Nd/^{144}Nd$ and $^{150}Nd/^{144}Nd$ ratios obtained in this study after the Faraday cup replacement (n = 23) are ±6.3 and ±8.8 ppm (2 SDs), respectively, which are 1.5–4.1 times better than those obtained in previous studies.

References

Andreasen, R., Sharma, M., 2006. Solar nebula heterogeneity in p-process samarium and neodymium isotopes. Science 314, 806-809.

Avanzinelli, R., Boari, E., Conticelli, S., Francalanci, L., Guarnieri, L., Perini, G., Petrone, C.M., Tommasini, S., Ulivi, M., 2005. High precision Sr, Nd, and Pb isotopic analyses using the new generation Thermal Ionisation Mass Spectrometer ThermoFinnigan Triton-Ti (R). Periodico Di Mineralogia 74, 147-166.

Bennett, V.C., Brandon, A.D., Nutman, A.P., 2007. Coupled ^{142}Nd–^{143}Nd isotopic evidence for Hadean mantle dynamics. Science 318, 1907-1910.

Boyet, M., Carlson, R.W., 2005. ^{142}Nd evidence for early (> 4.53 Ga) global differentiation of the silicate Earth. Science 309, 576-581.

Boyet, M., Carlson, R.W., 2007. A highly depleted moon or a non-magma ocean origin for the lunar crust? Earth and Planetary Science Letters 262, 505-516.

Boyet, M., Carlson, R.W., Borg, L.E., Horan, M., 2015. Sm–Nd systematics of lunar ferroan anorthositic suite rocks: Constraints on lunar crust formation. Geochimica et Cosmochimica Acta 148, 203-218.

Boyet, M., Carlson, R.W., Horan, M., 2010. Old Sm-Nd ages for cumulate eucrites and redetermination of the solar system initial ^{146}Sm/^{144}Sm ratio. Earth and Planetary Science Letters 291, 172-181.

Brandon, A.D., Lapen, T.J., Debaille, V., Beard, B.L., Rankenburg, K., Neal, C., 2009. Re-evaluating ^{142}Nd/^{144}Nd in lunar mare basalts with implications for the early

evolution and bulk Sm/Nd of the Moon. Geochimica et Cosmochimica Acta 73, 6421-6445.

Carlson, R.W., Boyet, M., Horan, M., 2007. Chondrite barium, neodymium, and samarium isotopic heterogeneity and early earth differentiation. Science 316, 1175-1178.

Caro, G., Bourdon, B., 2010. Non-chondritic Sm/Nd ratio in the terrestrial planets: Consequences for the geochemical evolution of the mantle crust system. Geochimica et Cosmochimica Acta 74, 3333-3349.

Caro, G., Bourdon, B., Birck, J.L., Moorbath, S., 2006. High-precision $^{142}Nd/^{144}Nd$ measurements in terrestrial rocks: Constraints on the early differentiation of the Earth's mantle. Geochimica et Cosmochimica Acta 70, 164-191.

Caro, G., Bourdon, B., Halliday, A.N., Quitte, G., 2008. Super-chondritic Sm/Nd ratios in Mars, the Earth and the Moon. Nature 452, 336-339.

Debaille, V., Brandon, A.D., O'Neill, C., Yin, Q.Z., Jacobsen, B., 2009. Early martian mantle overturn inferred from isotopic composition of nakhlite meteorites. Nature Geoscience 2, 548-552.

Debaille, V., Brandon, A.D., Yin, Q.Z., Jacobsen, B., 2007. Coupled ^{142}Nd–^{143}Nd evidence for a protracted magma ocean in Mars. Nature 450, 525-528.

Gannoun, A., Boyet, M., Rizo, H., El Goresy, A., 2011. ^{146}Sm–^{142}Nd systematics measured in enstatite chondrites reveals a heterogeneous distribution of ^{142}Nd in the solar nebula. Proceedings of the National Academy of Sciences of the United States of America 108, 7693-7697.

Makishima, A., Nakamura, E., 1991. Calibration of Faraday cup efficiency in a multicollector mass spectrometer. Chemical Geology 94, 105-110.

O'Neil, J., Carlson, R.W., Francis, D., Stevenson, R.K., 2008. Neodymium-142 evidence for hadean mafic crust. Science 321, 1828-1831.

Roth, A.S.G., Bourdon, B., Mojzsis, S.J., Touboul, M., Sprung, P., Guitreau, M., Blichert-Toft, J., 2013. Inherited ^{142}Nd anomalies in Eoarchean protoliths. Earth and Planetary Science Letters 361, 50-57.

Thirlwall, M.F., 1991. Long-term reproducibility of multicollector Sr and Nd isotope ratio analysis. Chemical Geology 94, 85-104.

Touboul, M., Walker, R.J., 2012. High precision tungsten isotope measurement by thermal ionization mass spectrometry. International Journal of Mass Spectrometry 309, 109-117.

Wendt, I., Haase, G., 1998. Dynamic double collector measurement with cup efficiency factor determination. Chemical Geology 146, 99-110.

Yokoyama, T., Fukami, Y., Okui, W., Ito, N., Yamazaki, H., 2015. Nucleosynthetic strontium isotope anomalies in carbonaceous chondrites. Earth and Planetary Science Letters 416, 46-55.

Chapter 3:
Assessment of the secondary instrumental fractionation in TIMS: Implication for high-precision Nd isotope analysis of geochemical samples

Abstract

In this study, we investigated the secondary instrumental fractionation in thermal ionization mass spectrometry (TIMS), which cannot be ignored in the extraordinary high-precision Nd isotope measurements. We performed multiple Nd isotope measurements (n = 125) for a standard material JNdi-1. We found small but resolvable isotopic fluctuations the obtained $^{142}Nd/^{144}Nd$, $^{148}Nd/^{144}Nd$, and $^{150}Nd/^{144}Nd$ ratios of JNdi-1 that cannot be eliminated by the normal mass fractionation correction using the $^{146}Nd/^{144}Nd$ ratio, most likely due to secondary instrumental fractionation induced by the accumulation of materials (e.g., H_3PO_4 activator) emitted from measured samples onto the surface of ion source assemblage. The effect of the secondary instrumental fractionation observed in the $^{142}Nd/^{144}Nd$ ratio can be corrected using the simultaneously measured $^{150}Nd/^{144}Nd$ ratio. After the second-order correction, the reproducibilities of $^{142}Nd/^{144}Nd$ ratio have been improved from ±5.6 ppm to ±4.2 ppm (2 SDs). The second-order correction method enables more precise and accurate isotopic measurements for terrestrial rocks that potentially possess variable $^{142}Nd/^{144}Nd$ ratios.

3.1 Introduction

Latest-generation thermal ionization mass spectrometry (TIMS) instruments, equipped with several improved systems (e.g., optimized ion optics), are now capable of obtaining extraordinary high-precision isotope ratios with precisions less than 5 ppm (2 SD). In particular, recent analytical improvements for Nd isotopic analysis with TIMS have achieved the highest level of analytical precisions (Caro et al., 2006). Neodymium is a light rare earth element including two radiogenic isotopes (^{142}Nd and ^{143}Nd) and five non-radiogenic isotopes (^{144}Nd, ^{145}Nd, ^{146}Nd, ^{148}Nd, and ^{150}Nd). A short-lived isotope ^{146}Sm decays to ^{142}Nd ($T_{1/2}$ = 103 Ma) and changes the ^{142}Nd/^{144}Nd ratio in rocks and minerals depending on the time and the Sm/Nd ratio. Therefore, ancient materials that formed when ^{146}Sm is alive (> ~4 Ga) show variations in ^{142}Nd/^{144}Nd ratios, which allow us to track the processes such as silicate melting and fractional crystallization that occurred in the early terrestrial mantle and/or crust. However, the isotopic deviations of ^{142}Nd/^{144}Nd ratios in these samples from the terrestrial standard are occasionally limited to be < ~5 ppm. In the determination of high-precision Nd isotope ratios with TIMS, it is getting more important for properly addressing some issues that occur during the operation of mass spectrometers (e.g., mass discrimination effects), all of which would cause systematically biased erroneous results.

Mass discrimination effects that occur in the ion source and mass analyzer can be corrected by assuming several empirical laws that formulate the mechanism of isotopic fractionation (e.g., exponential law). In Nd isotopic measurements with old-generation TIMS instruments (e.g., Finnigan MAT 262; Thermo Fischer Scientific,

USA), a residual correlation was observed between $^{142}Nd/^{144}Nd$ and $^{143}Nd/^{144}Nd$ ratios even if these isotopic ratios were corrected by the empirical laws (e.g., Sharma et al., 1996). This problem, called the secondary instrumental fractionation, represents the occurrence of a non-ideal isotopic fractionation that cannot be corrected by fractionation laws. The residual correlation between two Nd isotope ratios was observed for Nd standard measurements with the latest-generation TIMS instruments. For instance, Roth et al. (2014) reported correlations among multiple Nd isotopic ratios of Khariar alkaline rocks in India and concluded that the residual correlations should be monitored to improve the accuracy of $^{142}Nd/^{144}Nd$ ratios, although the cause responsible for the correlation is yet unidentified. To clarify the cause of isotopic fluctuation in $^{142}Nd/^{144}Nd$ ratio that possibly occurring in TIMS isotopic measurements is significant to obtain reliable isotopic data for geochemical samples. In this study, we investigated the secondary instrumental fractionation that occurred in high-precision Nd isotopic measurements of TIMS and propose a method that can correct the secondary fractionation to obtain high-precision $^{142}Nd/^{144}Nd$ ratios in rock samples.

.

3.2 Experimental

Neodymium was ionized with a double filament assembly using a zone-refined Re filament. Approximately 500 ng of a standard material JNdi-1 dissolved in 1 μL 6.4 M HCl was loaded on the evaporation filament. Subsequently, the sample was covered by 0.01 % H_3PO_4 (1–8 μL) as an activator. Neodymium isotopes were collected in two different cup configurations within a single measurement run as shown in Table 3.1, in which $^{142}Nd/^{144}Nd$, $^{143}Nd/^{144}Nd$, $^{148}Nd/^{144}Nd$, and $^{150}Nd/^{144}Nd$ ratios were obtained by the dynamic-multicollection method as described in Chapter 2.

Table 3.1 *Cup configuration and time settings for Nd isotope measurements with TIMS.*

	L4	L3	L2	L1	C	H1	H2	H3	H4	Integration time	Idle time
Jump 1	^{140}Ce	^{142}Nd	^{143}Nd	^{144}Nd	^{145}Nd	^{146}Nd	^{147}Sm	^{148}Nd	^{150}Nd	16.777 s	4.000 s
Jump 2		^{140}Ce		^{142}Nd	^{143}Nd	^{144}Nd	^{145}Nd	^{146}Nd	^{148}Nd	16.777 s	4.000 s

The total analytical time per single measurement took ~4.5 h including the idle time (4.000 s) between two magnet settings, baseline measurement (30 s) at the beginning of each block, beam focusing in every 3 blocks, and peak centering in every 5 blocks. The collection of Nd isotopes consisted of 16.777 s in each line, two lines in one cycle, 20 cycles in one block, and 18 blocks in a single measurement. Neodymium isotope ratios were corrected with the exponential law, assuming the relation of $^{146}Nd/^{144}Nd = 0.7219$. Mass interferences from Ce and Sm were monitored at ^{140}Ce (Jumps 1 and 2) and ^{147}Sm (Jump 1) by assuming $^{142}Ce/^{140}Ce = 0.12565$, $^{144}Sm/^{147}Sm = 0.20498$, $^{148}Sm/^{147}Sm = 0.74970$, and $^{150}Sm/^{147}Sm = 0.49219$.

The ion lens assemblage of TIMS was cleaned with a diluted detergent solution (RBS 50; Sigma-Aldrich, Germany) several times during the total analytical campaign.

Prior to the sample setting in the ion source housing of TIMS instrument, the source baking was conducted for 6–9 h.

3.3 Results and Discussion

3.3.1 Fluctuation of Nd isotopic ratios obtained by the dynamic method

The performance of Nd isotope analysis using TIMS instrument was evaluated by repeated measurements of the standard JNdi-1 conducted over 4 years (n = 125; April 2014–December 2018). During the course of this study, we obtained stabilized reproducibilities of Nd isotope ratios (±5.6, ±5.8, and ±14 ppm for $^{142}Nd/^{144}Nd$, $^{148}Nd/^{144}Nd$, and $^{150}Nd/^{144}Nd$, 2 SDs, respectively) for measurements of the standard JNdi-1. In more detail, however, there still remain several factors that can fluctuate the Nd isotope ratios obtained by the dynamic method.

One possibility responsible for the fluctuation of Nd isotope ratios is inadequate correction for the mass-dependent isotopic fractionation that occurred in the instrument. To evaluate the validity of the exponential law correction, we determined the mean fractionation factor for each single isotopic measurement (α_{mean}) that is defined by the following equation:

$$\alpha_{mean} = \ln\left\{\frac{R_{ref.}}{R_{mean}}\right\} / \ln\left(\frac{m_{146}}{m_{144}}\right) \quad (3.1)$$

where $R_{ref.}$ is the reference isotope ratio of $^{146}Nd/^{144}Nd$ = 0.7219, R_{mean} is the mean value of observed $^{146}Nd/^{144}Nd$ ratios in a single isotopic measurement, and m_{144} and m_{146} are the isotope masses for ^{144}Nd and ^{146}Nd, respectively. As shown in Fig. 3.1, α_{mean} values do not correlate with the resulting Nd isotope ratios obtained after the

exponential law correction, which is apparent from the low correlation coefficients (r^2 = 0.02 to 0.07).

Whereas the α_{mean} value is not a predominant factor that controls the fluctuation of Nd isotope ratios, we found that the extent of dispersion for mass fractionation factor within a single isotopic measurement has a relationship with the resulting Nd isotope ratios obtained after the exponential law correction. As shown in Fig. 3.1, the fluctuation of 2 SE values of raw $^{146}Nd/^{144}Nd$ ratios for individual isotopic measurements ($2\sigma_{146/144}$ values) is generally correlated with the observed Nd isotope ratios (r^2 = 0.24 to 0.41). In addition, $2\sigma_{146/144}$ values would fluctuate in several analytical campaigns (Fig. 3.2). Such an extent of dispersion of raw isotopic ratios is observed for Sr isotope measurements (represented as $2\sigma_{88/86}$) that were conducted with the same instrument during these campaigns.

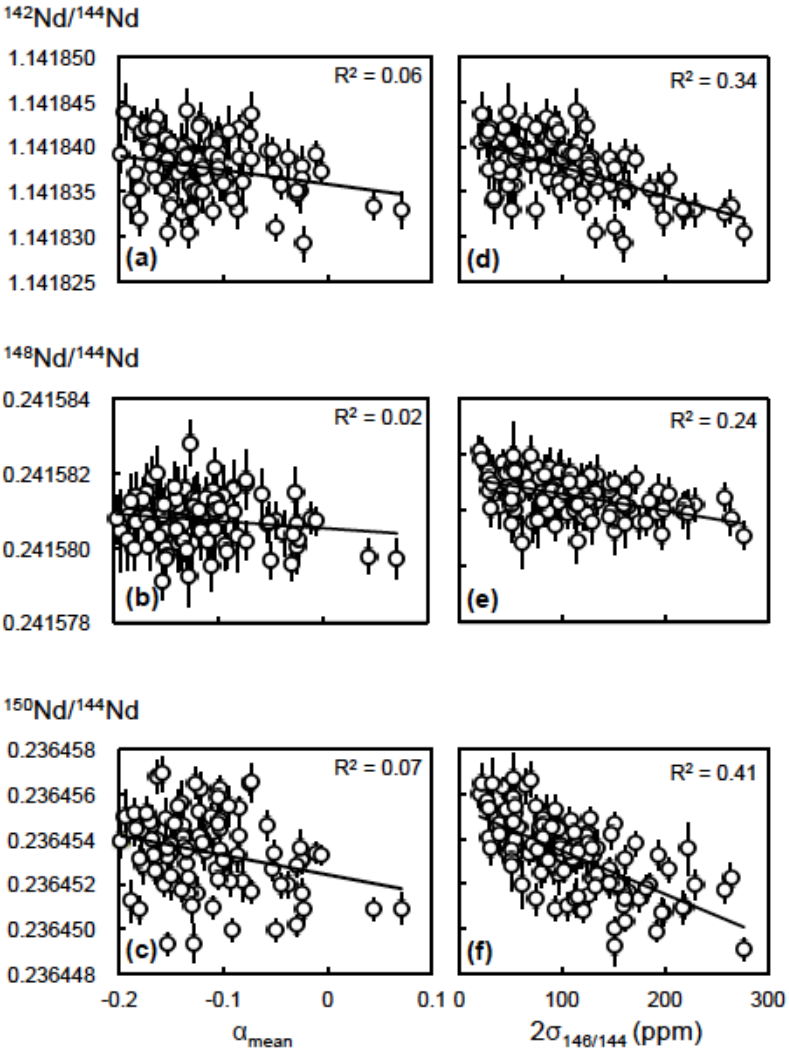

Fig. 3.1 *Plots of (a) $^{142}Nd/^{144}Nd$ ratio, (b) $^{148}Nd/^{144}Nd$ ratio, and (c) $^{150}Nd/^{144}Nd$ ratio versus the mean fractionation factors (α_{mean}) and (d) $^{142}Nd/^{144}Nd$ ratio, (e) $^{148}Nd/^{144}Nd$ ratio, and (f) $^{150}Nd/^{144}Nd$ ratio versus the dispersion of the mean fractionation factors ($2\sigma_{146/144}$). Error bars represent uncertainties for single isotopic measurements (2 SEs) and bold lines represent the regression lines.*

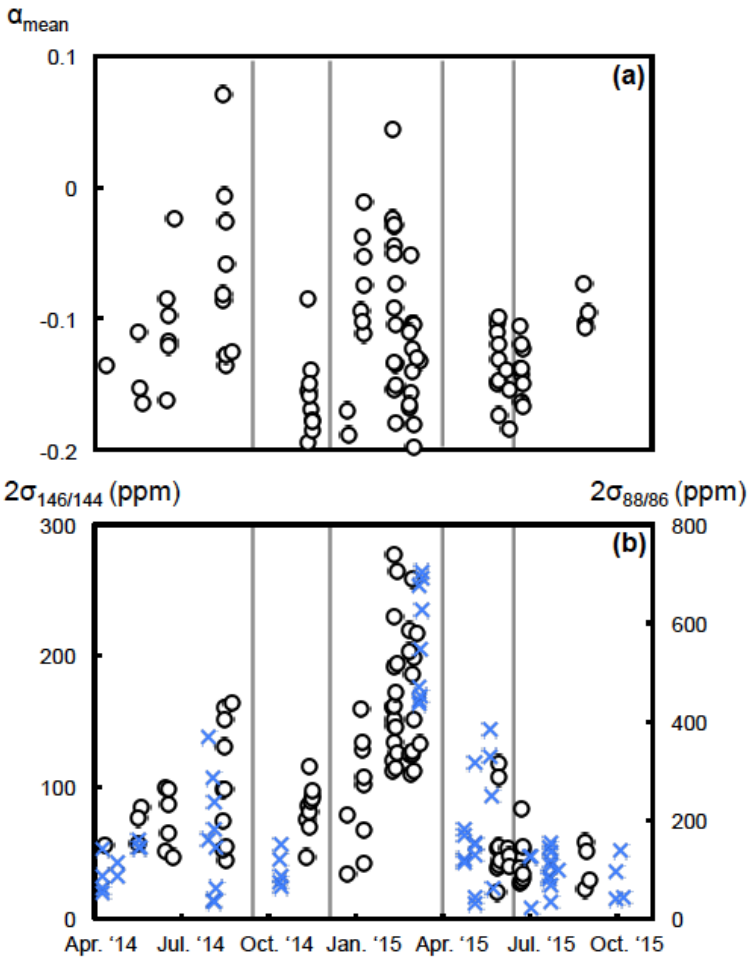

Fig. 3.2 *Fluctuation of (a) mean fractionation factors of Nd isotope measurements (α_{mean}) and (b) dispersion of the mean fractionation factors ($2\sigma_{146/144}$: circles) against the individual analytical campaigns during April '14 to October '15. In (b), dispersion of the mean fractionation factors for Sr isotope measurements ($2\sigma_{88/86}$: cross symbols) are plotted for comparison. Gray bars represent the timing of cleaning for the ion lens assemblage.*

Obviously, subtle differences in the sample loading technique and filament heating condition are not responsible for the variation of $2\sigma_{88/86}$ and $2\sigma_{146/144}$ values. Alternatively, here we postulate that the variation of $2\sigma_{146/144}$ values in the overall

campaigns is caused by the modification of mass fractionation mechanism in the ion lens system of the TIMS instrument. Gray bars in Fig. 3.2 represent the timing of ion source cleaning and baking that were conducted in between the each individual campaign. The $2\sigma_{146/144}$ values of the certain analytical campaigns gradually increase from the beginning toward the end of individual campaigns, which then drastically decrease at the beginning of the next campaign when the ion source is clean. This observation implies that the accumulation of materials onto the surface of ion source assemblage has modified the mass fractionation mechanism that resulted in the increase of $2\sigma_{146/144}$ values. Some of the activators used in the isotopic analyses with our TIMS instrument, specifically for diluted H_3PO_4 applied to the measurements of Sr, Nd, and Pb isotopes, are less volatile and possess relatively high electric conductivity. If some aliquot of H_3PO_4 remains on the surface of ion lens assemblage during measurements, an electrical circuit could be established on the focus plates. Consequently, the focal properties and the energy of Nd ions emitted from the Re filaments are modified. Therefore, we consider that the variable $2\sigma_{146/144}$ values were caused by the unstable focal properties of source lenses due to the accumulation of H_3PO_4.

3.3.2 Covariation of $^{142}Nd/^{144}Nd$, $^{148}Nd/^{144}Nd$, and $^{150}Nd/^{144}Nd$ ratios

Here we discuss why the increase of $2\sigma_{146/144}$ values resulted in the systematic decrease of $^{142}Nd/^{144}Nd$, $^{148}Nd/^{144}Nd$, and $^{150}Nd/^{144}Nd$ ratios in the dynamic method. We divided all measurements into three groups based on $2\sigma_{146/144}$ values (*in caption of Fig. 3.3*). Fig. 3.3 presents the diagrams plotting two Nd isotopic ratios ($^{150}Nd/^{144}Nd$

versus $^{142}Nd/^{144}Nd$ and $^{150}Nd/^{144}Nd$ versus $^{148}Nd/^{144}Nd$) for JNdi-1, both of which show positive correlations. In addition, the data from the distinct groups were separately plotted on these diagrams. We propose major two possibilities that are responsible for the observed linear trends in Fig. 3.3: (i) correlation of analytical errors and (ii) secondary instrumental fractionation.

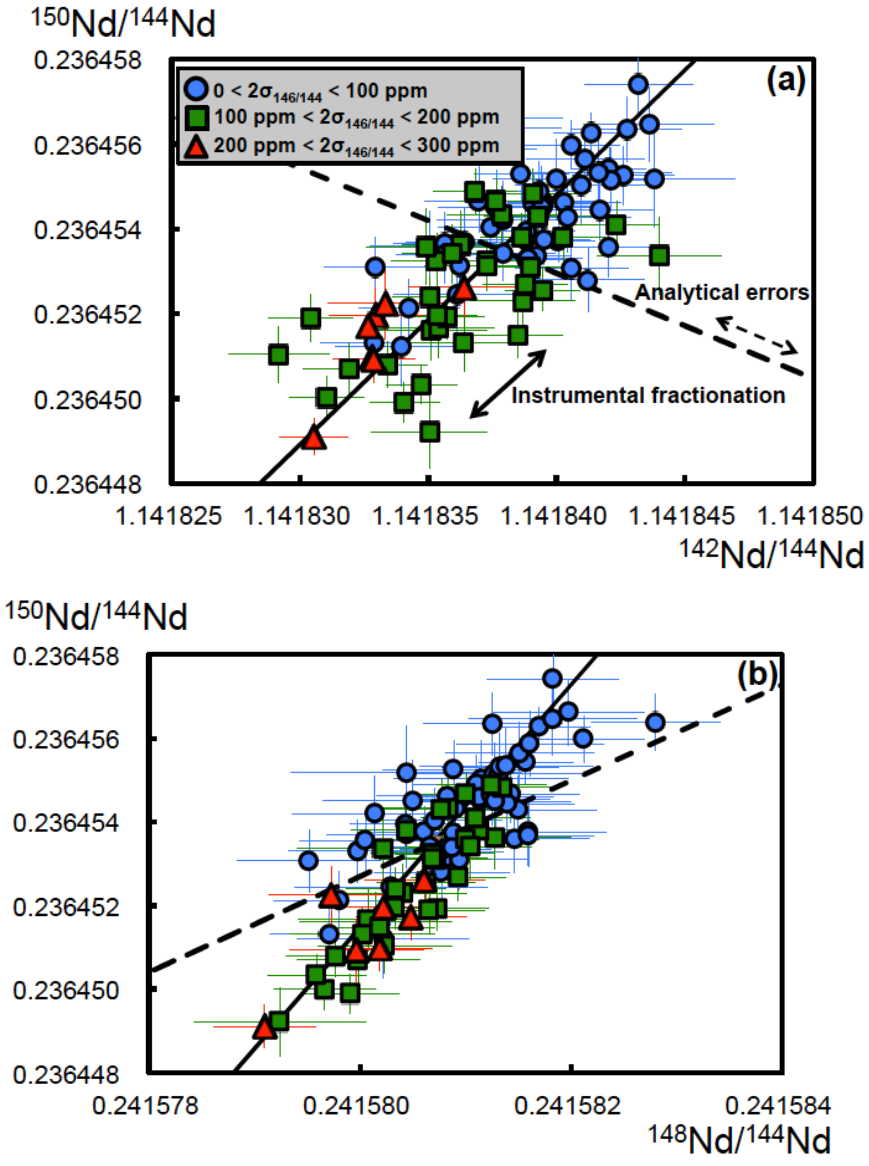

Fig. 3.3 *Diagrams of $^{150}Nd/^{144}Nd$ ratio versus (a) $^{142}Nd/^{144}Nd$ and (b) $^{148}Nd/^{144}Nd$ ratios. Each line represents the predicted slope (bold lines, secondary instrumental fractionation; dashed lines, analytical errors). Each symbol represents the ranges for the dispersion of mean fractionation factors (circles, $0 < 2\sigma_{146/144} < 100$ ppm; squares, $100 \text{ ppm} < 2\sigma_{146/144} < 200$ ppm; triangles, $200 \text{ ppm} < 2\sigma_{146/144} < 300$ ppm). Error bars represent uncertainties for single isotopic measurements (2 SEs).*

In our dynamic Nd isotope analysis, equation deriving the $^{150}Nd/^{144}Nd$ ratio with the exponential law correction includes the $^{142}Nd/^{144}Nd$ and $^{148}Nd/^{144}Nd$ ratios determined in the identical measurement cycle (Chapter 2). This implies that the analytical error of $^{150}Nd/^{144}Nd$ ratio correlate with those of $^{142}Nd/^{144}Nd$ and $^{148}Nd/^{144}Nd$ ratios. To assess this possibility, we conducted a Monte-Carlo simulation for statistically determining the analytical errors of $^{142}Nd/^{144}Nd$, $^{148}Nd/^{144}Nd$, and $^{150}Nd/^{144}Nd$ ratios.

In the simulation, we considered ion beams of Nd ($I_{i,j}$) in volts given by random variables, where i = 142, 144, 146, 148, and 150 for ^{142}Nd, ^{144}Nd, ^{146}Nd, ^{148}Nd, and ^{150}Nd, and j = 1 and 2 for Jumps 1 and 2, respectively. Each $I_{i,j}$ value is independent and normally distributed with a fixed mean of $\mu_{i,j}$ and a standard deviation of $\sigma_{i,j}$, which are governed by the following equation;

$$\sigma_{i,j}{}^2 = a + b\mu_{i,j} \quad (3.2)$$

$$a = \frac{4kTR}{\Delta t}, \quad b = \frac{eR}{\Delta t} \quad (3.3)$$

where a and b represent specified error parameters for the Johnson-Nyquist noise in the amplifiers and the counting statistics, and k and e are the Boltzmann constant (= 1.380654 × 10^{-23} J/K) and the elementary charge (= 1.602176487 × 10^{-19} C), respectively (Dodson, 1969). The resistance R (= 10^{11} Ω), the temperature T (= 300 K), and the integration time Δt (= 16 s) are derived from the properties for the mass spectrometer in this study. For simplification, we assumed that $\mu_{i,1} = \mu_{i,2}$, and that Nd isotope ratios are equal to the average values of this study: $\mu_{142,j}/\mu_{144,j}$ = 1.1418376, $\mu_{148,j}/\mu_{144,j}$ = 0.2415807, $\mu_{150,j}/\mu_{144,j}$ = 0.2364534 respectively. In addition, we ignored the influence of mass fractionation during TIMS measurements, so that the $\mu_{146,j}/\mu_{144,j}$ ratio was fixed to be 0.7219 throughout the calculation. We generated 360 sets of $I_{i,j}$ values for obtaining a set of (^{142}Nd/^{144}Nd)$_{corr.}$, (^{148}Nd/^{144}Nd)$_{corr.}$, and (^{150}Nd/^{144}Nd)$_{corr.}$ ratios. The error correlations among ^{142}Nd/^{144}Nd, ^{148}Nd/^{144}Nd, and ^{150}Nd/^{144}Nd ratios were evaluated by producing 100 sets of (^{142}Nd/^{144}Nd)$_{corr.}$, (^{148}Nd/^{144}Nd)$_{corr.}$, and (^{150}Nd/^{144}Nd)$_{corr.}$ ratios.

We simulated three cases in which $\mu_{142,j}$ = 1.0, 5.0, and 10 volts (Fig. 3.4). In all cases, we observed negative and positive correlations in the ^{150}Nd/^{144}Nd versus ^{142}Nd/^{144}Nd and ^{150}Nd/^{144}Nd versus ^{148}Nd/^{144}Nd diagrams, respectively, which represent the covariation of Nd isotope ratios caused by analytical errors. The slopes of error correlations determined from the datasets of $\mu_{142,j}$ = 5.0 are –0.25 and 1.14 for the correlations in Fig 3.4. Consequently, the error correlations are shown as dashed lines in Fig. 3.3, both of which are clearly distinguishable from the trends for actual measurement plots. Therefore, we conclude that analytical errors did not play a

dominant role in generating the observed linear trends in Fig. 3.3.

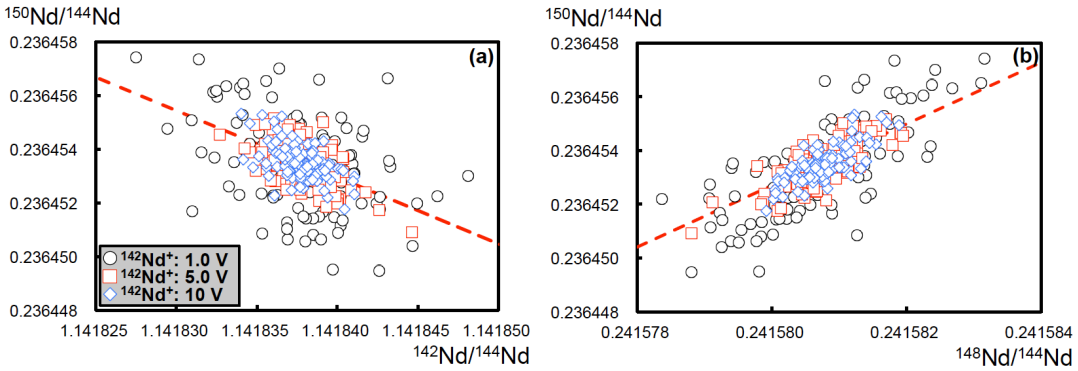

Fig. 3.4 *Diagrams of $^{150}Nd/^{144}Nd$ ratio versus (a) $^{142}Nd/^{144}Nd$ ratio and (b) $^{148}Nd/^{144}Nd$ ratio obtained with a Monte-Carlo simulation. All isotopic ratios were calculated with the equation of the dynamic method. Each symbol represents the average of the assumed beam intensity for $^{142}Nd^{+}$ through a single measurement (circles, 1.0 V; squares, 5.0 V; diamonds, 10 V). Dashed lines represent the regression lines for the case of $^{142}Nd^{+}$ = 5.0 V.*

Finally, we discuss the effect of secondary instrumental fractionation as for the reason of observed correlations between Nd isotope ratios. Caro et al. (2006) argued that the secondary instrumental fractionation was usually not observed in the latest-generation TIMS instruments, but it was induced by the same instrument as a result of ion optics effect in the Z-focus plate when the electron deflection magnet was set inside of the X-symmetry plates. The authors proposed that the presence of the secondary instrumental fractionation can be assessed by determining the second-order corrected $^{142}Nd/^{144}Nd$ ratio, $(^{142}Nd/^{144}Nd)_{2nd\text{-}corr.}$, using the following equations (Caro et al., 2006);

$$\left(\frac{^{142}\mathrm{Nd}}{^{144}\mathrm{Nd}}\right)_{2nd\text{-}corr.} = \left(\frac{^{142}\mathrm{Nd}}{^{144}\mathrm{Nd}}\right)_{corr.} \left\{\frac{\left(\frac{^{150}\mathrm{Nd}}{^{144}\mathrm{Nd}}\right)_{ref.}}{\left(\frac{^{150}\mathrm{Nd}}{^{144}\mathrm{Nd}}\right)_{corr.}}\right\}^{f_1} \quad (3.4)$$

$$f_1 = \frac{\ln\left(\frac{m_{142}}{m_{144}}\right)\ln\left(\frac{m_{142}}{m_{146}}\right)}{\ln\left(\frac{m_{150}}{m_{144}}\right)\ln\left(\frac{m_{150}}{m_{146}}\right)} \quad (3.5).$$

From these equations, we determined the correlations between (^{142}Nd/^{144}Nd)$_{corr.}$ versus (^{150}Nd/^{144}Nd)$_{corr.}$ assuming (^{142}Nd/^{144}Nd)$_{2nd\text{-}corr.}$ = 1.1418376 and (^{150}Nd/^{144}Nd)$_{ref.}$ = 0.2364534, which are the mean values of measured Nd isotope ratios. As shown in Fig. 3.3, the Nd isotopic ratios measured in this study are generally plotted along the obtained correlations, strongly suggesting the occurrence of the secondary instrumental fractionation. The secondary instrumental fractionation observed here was likely generated by unstable focal properties of ion source lenses. This effect was not due to the existence of the deflection magnet, but the accumulation of the solution emitted from filaments, which represent high electric conductivity. Therefore, accurate Nd isotopic ratios only can be obtained in the case that there is no secondary instrumental fractionation with the impurity of ion source lenses.

The effect of the secondary instrumental fractionation on the ^{142}Nd/^{144}Nd ratio can be corrected by adopting Eqs. 3.4–3.5. Consequently, the overall reproducibility of ^{142}Nd/^{144}Nd ratio was improved from ±5.6 to ±4.2 ppm (2 SDs) after the second-order correction. To conclude, precise determination of a non-radiogenic Nd isotope ratio,

especially for $^{150}Nd/^{144}Nd$ with the dynamic method, is indispensable for achieving extraordinary high-precision analysis of $^{142}Nd/^{144}Nd$ ratios for terrestrial samples. On the other hand, the second-order correction of $^{142}Nd/^{144}Nd$ ratios using the $^{150}Nd/^{144}Nd$ ratio does not work for meteorite samples, because unradiogenic Nd isotopic ratios ($^{145}Nd/^{144}Nd$, $^{148}Nd/^{144}Nd$, and $^{150}Nd/^{144}Nd$) are variable in bulk aliquots and components of chondrites and differentiated meteorites (Burkhardt et al., 2016). For instance, the difference of $^{150}Nd/^{144}Nd$ ratios between terrestrial samples and ordinary chondrites is 17–20 ppm. Such a difference is comparable to the difference of $^{150}Nd/^{144}Nd$ ratios (13 ppm) for the cases when the focal properties of ion optics are stable ($0 < 2\sigma_{146/144} < 100$ ppm) and unstable (200 ppm $< 2\sigma_{146/144} <$ 300 ppm). Therefore, to perform precise and accurate isotope measurements for meteorite samples, the secondary instrumental fractionation in ion focusing system should be suppressed. A simple and the most effective way to suppress the secondary instrumental fractionation are to maintain the ion lens as clean as possible.

References

Burkhardt, C., Kleine, T., Dauphas, N., Wieler, R., 2012. Origin of isotopic heterogeneity in the solar nebula by thermal processing and mixing of nebular dust. Earth and Planetary Science Letters 357, 298-307.

Carlson, R.W., 2014. Thermal ionization mass spectrometry. Treatise on Geochemistry, 337–354.

Caro, G., Bourdon, B., Birck, J.L., Moorbath, S., 2006. High-precision $^{142}Nd/^{144}Nd$ measurements in terrestrial rocks: Constraints on the early differentiation of the Earth's mantle. Geochimica et Cosmochimica Acta 70, 164-191.

Dodson, M.H., 1969. A theoretical study of the use of internal standards for precise isotopic analysis by the surface ionization technique part II: error relationships. Journal of Physics E: Scientific Instruments 2, 490–498.

Roth, A.S.G., Scherer, E.E., Maden, C., Mezger, K., Bourdon, B., 2014. Revisiting the ^{142}Nd deficits in the 1.48 Ga Khariar alkaline rocks, India. Chemical Geology 386, 238-248.

Sharma, M., Papanastassiou, D.A., Wasserburg, G.J., Dymek, R.F., 1996. The issue of the terrestrial record of ^{146}Sm. Geochimica et Cosmochimica Acta 60, 2037-2047.

Chapter 4:
Neodymium isotope heterogeneity of ordinary and carbonaceous chondrites and the origin of non-chondritic ^{142}Nd compositions in the Earth

based on Fukai, R. and Yokoyama, T. (2017) EPSL, 474, 206.

Abstract

We present high-precision Nd isotope compositions for ordinary and carbonaceous chondrites determined using thermal ionization mass spectrometry (TIMS) with the dynamic and multistatic methods. The ordinary chondrites had uniform and non-terrestrial μ^{142}Nd, μ^{148}Nd, and μ^{150}Nd values, with data that plot along the mixing line between *s*-process and terrestrial components in μ^{150}Nd versus μ^{148}Nd, μ^{142}Nd versus μ^{148}Nd, and μ^{142}Nd versus μ^{150}Nd diagrams. In contrast, the carbonaceous chondrites were characterized by larger anomalies in their μ^{142}Nd, μ^{148}Nd, and μ^{150}Nd values compared to ordinary chondrites. Importantly, the data for carbonaceous chondrites plot along the *s*-process and terrestrial mixing line in a μ^{150}Nd versus μ^{148}Nd diagram, whereas they have systematically lower μ^{142}Nd values than the *s*-process and terrestrial mixing line in μ^{142}Nd versus μ^{148}Nd and μ^{142}Nd versus μ^{150}Nd diagrams. This shift likely results from the incorporation of calcium- and aluminum-rich inclusions (CAIs), indicating that the Nd isotopic variability in the ordinary and CAI-subtracted carbonaceous chondrites was caused solely by the heterogeneous distribution of *s*-process nuclides. The isotopic variation most likely results from nebular thermal processing that caused selective destruction of *s*-process-depleted dust grains in the inner Solar System where the parent bodies of ordinary chondrites formed, whereas such grains were preserved in the region of carbonaceous chondrite parent body formation. The Nd isotope dichotomy between bulk aliquots of ordinary and carbonaceous chondrites can be related to the presence of Jupiter, which may have separated two isotopically distinct reservoirs that were present in the solar nebula. After

correcting for *s*-process anomalies and CAI contributions to the Nd isotopes observed in the chondrites, we obtained a μ^{142}Nd value (−2.4 ± 4.8 ppm) that was indistinguishable from the terrestrial value. Our results corroborate the interpretation that a missing reservoir (e.g., a hidden enriched mantle reservoir, erosional loss of crust) is not required to explain the observed differences in ^{142}Nd/^{144}Nd ratios between chondrites and terrestrial materials.

4.1 Introduction

Nucleosynthetic isotope anomalies in bulk chondrites and differentiated meteorites, which are characterized by isotopic deviations from terrestrial materials, have become a well-studied phenomenon for several refractory elements including Ti, Cr, Sr, Mo, and Ba (e.g., Dauphas et al., 2004; Trinquier et al., 2007, 2009; Burkhardt et al., 2011; Moynier et al., 2012; Yokoyama et al., 2015; Bermingham et al., 2016). These findings point to the existence of planetary-scale isotopic heterogeneities in refractory heavy elements as a result of the heterogeneous distribution of presolar grains in the solar nebula before the onset of planetesimal formation. In contrast, some elements exhibit uniform isotope compositions across different meteorite groups, including Te (Fehr et al., 2006; Fukami and Yokoyama, 2017), Hf (Sprung et al., 2010), and Os (Yokoyama et al., 2007, 2010). Such inconsistencies in isotope distributions are critical for understanding the physical and chemical processes that occurred in the solar nebula and/or in planetary bodies.

High-precision Nd isotope analyses of bulk chondrites have been the focus of recent interest in the cosmochemistry community (Boyet and Carlson, 2005; Andreasen and Sharma, 2006; Carlson et al., 2007; Gannoun et al., 2011; Burkhardt et al., 2016). A pioneering study on high-precision Nd isotope analyses with thermal ionization mass spectrometry (TIMS) found that bulk chondrites possess $^{142}Nd/^{144}Nd$ ratios that are approximately 20 ppm lower than those in terrestrial rocks (Boyet and Carlson, 2005). The cause of this anomaly was interpreted to be Sm–Nd fractionation via early differentiation of the terrestrial mantle.

Variations in $^{142}Nd/^{144}Nd$ ratios have been reported for three types of chondrites (enstatite, ordinary, and carbonaceous chondrites) in subsequent studies (Carlson et al., 2007; Gannoun et al., 2011). Because the $^{142}Nd/^{144}Nd$ ratios in chondrites roughly correlate with the ratios of non-radiogenic Nd isotopes (e.g., $^{148}Nd/^{144}Nd$, $^{150}Nd/^{144}Nd$), it has been suggested that the isotopic variation in Nd isotopes results from nucleosynthetic isotopic heterogeneities in the early Solar System. Importantly, these studies argued that the isotopic composition of terrestrial materials cannot be reproduced by the heterogeneous distribution of isotopically anomalous grains in the solar nebula. Dickin (2016) pointed out that the regression line obtained from plotted data for the three chondrites types does not pass the terrestrial composition on a $^{142}Nd/^{144}Nd$ versus $^{148}Nd/^{144}Nd$ diagram.

Recently, two studies reported intriguing results from high-precision Sm–Nd isotope measurements on bulk aliquots of chondrites, as well as calcium- and aluminum-rich inclusions (CAIs) and their mineral fractions. Burkhardt et al. (2016) found that non-radiogenic isotopes in chondrites and CAIs from the carbonaceous chondrite Allende (CV3) display nucleosynthetic anomalies. The authors argued that the Sm–Nd isotope anomalies in the chondrites could be explained by a deficit in *s*-process components relative to the Earth, although the anomalies in the bulk Allende material required an additional anomalous component. In contrast, Bouvier and Boyet (2016) found that the bulk CAIs and their mineral fractions from three carbonaceous chondrites had non-radiogenic Nd isotope compositions similar to that of a terrestrial standard, excluding CAIs from NWA 2364 (CV3). In addition, the authors argued that the CAIs

without nucleosynthetic isotope anomalies shared a ^{146}Sm–^{142}Nd isotopic evolution that is consistent with that of the Earth. In spite of the contrasting results obtained in the two studies, both studies reached the conclusion that the bulk silicate Earth has a chondritic Sm/Nd ratio as well as chondritic abundances of other refractory elements, negating the need for a hidden mantle reservoir model or collisional erosion crust scenario to explain the elevated $^{142}Nd/^{144}Nd$ ratio of the Earth's mantle relative to chondrites.

Bulk carbonaceous chondrites generally show the largest nucleosynthetic isotope anomalies for refractory heavy elements (e.g., Cr, Sr, Mo, Ru). In addition, the strength of the isotope anomalies for some elements (e.g., Cr, Sr) is variable across different groups of carbonaceous chondrites. Therefore, carbonaceous chondrites are well suited to preserving information about the distribution of isotopically anomalous carriers in the early Solar System. However, high-precision Nd isotope analyses of bulk carbonaceous chondrites, especially for presolar-grain-bearing unequilibrated chondrites, have been hindered due to analytical difficulties in achieving complete sample dissolution with acid digestion. The importance of complete sample digestion in nucleosynthetic isotope anomaly studies on unequilibrated chondrites has been demonstrated in several previous works (Sr: Yokoyama et al., 2015; Ba: Bermingham et al., 2016; Os: Yokoyama et al., 2007, 2010). In this study, we performed high-precision Nd isotope analyses on various types of ordinary and carbonaceous chondrites using TIMS with an improved dynamic multi-collection method (Chapters 2 and 3). Notably, samples containing acid-resistant presolar grains were processed by a new acid digestion technique that achieved complete dissolution of presolar grains (Yokoyama et al., 2015). With the new

high-precision Nd isotope data for ordinary and carbonaceous chondrites, we revisit the origin of nucleosynthetic Nd isotope variability in chondrites and terrestrial materials.

4.2 Experimental procedures

We investigated three terrestrial samples (JB-3, basalt; JA-2, andesite; JR-2, rhyolite), six carbonaceous chondrites (Tagish Lake, C2-ungrouped; Murchison, CM2; Dho 1432, CR2; Allende, CV3; NWA 2090, CO3; DaG 190, CO3), and eight ordinary chondrites (Kesen, H4; Forest City, H5; Saratov, L4; Etter, L5; Modoc (1905), L6; Hamlet, LL4; Tuxtuac, LL5; Saint-Séverin, LL6). The meteorite chips were cleaned with distilled acetone and H_2O for 30 min., and then powdered using either an agate mortar and pestle or a sample homogenizer (Multi-beads shocker®; Yasui Kikai, Japan), with which the rock chips were pulverized in polyethylene bottles at 2500 rpm for 900-s.

The concentrations of Nd and Sm in the meteorite samples were determined using the isotope dilution method with a quadrupole-type inductively coupled plasma-mass spectrometer (ICP-MS: X-Series 2; Thermo Fisher Scientific, USA) following the procedure described in Kagami and Yokoyama (2016). In brief, aliquots (~5%) of meteorite sample solutions prepared by acid digestion for Nd isotope analysis (see below) were transferred to Teflon vessels to which ^{145}Nd- and ^{149}Sm-enriched spikes were added. The vessels were tightly capped and heated at 100 °C overnight to ensure isotopic equilibrium. Then, the solutions were dried and dissolved in 3.0 M HNO_3 (0.5 mL). Subsequently, the sample solutions were passed through a 100–150-μm TRU resin (Eichrom Technologies, USA) to remove major elements. Finally, the ^{145}Nd/^{146}Nd and ^{147}Sm/^{149}Sm ratios of the sample solutions were determined simultaneously with ICP-MS.

Ordinary and carbonaceous chondrites with a petrologic grade of less than 4 are known to contain isotopically anomalous acid-resistant presolar grains such as SiC and graphite. These meteorite samples (~0.5 g) were placed in a polytetrafluoroethylene (PTFE) insert (50 mL vol.) in a high-pressure digestion system (DAB-2; Berghof, Germany), together with 6.8 mL 30 M HF (AAS grade with distillation; Kanto Chemical, Japan), 4.8 mL 16 M HNO_3 (EL grade with distillation; Mitsubishi Chemical, Japan), and 9.6 mL 96% H_2SO_4 (Ultrapur-grade; Kanto Chemical, Japan). The insert was then placed in a stainless steel jacket and heated at 250 °C for 48 h under high-pressure. The effectiveness of this approach in decomposing refractory presolar grains was confirmed by Yokoyama et al. (2015). After sample digestion, the PTFE insert was placed on a hotplate at 220 °C in order to completely evaporate the HF and HNO_3. The solution was transferred to a quartz glass beaker and dried at 310 °C in order to evaporate the remaining H_2SO_4. The residue in the PTFE insert was dissolved in 6.4 M HCl and transferred to a glass beaker, then dried at 150 °C. Finally, the dried sulfate-containing residue was dissolved in 20 mL of 1.0 M HCl for chemical separation (see below). Chondrite samples with a petrologic grade of 4 or greater were digested using the normal procedures described in Yokoyama et al. (2017). In brief, the powdered samples (up to 2 g) were placed in Teflon vessels with a 1:1:1 mixture of 30 M HF, 12 M $HClO_4$ (AA–100 grade; TAMA Chemical, Japan), and 16 M HNO_3 in proportions of 1 mL of each acid per 0.1 g of sample. The sample solutions were heated at 120 °C for 12 h, at 165 °C for 20 h, and at 195 °C until dry. To completely decompose insoluble fluorides, the same amount of 12 M $HClO_4$ was added to the dried

sample and heated at 165 °C for 20 h and at 195 °C until dry. The dried solutions were finally dissolved in 20 mL of 1.0 M HCl for chemical separation.

For Nd isotope analysis, we conducted a 5-step column separation procedure that was modified from Kagami and Yokoyama (2016). The sample solution was loaded onto a 1:1 mixture of two cation-exchange resins (AG50WX8 and AG50WX12; Bio-Rad, USA) in order to remove major elements (e.g., Mg, Al, Fe). Then, Sr was separated from the REEs using a 100–150-μm Sr resin (Eichrom Technologies) and retained for Sr isotope analysis. To remove the remaining major elements (e.g., Ca), the solution was again passed through the mixed cation-exchange resin. Subsequently, Ce was removed from the remaining REEs by passing the solution through a 50–100-μm LN resin (Eichrom Technologies), during which Ce^{3+} in the sample solution (10 M HNO_3) was oxidized to Ce^{4+} using $KBrO_3$ (Tazoe et al., 2007). Finally, Nd was separated from Sm using the LN resin in HCl media. The amount of Nd in the blank resulting from the entire chemical procedure was ~10 pg. Because we used 100–1000 ng Nd for each single isotopic measurement, the blank content did not affect the Nd isotopic compositions obtained for the meteorite and terrestrial samples in this study.

For terrestrial rocks, we conducted an analytical protocol that differed slightly from that used for the meteorite samples. Samples (~50 mg) were decomposed using the same procedure outlined for meteorite samples with a petrologic grade of 4 or greater, although HNO_3 was not used because these samples do not contain organic materials. The decomposed samples were dissolved in 1.0 M HCl, and Nd was separated via a 1-step cation-exchange and 2-step separations with the LN resin. We regard the subtle

difference between the chemical procedures for meteorite and terrestrial samples as unlikely to bias the results of Nd isotope measurements based on the fact that the recovery yield of Nd was ~100% during the first cation-exchange and the Sr resin separation procedures, both of which were omitted in the analyses of terrestrial samples. This result should preclude any unexpected mass-independent Nd isotope fractionation.

All isotope measurements were performed using TIMS instrument (Triton *Plus*; Thermo Fisher Scientific) installed at the Tokyo Institute of Technology. The instrument is equipped with nine Faraday cups and 10^{11} Ω resistors. Neodymium was ionized with a double-filament assembly using a zone-refined Re filament (thickness: 0.0305 mm, width: 0.750 mm; H. Cross, USA) that was outgassed under vacuum conditions prior to use. The Nd sample (100–1000 ng) was dissolved in 1 μL of 6.4 M HCl, then loaded onto the evaporation filament and dried at 0.8 A. Subsequently, the sample was covered with 1 μL of 0.04% H_3PO_4 and dried at 1.0 A. In each measurement, the ionization filament temperature was first increased to 4.0 A at a rate of 200 mA/m. The current in the sample filament was increased to 1.0 A at a rate of 100 mA/m, after which it continuously increased at a lower rate (10–50 mA/m) until the $^{142}Nd^{+}$ intensity reached ~10 V.

Neodymium isotopes were collected with a two-jump cup configuration within a single measurement run (Table 4.1), in which $^{142}Nd/^{144}Nd$, $^{148}Nd/^{144}Nd$, and $^{150}Nd/^{144}Nd$ ratios were obtained using the dynamic multi-collection method described in Chapter 2. Individual isotopic measurements consisted of 360 ratios of 16.67-s integrations. The mass-dependent isotopic fractionation during measurements was corrected by the

exponential law and normalized using the relation $^{146}Nd/^{144}Nd = 0.7219$.

Table 4.1 *Analytical conditions for Nd isotope measurements with TIMS.*

	L4	L3	L2	L1	C	H1	H2	H3	H4	Integration time	Idle time
Jump 1	^{140}Ce	^{142}Nd	^{143}Nd	^{144}Nd	^{145}Nd	^{146}Nd	^{147}Sm	^{148}Nd	^{150}Nd	16.777 s	4.000 s
Jump 2		^{140}Ce		^{142}Nd	^{143}Nd	^{144}Nd	^{145}Nd	^{146}Nd	^{148}Nd	16.777 s	4.000 s

Neodymium isotope collection consisted of two jumps in one cycle, 20 cycles in one block, and 18 blocks in a single measurement. An amplifier rotation system was applied to minimize the error due to the amplifier gain calibration in the case of static measurements. The total analytical time for a single measurement was ~4.5 h including a baseline measurement (30 s) at the beginning of each block, beam focusing every 3 blocks, and peak centering every 5 blocks. Mass interferences from Ce and Sm are monitored at ^{140}Ce (Jumps 1 and 2) and ^{147}Sm (Jump 1) by assuming $^{142}Ce/^{140}Ce = 0.12565$, $^{144}Sm/^{147}Sm = 0.20498$, $^{148}Sm/^{147}Sm = 0.74970$, and $^{150}Sm/^{147}Sm = 0.49219$.

In addition, this method enables the determination of $^{143}Nd/^{144}Nd$ and $^{145}Nd/^{144}Nd$ ratios by the two-jump multistatic method protocol. To eliminate the effect of temporal fluctuations in the Nd isotope ratios obtained by the multistatic and possibly the dynamic methods, which is primarily due to deterioration of the Faraday cups, the absolute Nd isotope ratios for an unknown sample were obtained by normalizing the observed Nd isotope ratios to the mean values of the terrestrial standard JNdi-1 obtained in each analytical campaign (<2 months). The analytical reproducibilities of the Nd isotope ratios obtained by the dynamic method during each analytical campaign were ±5.1, ±5.9, and ±11 ppm (2 SDs) on average for $^{142}Nd/^{144}Nd$, $^{148}Nd/^{144}Nd$, and

$^{150}Nd/^{144}Nd$ ratios, respectively. Notably, the reproducibilities for $^{148}Nd/^{144}Nd$ and $^{150}Nd/^{144}Nd$ ratios obtained in this study were about three times better than those obtained by the static method in previous studies (Andreasen and Sharma, 2006; Boyet and Carlson, 2005; Carlson et al., 2007; Gannoun et al., 2011). The Nd isotope ratio reproducibilities obtained by the multistatic method were 5.1–13 ppm for $^{143}Nd/^{144}Nd$ ratio and 8.9–27 ppm for $^{145}Nd/^{144}Nd$ ratio (2 SDs), which were more precise than those obtained by the static method ($^{143}Nd/^{144}Nd$: 5.3–22 ppm, $^{145}Nd/^{144}Nd$: 7.6–47 ppm).

4.3 Results

Throughout this chapter, the Nd isotope ratios (excluding $^{143}Nd/^{144}Nd$) for meteorite and terrestrial rock samples are reported in μ notation, which represents parts per 10^6 deviations from the mean values of repeated analyses for JNdi-1 ($\mu^{i}Nd = (R_{sample}/R_{terrestrial}-1) \times 10^6$, $R = {}^{i}Nd/^{144}Nd$). Tables 4.2 and 4.3 summarize the Nd isotope ratios and $^{147}Sm/^{144}Nd$ ratios for terrestrial and chondrite samples obtained in this study. For samples measured three times or more, the reported analytical errors are either 2 SDs of the multiple sample measurements or the average analytical uncertainties of multiple campaigns for JNdi-1 (2 SDs), whichever is larger. For samples measured twice, the analytical errors are represented as the average analytical uncertainties of multiple campaigns for JNdi-1 (2 SDs). For samples measured once, the analytical errors are either the internal error of a single measurement or the analytical uncertainty for JNdi-1 (2 SD) measured in the same analytical campaign, whichever is larger. The errors on the $^{147}Sm/^{144}Nd$ ratios are the internal error of a single measurement.

4.3.1 Terrestrial samples

Neodymium isotope ratios for terrestrial samples obtained using the dynamic method ($\mu^{142}Nd$, $\mu^{148}Nd$, and $\mu^{150}Nd$ values) are shown in Fig. 4.1. The reproducibilities of the $\mu^{142}Nd$, $\mu^{148}Nd$, and $\mu^{150}Nd$ values for JNdi-1 calculated by averaging the values from multiple analytical campaigns are also shown as gray bars. Because these samples were measured in different analytical campaigns throughout the entire analytical period

of this study, the consistency of the μ^{142}Nd, μ^{148}Nd, and μ^{150}Nd values between the terrestrial rock samples and JNdi-1 verifies the accuracy of our measurements.

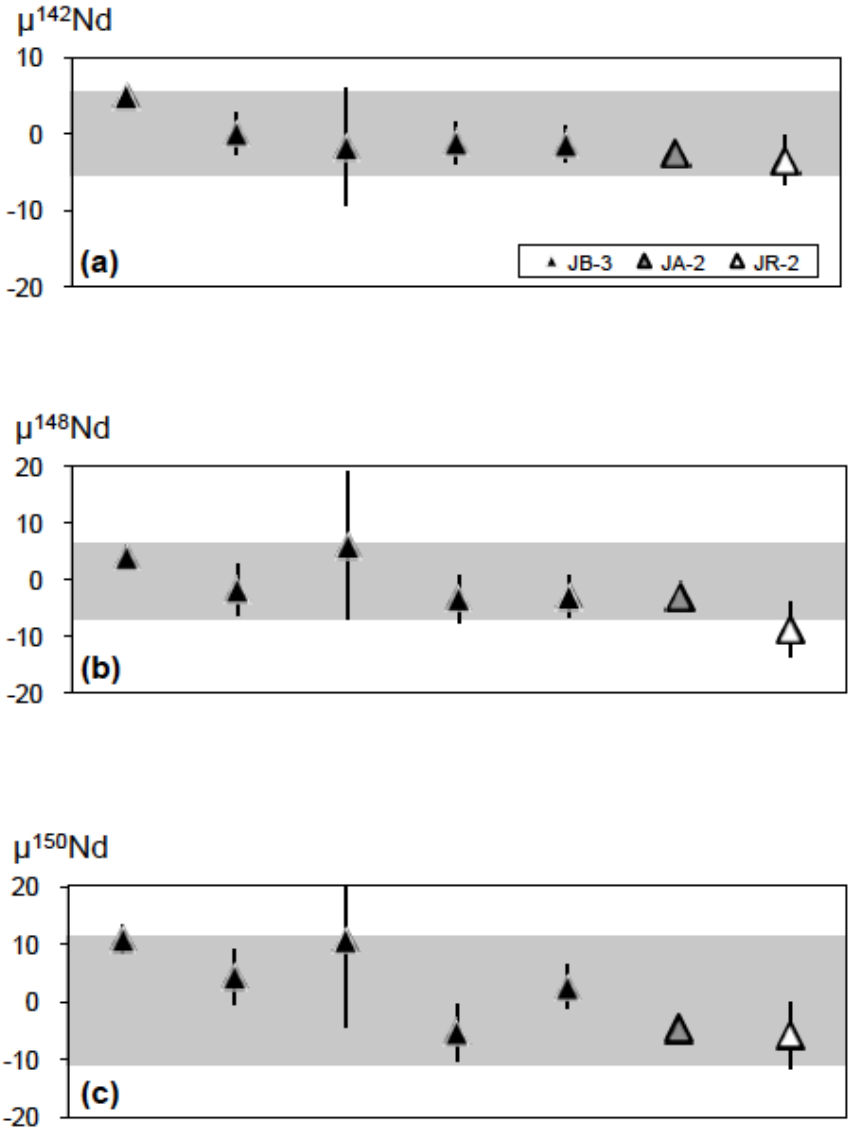

Fig. 4.1 *(a) μ^{142}Nd, (b) μ^{148}Nd, and (c) μ^{150}Nd values of terrestrial rocks (black triangles, JB-3; gray triangle, JA-2; white triangle, JR-2). Gray bars represent the mean reproducibilities (2 SDs) for repeated measurements of JNdi-1 in multiple analytical campaigns. Error bars are the internal uncertainties of each single measurement (2 SEs).*

4.3.2 Ordinary and carbonaceous chondrites

All ordinary chondrites had negative μ^{142}Nd values ranging from −19 to −7.5 ppm (Table 4.2). Ordinary chondrites had positive μ^{148}Nd (+6.4 to +15 ppm) and μ^{150}Nd values (+6.0 to +35 ppm) except for Adrian (H4). The μ^{145}Nd values of the ordinary chondrites were difficult to resolve from the isotopic composition of the terrestrial standard because of the relatively large analytical uncertainty.

In contrast to the ordinary chondrites, carbonaceous chondrites displayed variable μ^{142}Nd values ranging from −34 to −5.6 ppm (Table 4.2). Most of the carbonaceous chondrites had positive μ^{148}Nd and μ^{150}Nd values that exceeded the range of analytical reproducibilities for the terrestrial standard. In contrast, μ^{148}Nd and μ^{150}Nd isotope anomalies were not obvious in NWA 2090 (CO3) and Tagish Lake (C2-ungrouped).

Table 4.2 *Neodymium isotope compositions for the terrestrial materials and ordinary and carbonaceous chondrites measured in this study.*

Sample	Type	N	$\mu^{142}Nd$	$\mu^{142}Nd_{143Nd\_corr.}$	$\mu^{145}Nd$	$\mu^{148}Nd$	$\mu^{150}Nd$	$^{143}Nd/^{144}Nd$
Terrestrial samples								
JB-3	Basalt	5	–0.2 ± 5.5		2.3 ± 16	0.5 ± 8.6	4.6 ± 13	0.513060 (10)
JA-2	Andesite	1	–2.5 ± 4.0		–19 ± 27	–2.9 ± 4.6	–4.7 ± 7.4	0.512543 (5)
JR-2	Rhyolite	1	–3.5 ± 4.0		7.5 ± 27	–8.7 ± 4.8	–5.8 ± 7.4	0.512920 (5)
Ave.		**3**	**–2.0 ± 4.0**		**–3.1 ± 28**	**–3.7 ± 9.3**	**–2.0 ± 11**	
Ordinary chondrites								
Adrian	H4	2	–8.9 ± 5.1		–7.5 ± 16	–1.0 ± 5.9	–1.7 ± 11	0.512284 (5)
Kesen	H4	1	–12 ± 4.9	–12 ± 4.9	–4.4 ± 14	15 ± 4.9	27 ± 12	0.512632 (7)
Forest City	H5	1	–12 ± 7.4	–12 ± 7.4	17 ± 27	11 ± 7.6	17 ± 19	0.512633 (3)
Saratov	L4	2	–14 ± 5.1	–13 ± 5.1	6.8 ± 16	13 ± 5.9	20 ± 11	0.512616 (5)
Etter	L5	1	–16 ± 4.0	–15 ± 4.0	–12 ± 27	8.9 ± 4.6	19 ± 7.4	0.512599 (5)
Modoc (1905)	L6	2	–19 ± 5.1	–13 ± 5.1	–6.1 ± 16	8.1 ± 5.9	6.0 ± 11	0.512510 (5)
Hamlet	LL4	1	–7.5 ± 4.9	–7.2 ± 4.9	2.4 ± 15	10 ± 5.1	35 ± 12	0.512626 (7)
Tuxtuac	LL5	2	–11 ± 5.1	–12 ± 5.1	–7.3 ± 16	6.4 ± 5.9	13 ± 11	0.512643 (5)
Saint-Séverin	LL6	1	–12 ± 7.8	–8.9 ± 7.8	–5.7 ± 14	10 ± 12	23 ± 12	0.512571 (7)
Ave.		**8**	**–13 ± 6.9**	**–12 ± 4.8**	**–1.2 ± 19**	**10 ± 5.8**	**20 ± 17**	
Carbonaceous chondrites								
Tagish Lake	C2-ungrouped	2	–18 ± 5.1		–4.9 ± 16	3.2 ± 5.9	8.7 ± 11	0.512599 (5)
NWA 2090	CO3	2	–5.6 ± 5.1		–6.7 ± 48	0.8 ± 5.9	4.3 ± 11	0.512315 (8)
Dho 1432	CR2	1	–28 ± 3.8	–30 ± 3.8	16 ± 15	18 ± 5.4	26 ± 9.5	0.512677 (5)
Murchison	CM2	4	–31 ± 7.4	–31 ± 7.4	2.1 ± 16	23 ± 13	24 ± 24	0.512613 (5)
Allende	CV3	4	–32 ± 7.5	–31 ± 7.5	–1.1 ± 16	19 ± 16	27 ± 26	0.512608 (19)
DaG 190	CO3	1	–34 ± 4.0	–34 ± 4.0	19 ± 27	22 ± 4.6	27 ± 7.4	0.512641 (5)
Ave.		**4**	**–31 ± 5.3**	**–32 ± 4.0**	**9.0 ± 20**	**20 ± 4.6**	**26 ± 7.4**	

Analytical errors for samples with N ≥ 3 are either 2 SDs of multiple measurements or average analytical uncertainties from multiple campaigns for JNdi-1 (2 SDs), whichever is larger. Analytical errors with N = 2 are represented as average analytical uncertainties of the dynamic method from multiple campaigns for JNdi-1 (2 SDs).

Analytical errors for samples with N = 1 are either the internal uncertainties of a single measurement or the analytical uncertainty of JNdi-1 (2 SD) measured in the same analytical campaign, whichever is larger. The numbers in parentheses for $^{143}Nd/^{144}Nd$ are individual analytical errors in the final digit. $\mu^{142}Nd_{143Nd\_corr.}$ denotes $\mu^{142}Nd$ corrected for radiogenic ^{142}Nd variations to a common chondritic value ($^{143}Nd/^{144}Nd$ = 0.512630; Bouvier et al. 2008).

Table 4.3 *$^{147}Sm/^{144}Nd$ ratios for ordinary and carbonaceous chondrites measured in this study.*

Sample	Type	Fall or Find	$^{147}Sm/^{144}Nd$
Ordinary chondrites			
Adrian	H4	Find	0.137 ± 0.002
Kesen	H4	Fall	
Forest City	H5	Fall	0.196 ± 0.003
Saratov	L4	Fall	0.196 ± 0.002
Etter	L5	Find	0.195 ± 0.002
Modoc (1905)	L6	Fall	0.195 ± 0.002
Hamlet	LL4	Fall	
Tuxtuac	LL5	Fall	0.192 ± 0.002
Saint-Séverin	LL6	Fall	0.191 ± 0.002
Carbonaceous chondrites			
Tagish Lake	C2-ungrouped	Fall	0.148 ± 0.001
NWA 2090	CO3	Find	0.174 ± 0.002
Dho 1432	CR2	Find	0.195 ± 0.003
Murchison	CM2	Fall	0.197 ± 0.002
Allende	CV3	Fall	0.195 ± 0.002
DaG 190	CO3	Find	0.197 ± 0.002

Analytical errors for samples with N = 1 are either the internal error of a single measurement or the analytical uncertainty of JNdi-1 (2 SD) measured in the same analytical campaign, whichever is larger. Errors for the $^{147}Sm/^{144}Nd$ ratios are the internal error of a single measurement.

4.4 Discussion

4.4.1 Ancient and recent redistributions of Nd and Sm in chondrites

Fig. 4.2 shows $^{143}Nd/^{144}Nd$ versus $^{147}Sm/^{144}Nd$ and $\mu^{142}Nd$ versus $^{147}Sm/^{144}Nd$ diagrams for ordinary and carbonaceous chondrites. In $^{143}Nd/^{144}Nd$ versus $^{147}Sm/^{144}Nd$ space, the data for Adrian (H4) and NWA 2090 (CO3) clearly deviate from the 4.567 Ga isochron. While the $^{143}Nd/^{144}Nd$ ratios for most of the chondrites analyzed were consistent with that reported for unequilibrated chondrites by Bouvier et al. (2008) (0.51263 ± 0.00001, 2SE), Adrian and NWA 2090 have markedly lower $^{143}Nd/^{144}Nd$ ratios (0.51228 and 0.51232, respectively) than those of the other chondrites. Importantly, the Adrian $\mu^{148}Nd$ and $\mu^{150}Nd$ values were distinct from those of the other ordinary chondrites, whereas the $\mu^{148}Nd$ and $\mu^{150}Nd$ values for Kesen (H4), which belongs to the same subgroup of ordinary chondrites, were consistent with those of the other samples. As is the case for Adrian, NWA 2090 displayed $\mu^{148}Nd$ and $\mu^{150}Nd$ values distinct from those of another CO3 chondrite, DaG 190. These variations are not caused by incomplete sample digestion because the carbonaceous chondrites were decomposed using a high-pressure digestion system with HF + HNO_3 + H_2SO_4. The non-isochronous behavior of Adrian and NWA 2090 could result from thermal metamorphism of the parent body, as well as recent secondary processes including shock metamorphism and/or terrestrial weathering. Gannoun et al. (2011) argued that such processes would alter the $\mu^{142}Nd$ values in enstatite chondrites to produce $^{143}Nd/^{144}Nd$ ratios outside the range defined for chondrites. For this reason, Adrian and NWA 2090 are excluded from the following discussion.

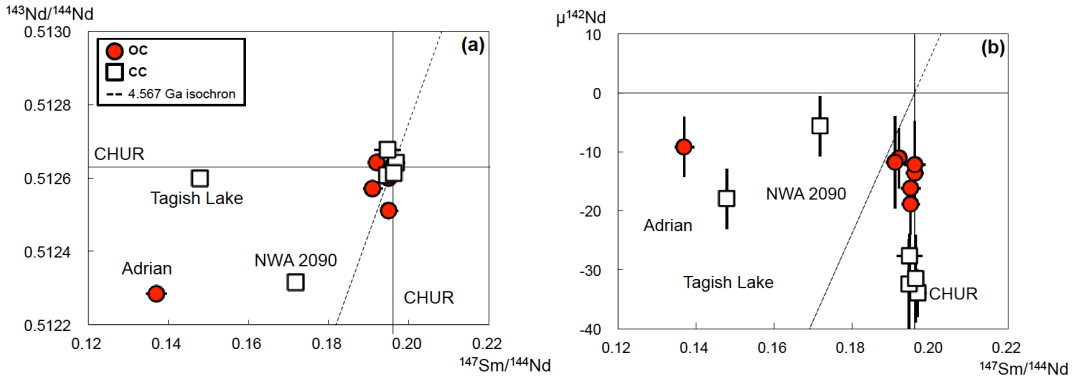

Fig. 4.2 *$^{143}Nd/^{144}Nd$ versus $^{147}Sm/^{144}Nd$ and (b) $\mu^{142}Nd$ versus $^{147}Sm/^{144}Nd$ diagrams for ordinary and carbonaceous chondrites. See the text (Section 4.3) and Tables 4.2 and 4.3 for error bars. $^{143}Nd/^{144}Nd$ and $^{147}Sm/^{144}Nd$ ratios of CHUR (0.512630 and 0.1960, respectively) were obtained from Bouvier et al. (2008). The dashed line indicates the 4.567 Ga isochron for ^{147}Sm–^{143}Nd ($T_{1/2}$ = 1.06 × 10^{11} yr) and ^{146}Sm–^{142}Nd ($T_{1/2}$ = 1.03 × 10^{8} yr) passing through CHUR.*

On the other hand, Tagish Lake (C2-ungrouped) had a low $^{147}Sm/^{144}Nd$ ratio but had a chondritic $^{143}Nd/^{144}Nd$ ratio. Friedrich et al. (2002) demonstrated that later-collected samples of Tagish Lake displayed trace element patterns affected by weathering compared to the pristine batch of meteorite samples collected immediately after the fall. For the offset in the Tagish Lake isotope values to be caused by weathering would require a strong change in the Sm/Nd ratio, such that all other Nd isotopes in the sample should have been affected by this contamination as well. Indeed, relative to the other carbonaceous chondrites, Tagish Lake displays $\mu^{142}Nd$, $\mu^{148}Nd$, and $\mu^{150}Nd$ values that are offset toward the terrestrial composition, supporting the claim of significant terrestrial contamination. Thus, the anomalies in Tagish Lake are only minimum estimates, and it must be excluded from the following discussion as well.

4.4.2 Non-radiogenic Nd isotope anomalies in chondrites

As shown in Fig. 4.3, μ^{148}Nd and μ^{150}Nd values for the ordinary and carbonaceous chondrites are correlated and can largely be resolved from the terrestrial standard. For ordinary chondrites (Fig. 4.3a), the reproducibilities of the μ^{148}Nd and μ^{150}Nd values (±6.6 and ±18 ppm, respectively; 2 SDs) are comparable to those of JNdi-1 (±5.9 and ±11 ppm, respectively; 2 SDs). This suggests that ordinary chondrites possess uniform, non-terrestrial μ^{148}Nd and μ^{150}Nd values irrespective of their chemical classification (H, L, and LL) and petrologic grade (4–6). In the case of carbonaceous chondrites, the mean μ^{148}Nd and μ^{150}Nd values from multiple measurements of Allende and Murchison are indistinguishable from those of Dho 1432 and DaG 190. This result suggests that these carbonaceous chondrites possess generally uniform isotopic compositions with μ^{148}Nd and μ^{150}Nd values greater than those of ordinary chondrites. It should be noted that CV, CO, CM, and CR chondrites possess non-uniform compositions in terms of the modal abundances of CAIs (Hezel et al., 2008) and possibly presolar grains, which are supposed to be the carriers of anomalous Nd isotopes.

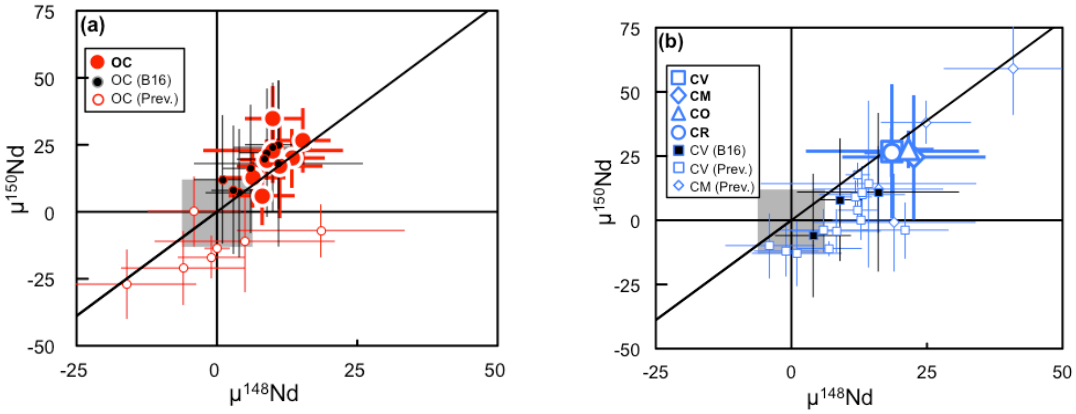

Fig. 4.3 *Diagrams of μ^{150}Nd versus μ^{148}Nd with data plotted for (a) ordinary and (b) carbonaceous chondrites measured in this study (large symbols). See the text (section 4.3) and Table 4.2 for error bars. Small open symbols represent previously reported data from Boyet and Carlson (2005), Andreasen and Sharma (2006), Carlson et al. (2007), Gannoun et al. (2011), and Saji et al. (2016). Small filled symbols represent the data of Burkhardt et al. (2016). Gray zones represent uncertainties on the terrestrial standard (2 SDs). Bold lines are mixing lines between theoretical s-process (Bisterzo et al., 2011) and terrestrial components.*

Fig. 4.3 contains plots of the μ^{148}Nd and μ^{150}Nd values for ordinary and carbonaceous chondrites obtained in previous studies (small symbols: Boyet and Carlson, 2005; Andreasen and Sharma, 2006; Carlson et al., 2007; Gannoun et al., 2011; Burkhardt et al., 2016; Saji et al., 2016). Most of the previous μ^{148}Nd and μ^{150}Nd values for ordinary chondrites and Allende (CV3) are systematically lower than those obtained in this study. This inconsistency cannot be attributed to the problem of incomplete sample digestion because the petrologic grade of these samples is equal to or greater than 3.6, so that the abundance of acid-resistant presolar grains (e.g., SiC, graphite) is either negligibly small or nil. In addition, most presolar SiC grains in

chondrites (mainstream grains) are considered to be enriched in *s*-process isotopes with extremely large negative μ^{148}Nd and μ^{150}Nd values (Hoppe and Ott, 1997), in which case incomplete digestion would result in a shift toward more positive μ^{148}Nd and μ^{150}Nd values. Furthermore, the previously reported μ^{148}Nd and μ^{150}Nd values for CM2 chondrites generally match our data, however, their reproducibilities are 1.7–2.1 times greater than those of this study. Therefore, we infer that the inconsistency between the previous μ^{148}Nd and μ^{150}Nd values and our data is primarily caused by analytical problems associated with relatively large uncertainties on the Nd isotope ratios obtained in previous studies. This interpretation is supported by recent high-precision Nd isotope analyses by Burkhardt et al. (2016), who used relatively large amounts of meteorite samples (~2 g) in each measurement. Their mean μ^{148}Nd and μ^{150}Nd values for ordinary chondrites (Fig. 4.3a; small filled symbols) are consistent with those of this study.

To evaluate the origin of non-terrestrial μ^{148}Nd and μ^{150}Nd values in chondrites, we performed mixing calculations between a terrestrial component and a theoretical *s*-process end-member component. The mixing lines presented in Fig. 4.3 were calculated by applying the equation from Dauphas et al. (2004) to Nd isotopes:

$$\mu\ ^{i}\mathrm{Nd} = \frac{\rho\ ^{i}\mathrm{Nd} - \rho^{146}\mathrm{Nd} \times \gamma\ ^{i}\mathrm{Nd}}{\rho^{142}\mathrm{Nd} - \rho^{146}\mathrm{Nd} \times \gamma^{142}\mathrm{Nd}} \times \mu^{142}\mathrm{Nd} \qquad (4.1)$$

$$\rho\ ^{i}\mathrm{Nd} = \left(\frac{^{i}\mathrm{Nd}}{^{144}\mathrm{Nd}}\right)_{s} \Big/ \left(\frac{^{i}\mathrm{Nd}}{^{144}\mathrm{Nd}}\right)_{Earth} - 1 \qquad (4.2)$$

$$\gamma\ ^{i}\mathrm{Nd} = (i - 144)/(146 - 144) \qquad (4.3).$$

The slopes of the mixing lines, calculated using multiple *s*-process components determined from different theoretical models (Arlandini et al., 1999; Bisterzo et al., 2011, 2014, 2015), are nearly indistinguishable from one another. Therefore, the *s*-process component of Bisterzo et al. (2011) was used to calculate the representative mixing lines shown in Fig. 4.3 (and in the following related figures). The data for ordinary and carbonaceous chondrites obtained in this study generally plot along the calculated mixing line in Fig. 4.3. This implies that the non-terrestrial μ^{148}Nd and μ^{150}Nd values for ordinary and carbonaceous chondrites resulted from a heterogeneous distribution of *s*-process nuclides in the early Solar System.

4.4.3 μ^{142}Nd anomalies in chondrites

Because ^{142}Nd is a decay product of the extinct nuclide ^{146}Sm ($T_{1/2}$ = 103 Myr), the μ^{142}Nd anomalies observed in chondrites relative to the accessible terrestrial mantle may not only reflect planetary-scale nucleosynthetic heterogeneities but also the effect of early Sm–Nd fractionation. Fig. 4.4 display plots of μ^{142}Nd versus μ^{148}Nd and μ^{142}Nd versus μ^{150}Nd values, respectively, for ordinary and carbonaceous chondrites. As shown in Figs. 4.4a and 4.4c, ordinary chondrites have uniform μ^{142}Nd values that can be resolved from the terrestrial standard. Notably, our data for ordinary chondrites plot along the mixing line between the *s*-process and terrestrial components, suggesting that the non-terrestrial μ^{142}Nd values in the ordinary chondrites, as is the case for the μ^{148}Nd and μ^{150}Nd values, was caused by the heterogeneous distribution of *s*-process nuclides

in the Solar System. Previous studies, including Burkhardt et al. (2016), reached the same conclusion, although the data from the previous studies exhibit a small shift away from the *s*-process–terrestrial mixing line on the $\mu^{142}Nd$–$\mu^{148}Nd$ diagram (Fig. 4.4a). The cause of elevated $\mu^{142}Nd$ values from previous studies is currently unclear; however, analytical difficulties or sampling bias may have been responsible for the small shifts observed.

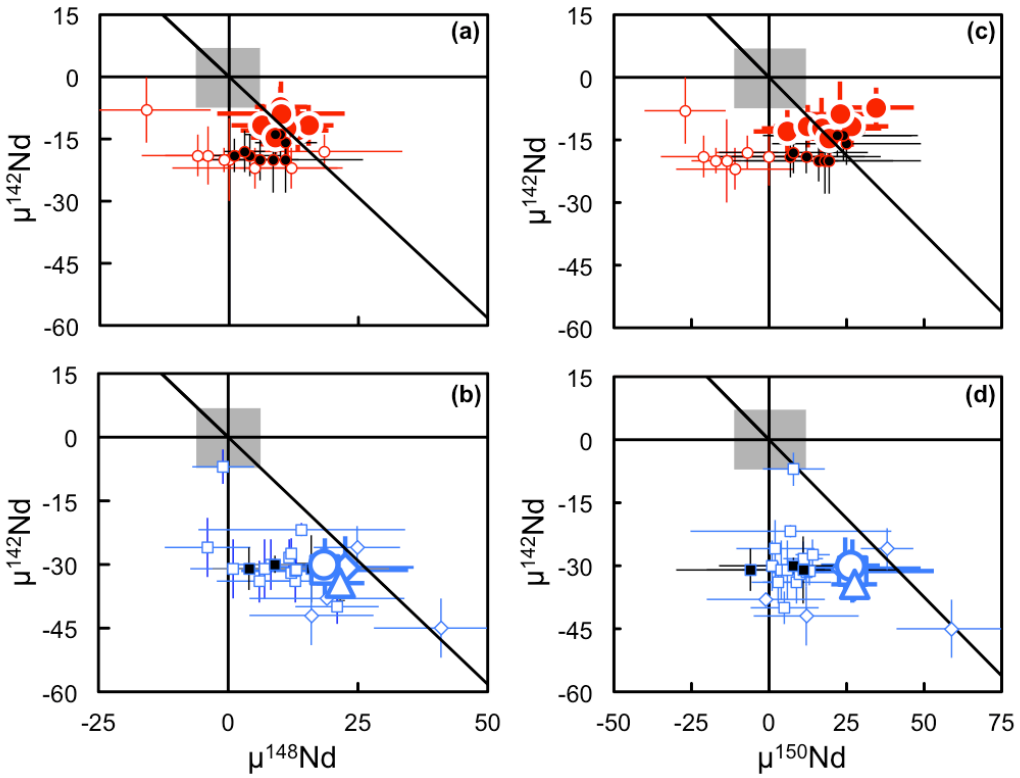

Fig. 4.4 *Diagrams of $\mu^{142}Nd$ versus $\mu^{148}Nd$ with data plotted for (a) ordinary and (b) carbonaceous chondrites and $\mu^{142}Nd$ versus $\mu^{150}Nd$ with data plotted for (c) ordinary and (d) carbonaceous chondrites. Large, small open, and small filled symbols, gray zones, error bars, and bold lines are as in Fig. 4.3. $\mu^{142}Nd$ values for ordinary and carbonaceous chondrites are corrected for radiogenic ^{142}Nd variations to a common chondritic value of $^{143}Nd/^{144}Nd = 0.512630$ (Bouvier et al., 2008).*

In contrast, the data for the carbonaceous chondrites deviate from the mixing line between the *s*-process and terrestrial components toward lower μ^{142}Nd values (Figs. 4.4b and 4.4d). Because the μ^{148}Nd and μ^{150}Nd values for carbonaceous chondrites lie along the *s*-process–terrestrial mixing line (Fig. 4.3b), the offset observed in Figs. 4.4b and 4.4d requires an additional source of the variation in ^{142}Nd/^{144}Nd ratios in carbonaceous chondrites other than the heterogeneous distribution of *s*-process nuclides. The effect of cosmic-ray exposure is unlikely to generate the observed μ^{142}Nd variation. Chondrites generally possess younger cosmic exposure ages (e.g., Allende: ~5 Ma; Eugster et al., 2007) compared to differentiated meteorites, although estimates for the other chondrites measured in this study have not been reported. The extent of the variations in μ^{142}Nd induced by cosmic-ray exposure is expected to be smaller than 1 ppm, as suggested by the magnitude of negative and positive shifts in the ^{149}Sm/^{152}Sm and ^{150}Sm/^{152}Sm ratios of chondrites (Carlson et al., 2007; Gannoun et al., 2011; Burkhardt et al., 2016).

The observed negative shift in μ^{142}Nd values for carbonaceous chondrites could be attributed to the incorporation of CAIs. Burkhardt et al. (2016) asserted that a CAI from Allende had an *s*-process-enriched μ^{148}Nd value (–28 ± 15 ppm) with a decay-corrected μ^{142}Nd value of −15 ± 7.8 ppm, which is consistent with the data for other canonical CAIs from Allende measured by Brennecka et al. (2013). As shown in Fig. 4.5, the data points for these Allende CAIs plot below the mixing line between *s*-process and terrestrial components. Burkhardt et al. (2016) argued that subtracting this

component from the bulk aliquot of Allende gave the composition of a CAI-subtracted carbonaceous chondrite source reservoir, whose μ^{142}Nd and μ^{148}Nd values plotted close to the *s*-process–terrestrial mixing line. To assess this model, we determined the isotopic compositions of CAI-subtracted carbonaceous chondrites using a mass-balance calculation, assuming that the Nd isotopic compositions (Brennecka et al., 2013) and Nd concentrations (9.1 ppm; Marks et al., 2014) of the CAIs were uniform across all types of carbonaceous chondrites. In contrast, the CAI abundances were non-uniform across individual types of carbonaceous chondrites (CV: 2.98 %, CM: 1.21 %, CO: 0.99 %, CR: 0.12 %; Hezel et al., 2008). The Nd concentrations in individual bulk chondrites types were determined by ICP-MS measurements using the isotope dilution method (Table 4.4).

Table 4.4 *Parameters and the results of mass-balance calculations for carbonaceous chondrites.*

	Nd conc. (ppm)	CAI abun. (vol. %) (1)	μ^{142}Nd	2 SE	μ^{148}Nd	2 SE	μ^{150}Nd	2 SE
CAI (2)	9.1 (3)		–10	4.5	–29	5.4	–64	11
Dho $1432_{calc.}$	0.61	0.1	–30	3.9	19	5.5	29	10
$Murchison_{calc.}$	0.64	1.2	–35	5.0	34	8.0	43	15
DaG $190_{calc.}$	0.70	1.0	–38	5.2	30	7.3	42	13
$Allende_{calc.}$	0.89	3.0	–41	6.0	37	13	65	19

References. *(1) Hezel et al., (2008); (2) Brennecka et al., (2013); (3) Marks et al., (2014);*

Uncertainties for Nd isotopic compositions (2 SEs) were derived by propagating the analytical errors of Nd isotopic measurements for CAIs.

Fig. 4.5 shows μ^{142}Nd, μ^{148}Nd, and μ^{150}Nd values for the CAI-subtracted carbonaceous chondrites, all of which generally plot along the *s*-process mixing line. This result suggests that the offset from this line in the carbonaceous chondrite data in Figs. 4.4b and 4.4d is due to the incorporation of CAIs, and that the Nd isotopic variability in ordinary chondrites and the CAI-subtracted carbonaceous chondrites was therefore caused solely by the heterogeneous distribution of *s*-process nuclides (Burkhardt et al., 2016). Most importantly, the determined isotopic compositions of CAI-subtracted carbonaceous chondrites are variable and can be distinguished from one another in Fig. 4.5, suggesting that the CAI-subtracted carbonaceous chondrite reservoir possessed heterogeneous Nd isotopic compositions. This observation is consistent with the results of the Cr isotope analysis in carbonaceous chondrites that indicated large

within-group variations in ε^{54}Cr (Trinquier et al. 2007). Note that the Cr abundances in CAIs are not as high as Nd, so that subtracting the CAI components from the bulk carbonaceous chondrites only marginally modifies their Cr isotopic compositions (Burkhardt et al., 2016).

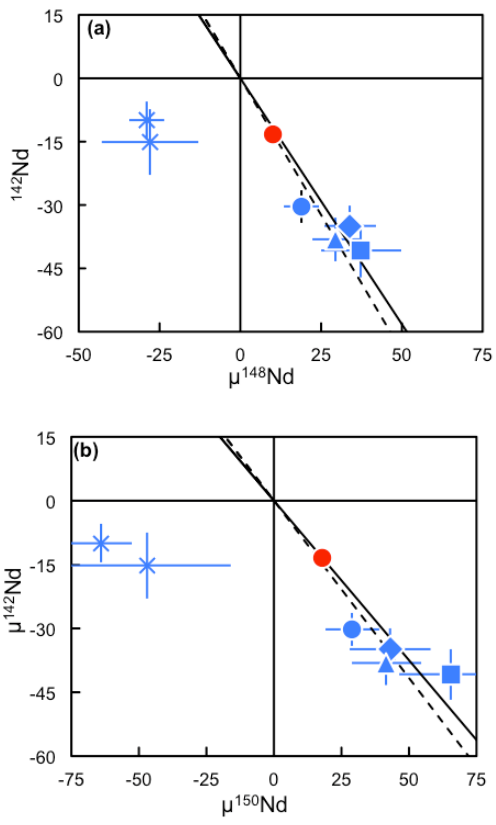

Fig. 4.5 *Diagrams of (a) μ^{142}Nd versus μ^{148}Nd and (b) μ^{142}Nd versus μ^{150}Nd values for ordinary and carbonaceous chondrites. Large symbols represent corrected data for the CAI contribution to ordinary chondrites (circles) and individual carbonaceous chondrites (symbol shapes are the same as in Figs. 4.3–4.4). Error bars for ordinary and carbonaceous chondrites represent uncertainties (2 SEs) derived by propagating the analytical errors from Nd isotopic measurements on CAIs. Crosses are data for CAIs with analytical errors (2 SDs) obtained in previous studies (Brennecka et al., 2013; Burkhardt et al., 2016). μ^{142}Nd values for ordinary and carbonaceous chondrites are corrected for radiogenic ^{142}Nd variations to a common chondritic value of ^{143}Nd/^{144}Nd = 0.512630 (Bouvier et al., 2008).*

4.4.4 Origin of planetary-scale Nd isotope variability

Several models are capable of explaining the observed planetary-scale isotope variability in Nd between the Earth, ordinary, and CAI-subtracted carbonaceous chondrites. One such model involves late injection of materials from a nearby

core-collapse supernova (ccSN) into the solar nebula (e.g., Dauphas et al., 2010). As shown in Fig. 4.5, a depletion in *s*-process Nd isotopes in CAI-subtracted carbonaceous chondrites relative to the Earth and ordinary chondrites is nearly indistinguishable from an excess of *r*-process Nd isotopes in the μ^{142}Nd versus μ^{148}Nd and μ^{142}Nd versus μ^{150}Nd diagrams. Because *r*-process nuclides of some trans-iron elements (e.g., Sr, Mo) are synthesized in the extremely neutron-rich environment of a ccSN, the observation that CAI-subtracted carbonaceous chondrites are enriched in *r*-process Nd relative to the Earth and ordinary chondrites is consistent with the supernova injection model. However, recent theoretical studies suggest that ccSNe should not result in synthesis of *r*-process nuclides with mass numbers (A) greater than ~110 because the neutrino-driven wind from nascent protoneutron stars becomes proton-rich due to the interaction between neutrons and neutrinos (e.g., Fischer et al., 2010; Wanajo, 2013). If this were the case, late injection of supernovae materials would not have altered the compositions of *r*-process nuclides of Nd throughout the formation region of the Earth and chondrites in the early Solar System.

The second model hypothesizes that thermal processing in the solar nebula induced the nucleosynthetic isotope heterogeneities in refractory elements observed in meteorites (Trinquier et al., 2009; Burkhardt et al., 2012; Yokoyama and Walker, 2016). Burkhardt et al. (2012) argued that inconsistencies related to the presence and absence of nucleosynthetic isotope anomalies in Mo and W in bulk carbonaceous chondrites, respectively, were caused by selective destruction of thermally weak, isotopically anomalous carriers by nebular thermal processing, during which moderately refractory

Mo was released from the carrier to the gas phase in oxidizing conditions, whereas the highly refractory W ($T_{50\%}$ = 1790 K; Lodders, 2003) remained in the solid phase. Because Nd has a lower resolvable $T_{50\%}$ (1602 K) compared to that of W, we conclude that the Nd isotope anomalies observed in chondrites also resulted from nebular thermal processing.

Due to the thermal gradient in the solar nebula, dust grains present in the inner Solar System would have been thermally processed to a greater extent than those in the outer Solar System, resulting in a compositional gradient across the present asteroid belt (Gradie and Tedesco, 1982). Spectral observations suggest that the parent bodies of ordinary chondrites are most likely linked to S-type asteroids located mainly in the Inner Main Belt (2.0 to 2.5 AU), while those of carbonaceous chondrites are linked to C- and P-type asteroids located mainly in the Outer Main Belt (2.8 to 3.3 AU) (e.g., Gaffey et al., 1993). The isotopic characteristics observed in Fig. 4.5 suggests that nebular thermal processing would have selectively destroyed thermally weak dust grains depleted in *s*-process Nd in the inner Solar System where S-type asteroids formed. The dust grains enriched in *s*-process Nd (e.g., mainstream presolar SiC) would have survived the thermal processing and been incorporated into the parent bodies of ordinary chondrites, whereas both *s*-enriched and *s*-depleted dust grains were incorporated into the parent bodies of carbonaceous chondrites. The mineral phases corresponding to the thermally weak dust grains are difficult to determine at present because no such presolar grains have been identified in chondrites.

Regardless of the actual model responsible for the Nd isotopic variability between

ordinary chondrites and CAI-subtracted carbonaceous chondrites, it is important to note that ordinary chondrites and bulk aliquots of carbonaceous chondrites do not plot on a single line in Fig. 4.4. This observation implies the presence of two isotopically distinct reservoirs in the solar nebula that cannot be explained by the heterogeneous distribution of *s*-process nuclides alone. Such isotopic dichotomies between carbonaceous chondrites and the other meteorites have been reported for certain elements (O–Ti–Cr: Warren, 2011; Cr–Sr: Yokoyama et al., 2015; Mo: Budde et al., 2016, Worsham et al., 2017). These may be related to the presence of a young Jupiter core, which may have prevented effective mixing between the two reservoirs located within and beyond the orbit of Jupiter (Budde et al., 2016). As discussed above, the incorporation of CAIs produced an offset from the *s*-process–terrestrial mixing line for carbonaceous chondrites (Figs. 4.4b and 4.4d). Therefore, the most likely carrier phase responsible for the Nd isotopic dichotomy is CAI-like materials that were incorporated into the CAI-subtracted carbonaceous chondrite source reservoir, whereas admixing of the CAI-like materials into the inner Solar System was impeded by a Jupiter core. The results of our Nd isotope measurements on chondrites suggest that the phases carrying the lithophile elements responsible for producing the isotopic dichotomy between ordinary chondrites and bulk aliquots of carbonaceous chondrites were probably distinct from those of siderophile elements such as Mo, although they were similarly separated into two regions isolated by a young Jupiter core.

4.4.5 Origin of non-chondritic $^{142}Nd/^{144}Nd$ ratios in terrestrial materials

Our new Nd isotopic data for ordinary and carbonaceous chondrites provide an important clue to the origin of non-chondritic $^{142}Nd/^{144}Nd$ ratios in the accessible Earth's mantle. Previous studies assumed that the bulk Earth had a chondritic Nd isotopic composition, which suggested that the elevated $\mu^{142}Nd$ values (~20 ppm) in terrestrial materials relative to chondrites pointed to the existence of a missing reservoir with negative $\mu^{142}Nd$ values either hidden deep in the mantle or lost to space by collisional erosion of the early crust (e.g., Boyet and Carlson, 2005; Carlson et al., 2007; O'Neill and Palme, 2008; Dickin, 2016).

More recently, this scenario was challenged by Burkhardt et al. (2016) and Bouvier and Boyet (2016). In particular, the former argued that the average intercept values for the regression lines of bulk meteorites on $\mu^{142}Nd$ versus $\mu^{i}Nd$ (i = 145, 148, and 150) diagrams ($\mu^{142}Nd = -5 \pm 3$ ppm; weighted mean) were identical to those for processed terrestrial standards ($\mu^{142}Nd = -1 \pm 2$ ppm). This observation led the authors to conclude that the ^{142}Nd compositions of chondrites and the accessible silicate Earth were indistinguishable from one another after correcting for nucleosynthetic Nd isotope heterogeneities. In determining the *s*-process-corrected $\mu^{142}Nd$ value, however, Burkhardt et al. (2016) included one achondrite (NWA 5363) and processed terrestrial standards in addition to bulk enstatite, ordinary, and CAI-subtracted carbonaceous chondrites, whereas a value of -6.1 ± 4.1 ppm (weighted mean) was obtained when data for such non-chondritic samples were removed from the calculation of the intercept values. This negative shift primarily results from the data for ordinary (and possibly enstatite) chondrites measured by Burkhardt et al. (2016) that plot below the mixing line

between the *s*-process and terrestrial components in the μ^{142}Nd versus μ^{145}Nd, μ^{148}Nd, and μ^{150}Nd diagrams. In contrast, our data for bulk ordinary chondrites and CAI-subtracted Allende result in a weighted mean intercept value of −2.4 ± 4.8 ppm for the regression lines in the μ^{142}Nd versus μ^{148}Nd and μ^{150}Nd diagrams, representing an exact match between the ^{142}Nd compositions of chondrites and the accessible silicate Earth after correcting for nucleosynthetic isotope anomalies. We conclude that the variations in Nd isotope compositions in planetary materials reflects the heterogeneous distribution of *s*-process nuclides for ordinary and CAI-subtracted carbonaceous chondrites, which corroborates the interpretation that a missing reservoir (e.g., a hidden mantle reservoir, crustal loss by erosion) is not required to explain the observed difference in ^{142}Nd/^{144}Nd ratios between chondrites and terrestrial materials.

4.5 Conclusion

We conducted high-precision Nd isotope analyses on bulk ordinary and carbonaceous chondrites by applying a new sample digestion technique that achieves complete dissolution of acid-resistant presolar grains. From the results of this study, we reached the following conclusions:

- Ordinary chondrites have uniform, non-terrestrial μ^{148}Nd and μ^{150}Nd values while carbonaceous chondrites display μ^{148}Nd and μ^{150}Nd values greater than those of ordinary chondrites. On a μ^{150}Nd versus μ^{148}Nd diagram, the data for these chondrites plot along the mixing line between *s*-process and terrestrial components, implying that the non-terrestrial μ^{148}Nd and μ^{150}Nd values in the chondrites resulted from the heterogeneous distribution of *s*-process nuclides in the early Solar System.
- Ordinary chondrites had uniform, non-terrestrial μ^{142}Nd values that plot along the *s*-process and terrestrial mixing line in a μ^{142}Nd versus μ^{148}Nd diagram, whereas carbonaceous chondrites have systematically lower μ^{142}Nd values than the data for other chondrites plotted on the same mixing line in the same diagram. This negative shift may be due to the incorporation of CAIs, indicating that the Nd isotopic variability in ordinary and CAI-subtracted carbonaceous chondrites was caused solely by the heterogeneous distribution of *s*-process nuclides.
- Planetary-scale Nd isotope heterogeneities observed in bulk meteorites most likely resulted from nebular thermal processing that caused selective destruction of *s*-process-depleted dust grains in the inner Solar System where the parent bodies of ordinary chondrites formed. The Nd isotope dichotomy between ordinary and bulk

aliquots of carbonaceous chondrites can be related to the presence of Jupiter, which may have separated two isotopically distinct reservoirs that were present in the solar nebula.

- Our new Nd isotopic data for ordinary and a CAI-subtracted CV chondrite yield a weighted mean intercept value of −2.4 ± 4.8 ppm for the regression lines on μ^{142}Nd versus μ^{148}Nd and μ^{150}Nd diagrams, representing an exact match between the ^{142}Nd compositions of chondrites and the accessible silicate Earth. This corroborates the interpretation that a missing component (e.g., a hidden enriched mantle reservoir, erosional loss of crust) is not required to explain the observed difference in ^{142}Nd/^{144}Nd ratios between chondrites and terrestrial materials.

References

Andreasen, R., Sharma, M., 2006. Solar nebula heterogeneity in p-process samarium and neodymium isotopes. Science 314, 806-809.

Arlandini, C., Kappeler, F., Wisshak, K., Gallino, R., Lugaro, M., Busso, M., Straniero, O., 1999. Neutron capture in low-mass asymptotic giant branch stars: Cross sections and abundance signatures. Astrophysical Journal 525, 886-900.

Bermingham, K.R., Mezger, K., Scherer, E.E., Horan, M.F., Carlson, R.W., Upadhyay, D., Magna, T., Pack, A., 2016. Barium isotope abundances in meteorites and their implications for early Solar System evolution. Geochimica et Cosmochimica Acta 175, 282-298.

Bisterzo, S., Gallino, R., Kappeler, F., Wiescher, M., Imbriani, G., Straniero, O., Cristallo, S., Gorres, J., deBoer, R.J., 2015. The branchings of the main s-process: their sensitivity to alpha-induced reactions on ^{13}C and ^{22}Ne and to the uncertainties of the nuclear network. Monthly Notices of the Royal Astronomical Society 449, 506-527.

Bisterzo, S., Gallino, R., Straniero, O., Cristallo, S., Kappeler, F., 2011. The s-process in low-metallicity stars - II. Interpretation of high-resolution spectroscopic observations with asymptotic giant branch models. Monthly Notices of the Royal Astronomical Society 418, 284-319.

Bisterzo, S., Travaglio, C., Gallino, R., Wiescher, M., Kappeler, F., 2014. Galactic chemical evolution and solar s-process abundances: dependence on the ^{13}C pocket structure. Astrophysical Journal 787 (10).

Bouvier, A., Boyet, M., 2016. Primitive Solar System materials and Earth share a common initial ^{142}Nd abundance. Nature 537, 399-402.

Bouvier, A., Vervoort, J.D., Patchett, P.J., 2008. The Lu-Hf and Sm-Nd isotopic composition of CHUR: Constraints from unequilibrated chondrites and implications for the bulk composition of terrestrial planets. Earth and Planetary Science Letters 273, 48-57.

Boyet, M., Carlson, R.W., 2005. ^{142}Nd evidence for early (> 4.53 Ga) global differentiation of the silicate Earth. Science 309, 576-581.

Brennecka, G.A., Borg, L.E., Wadhwa, M., 2013. Evidence for supernova injection into the solar nebula and the decoupling of r-process nucleosynthesis. Proceedings of the National Academy of Sciences of the United States of America 110, 17241-17246.

Budde, G., Burkhardt, C., Brennecka, G. A., Fischer-Gödde, M., Kruijer, T. S., Kleine, T., 2016. Molybdenum isotopic evidence for the origin of chondrules and a distinct genetic heritage of carbonaceous and non-carbonaceous meteorites. Earth and Planetary Science Letters, 454, 293-303.

Burkhardt, C., Borg, L.E., Brennecka, G.A., Shollenberger, Q.R., Dauphas, N., Kleine, T., 2016. A nucleosynthetic origin for the Earth's anomalous ^{142}Nd composition. Nature 537, 394-398.

Burkhardt, C., Kleine, T., Dauphas, N., Wieler, R., 2012. Origin of isotopic heterogeneity in the solar nebula by thermal processing and mixing of nebular dust. Earth and Planetary Science Letters 357, 298-307.

Burkhardt, C., Kleine, T., Oberli, F., Pack, A., Bourdon, B., Wieler, R., 2011. Molybdenum isotope anomalies in meteorites: Constraints on solar nebula evolution and origin of the Earth. Earth and Planetary Science Letters 312, 390-400.

Carlson, R.W., Boyet, M., Horan, M., 2007. Chondrite barium, neodymium, and samarium isotopic heterogeneity and early earth differentiation. Science 316, 1175-1178.

Dauphas, N., Davis, A.M., Marty, B., Reisberg, L., 2004. The cosmic molybdenum-ruthenium isotope correlation. Earth and Planetary Science Letters 226, 465-475.

Dauphas, N., Remusat, L., Chen, J.H., Roskosz, M., Papanastassiou, D.A., Stodolna, J., Guan, Y., Ma, C., Eiler, J.M., 2010. Neutron-rich chromium isotope anomalies in supernova nanoparticles. Astrophysical Journal 720, 1577-1591.

Dickin, A.P., 2016. The Chondritic Moon: a solution to the Nd-142 conundrum and implications for terrestrial mantle evolution. Geological Magazine 153, 548-555.

Eugster, O., Lorenzetti, S., Krähenbühl, U., Marti, K., 2007. Comparison of cosmic-ray exposure ages and trapped noble gases in chondrule and matrix samples of ordinary, enstatite, and carbonaceous chondrites. Meteoritics and Planetary Science, 42, 1351-1371.

Fehr, M.A., Rehkaemper, M., Halliday, A.N., Schoenbaechler, M., Hattendorf, B., Guenther, D., 2006. Search for nucleosynthetic and radiogenic tellurium isotope

anomalies in carbonaceous chondrites. Geochimica Et Cosmochimica Acta 70, 3436-3448.

Fischer, T., Whitehouse, S.C., Mezzacappa, A., Thielemann, F.K., Liebendörfer, M. 2010. Protoneutron star evolution and the neutrino-driven wind in general relativistic neutrino radiation hydrodynamics simulations. Astronomy and Astrophysics 517 (A80).

Friedrich, J.M., Wang, M.S., Lipschutz, M.E., 2002. Comparison of the trace element composition of Tagish Lake with other primitive carbonaceous chondrites. Meteoritics and Planetary Science 37, 677-686.

Fukami, Y., Yokoyama, T., 2017. Tellurium isotope compositions in acid leach fractions of carbonaceous chondrites. Geochemical Journal 51 (1), 17-29.

Gaffey, M.J., Bell, J.F., Brown, R.H., Burbine, T.H., Piatek, J.L., Reed, K.L., Chaky, D.A., 1993. Mineralogical variations within S-type asteroid class. Icarus 106, 573-602.

Gannoun, A., Boyet, M., Rizo, H., El Goresy, A., 2011. ^{146}Sm–^{142}Nd systematics measured in enstatite chondrites reveals a heterogeneous distribution of ^{142}Nd in the solar nebula. Proceedings of the National Academy of Sciences of the United States of America 108, 7693-7697.

Gradie, J., Tedesco, E., 1982. Compositional structure of the asteroid belt. Science 216, 1405-1407.

Hezel, D. C., Russell, S. S., Ross, A. J., Kearsley, A. T., 2008. Modal abundances of CAIs: Implication for bulk chondrite element abundances and fractionations. Meteoritics and Planetary Science 43, 11, 1879-1894.

Hoppe, P., Ott, U., 1997. Mainstream silicon carbide grains from meteorites. AIP Conference Proceedings 402, 27-58.

Kagami, S., Yokoyama, T., 2016. Chemical separation of Nd from geological samples for chronological studies using ^{146}Sm–^{142}Nd and ^{147}Sm–^{143}Nd systematics. Analytica Chimica Acta 937, 151-159.

Lodders, K., 2003. Solar system abundances and condensation temperatures of the elements. Astrophysical Journal 591, 1220-1247.

Marks, N. E., Borg, L. E., Hutcheon, I. D., Jacobsen, B., Clayton, R. N. 2014. Samarium–neodymium chronology and rubidium–strontium systematics of an Allende calcium–aluminum-rich inclusion with implications for ^{146}Sm half-life. Earth and Planetary Science Letters 405, 15-24.

Moynier, F., Day, J.M.D., Okui, W., Yokoyama, T., Bouvier, A., Walker, R.J., Podosek, F.A., 2012. Planetary-scale strontium isotopic heterogeneity and the age of volatile depletion of early solar system materials. Astrophysical Journal 758 (45).

O'Neill, H.S.C., Palme, H., 2008. Collisional erosion and the non-chondritic composition of the terrestrial planets. Philosophical Transactions of the Royal Society a-Mathematical Physical and Engineering Sciences 366, 4205-4238.

Saji, N. S., Wielandt, D., Paton, C., Bizzarro, M., 2016. Ultra-high-precision Nd-isotope measurements of geological materials by MC-ICPMS. Journal of Analytical Atomic Spectrometry 31 (7), 1490-1504.

Scott, E.R.D., Krot, A.N., 2014. Chondrites and Their components, 2nd edition. Treatise on Geochemistry, 65-137.

Sprung, P., Scherer, E.E., Upadhyay, D., Leya, I., Mezger, K., 2010. Non-nucleosynthetic heterogeneity in non-radiogenic stable Hf isotopes: Implications for early solar system chronology. Earth and Planetary Science Letters 295, 1-11.

Tazoe, H., Obata, H., Gamo, T., 2007. Determination of cerium isotope ratios in geochemical samples using oxidative extraction technique with chelating resin. Journal of Analytical Atomic Spectrometry 22, 616-622.

Trinquier, A., Birck, J.-L., Allegre, C.J., 2007. Widespread ^{54}Cr heterogeneity in the inner solar system. Astrophysical Journal 655, 1179-1185.

Trinquier, A., Elliot, T., Ulfbeck, D., Coath, C., Krot, A.N., Bizzarro, M., 2009. Origin of nucleosynthetic heterogeneity in the solar protoplanetary disk. Science 324, 374-376.

Wanajo, S., 2013. The r-process in proto-neutron-star wind revisited. Astrophysical Journal Letters 770 (L22).

Warren, P. H., 2011. Stable-isotopic anomalies and the accretionary assemblage of the Earth and Mars: A subordinate role for carbonaceous chondrites. Earth and Planetary Science Letters 311 (1), 93-100.

Worsham, E. A., Bermingham, K. R., Walker, R. J., 2017. Characterizing cosmochemical materials with genetic affinities to the Earth: Genetic and chronological diversity within the IAB iron meteorite complex. Earth and Planetary Science Letters 467, 157-166.

Yokoyama, T., Alexander, C.M.O.D., Walker, R.J., 2010. Osmium isotope anomalies in chondrites: Results for acid residues and related leachates. Earth and Planetary Science Letters 291, 48-59.

Yokoyama, T., Fukami, Y., Okui, W., Ito, N., Yamazaki, H., 2015. Nucleosynthetic strontium isotope anomalies in carbonaceous chondrites. Earth and Planetary Science Letters 416, 46-55.

Yokoyama, T., Nagai, Y., Hinohara, Y., Mori, T., 2017. Investigating the influence of nonspectral matrix effects for determination 22 trace elements in rock samples by ICP-QMS. Geostandards and Geoanalytical Research 41 (2), 221-242.

Yokoyama, T., Rai, V.K., Alexander, M.O.D., Lewis, R.S., Carlson, R.W., Shirey, S.B., Thiemens, M.H., Walker, R.J., 2007. Osmium isotope evidence for uniform distribution of s- and r-process components in the early solar system. Earth and Planetary Science Letters 259, 567-580.

Yokoyama, T., Walker, R.J., 2016. Nucleosynthetic Isotope Variations of Siderophile and Chalcophile Elements in the Solar System. Highly Siderophile and Strongly Chalcophile Elements in High-Temperature Geochemistry and Cosmochemistry 81, 107-160.

Chapter 5:
Nucleosynthetic Sr–Nd isotope correlations in chondrites: Evidence for nebular thermal processing and dust transportation in the early Solar System

Abstract

We conducted high-precision Sr and Nd isotopic measurements for bulk aliquots of chondrites by applying a complete sample digestion technique. Our new high-precision data indicate that enstatite and ordinary chondrites possess uniform and small, but resolvable, Sr and Nd isotopic deviations from terrestrial rocks. In contrast, we found Sr and Nd isotopic variations across different classes of carbonaceous chondrites (CM, CO, and CV), of which the data points deviate from the *s*-process mixing line in the Sr–Nd isotopic space. This shift likely resulted from the incorporation of calcium- and aluminum-rich inclusions (CAIs) into carbonaceous chondrite parent bodies. The planetary-scale Sr and Nd isotopic heterogeneities among terrestrial rocks, enstatite, ordinary, and CAI-subtracted carbonaceous chondrites point to the heterogeneous distribution of *s*-process enriched materials in the early Solar System, which was most likely caused by the global nebular thermal processing. On the other hand, the observed Sr and Nd isotopic variation across CAI-subtracted carbonaceous chondrites cannot be explained solely by the nebular thermal processing. Rather, this isotopic variation was caused by the involvement of *s*-process-depleted silicate grains that repeatedly circulated in the early Solar System, which were transferred and incorporated at varying degrees into the region where parent bodies of individual carbonaceous chondrites have formed. On the other hand, Sr and Nd isotopic compositions for CI chondrites are not explained by this disk evolutionary model, most likely due to the injection of supernovae materials and/or input of materials from the molecular cloud.

5.1 Introduction

Formation of the Solar System has been triggered by the gravitational collapse of molecular cloud core composed of gas and presolar dust grains that originated from diverse stellar environments (asymptotic giant-branch (AGB) stars, supernovae, and possibly novae). The early Solar System has been considered to be isotopically homogeneous as a result of destruction and mixing of presolar dust grains via multiple physical processes occurring in the molecular cloud and the solar nebula. However, the finding of planetary-scale isotopic variability for refractory heavy elements in bulk meteorites revealed that the early Solar System was not isotopically homogeneous as was previously thought. The observed isotopic heterogeneity in bulk meteorites is most likely nucleosynthetic in origin, which would provide useful information regarding the physical and chemical condition of the early Solar System.

Recently, Warren (2011) proposed a new taxonomy of meteorites based on the stable isotopic compositions of O, Ti, Cr, and Ni, by which stony meteorites can be divided into carbonaceous chondrites (CCs) and the other meteorites (non-carbonaceous meteorites (NCs): enstatite chondrites, ordinary chondrites, rumuruti chondrites, and most of differentiated meteorites). Such an "isotopic dichotomy" between CCs and NCs have been reported for the other isotopic systems including Mo (Budde et al., 2016; Kruijer et al., 2017; Poole et al., 2017; Worsham et al., 2017) and Nd (Fukai and Yokoyama, 2017). The observation implies the presence of two isotopically distinct reservoirs in the solar nebula. Previous studies argued that the isotopic dichotomy could be generated by the input of isotopically anomalous materials such as supernovae grains

and calcium- and aluminum-rich inclusions (CAIs) into the region where CCs have formed (Budde et al., 2016; Fukai and Yokoyama, 2017; Worsham et al., 2017). However, any single model proposed in the previous studies does not conclusively explain the cause of isotopic dichotomy for multiple isotopic systems observed in bulk meteorites.

Strontium is an intriguing element for studying the origin of isotopic dichotomy observed in meteorites. Strontium has four isotopes that are produced by stellar nucleosynthesis of the *p*-process (^{84}Sr) and *s*-process (^{86}Sr, ^{87}Sr, and ^{88}Sr), while a small portion of ^{88}Sr is produced by the *r*-process. Recent high-precision isotopic analyses by thermal ionization mass spectrometry (TIMS) revealed that bulk aliquots of chondrites and differentiated meteorites possess variable ^{84}Sr/^{86}Sr ratios, which would reflect varying contribution of the multiple nucleosynthetic components originated from diverse stellar environments among different classes of meteorites (Andreasen and Sharma, 2007; Moynier et al., 2012; Paton et al., 2013; Yokoyama et al., 2015). However, several analytical problems have hindered the understanding of extent and origin of Sr isotope heterogeneity across entire classes of meteorites. For instance, accurate Sr isotopic data for bulk CCs with sufficiently high-precision are limited, because most of the previous studies did not conduct complete sample digestion of primitive CCs that contained acid-resistant and isotopically anomalous presolar grains (Andreasen and Sharma, 2007; Moynier et al., 2012; Paton et al., 2013). The importance of complete sample digestion has been demonstrated in several previous studies on nucleosynthetic isotope anomalies in unequilibrated chondrites (e.g., Ba: Bermingham

et al., 2016; Os: Yokoyama et al., 2007, 2010). Additionally, simultaneous measurements of multiple isotope systems using single aliquots of meteorite samples were not performed in the previous studies on nucleosynthetic Sr isotope anomalies in bulk chondrites (Moynier et al., 2012; Paton et al., 2013; Yokoyama et al., 2015), although these studies attempted to directly compare the results of Sr isotope anomalies with the other isotope systems (O and Cr). It should be noted that the direct comparison of Sr isotope data with the other isotopic systems is specifically important because these studies corrected mass-dependent Sr isotopic fractionation occurring in mass spectrometer using two stable Sr isotopes ($^{88}Sr/^{86}Sr$), so that only $^{84}Sr/^{86}Sr$ ratio can be used to trace nucleosynthetic Sr isotope anomalies in meteorites.

In this study, we revisited nucleosynthetic Sr isotope anomalies in bulk chondrites, of which the data were newly obtained by high-precision isotopic analyses with TIMS (reproducibilities: ±20–30 ppm; 2 SD) coupled with an aggressive sample digestion technique that confirmed complete dissolution of acid-resistant presolar grains. Furthermore, all of the Sr isotope data in chondrites were directly compared with the Nd isotope data obtained either in this study or in Fukai and Yokoyama (2017) by using the same sample solution dedicated for the Sr isotopic analyses. Neodymium isotope ratios in bulk chondrites are good tracers to assist understanding the cause of nucleosynthetic Sr isotope heterogeneity in meteorites, because Sr and Nd have similar physicochemical characteristics with respect to affinity to silicates over metal phases (lithophile elements), incompatibility to solid phase during silicate melting, and refractory behavior in cosmochemical environments. With the new comprehensive dataset for Sr and Nd

isotopic compositions in bulk chondrites, we propose a new disk evolutionary model that accounts for the planetary-scale Sr and Nd isotope heterogeneities in the early Solar System.

5.2 Experimental procedures

We investigated two terrestrial basalts (JB-1a and JB-3; rock reference materials from the Geological Survey of Japan), four enstatite chondrites (Y-691, EH3; SAH 97072, EH3; Y-980223, EH6; A-882039, EL6), five ordinary chondrites (Forest City, H5; Saratov, L4; Modoc (1905), L6; Tuxtuac, LL5, Saint-Séverin, LL6), two rumuruti chondrites (NWA 753, R3.9; NWA 4814, R4) and seven different classes of carbonaceous chondrites (Orgueil, CI1; Y-980115, CI1; Dho 1432, CR2; Murchison, CM2; Jbilet Winselwan, CM2; Kainsaz, CO3; DaG 190, CO3; Allende, CV3; DaG 412, CK5; SaU 290, CH3). First, the meteorite samples were fragmented into chips using an iron mortar. The meteorite chips were cleaned with distilled acetone and H_2O (Milli-Q) for 30 min in an ultrasonic bath. Then the chips were powdered using either an agate mortar and pestle or a sample homogenizer (Multi-beads shocker®; Yasui Kikai, Japan), with which the rock chips were pulverized in polyethylene bottles at 2500 rpm for 900 s.

The concentrations of trace elements including Rb, Sr, Nd, and Sm in the meteorite samples were determined by the isotope dilution-internal standard (ID-IS) method using a quadrupole-type inductively coupled plasma-mass spectrometry (Q-type ICP-MS: X-Series 2; Thermo Fischer Scientific, USA) following the procedure described in Yokoyama et al. (2017). In brief, ~5% of sample aliquots of meteorite and terrestrial rocks were saved to determine the concentration of trace elements after the protocol for sample digestion. A solution of ^{113}In–^{203}Tl mixed spike was added to the solutions and diluted by 0.5M HNO_3 to appropriate dilution factor (DF = ~2000) for the

measurements of ICP-MS. A multi-element solution prepared from four certified reference materials was used as the standard for the determination of concentrations (Yokoyama et al., 2017).

Bulk chondrite samples with a petrologic grade of less than 4, which contain isotopically anomalous acid-resistant presolar grains, were digested using the procedures using a high-pressure digestion system as described in Yokoyama et al. (2015). To dissolve chondrite samples including acid-resistant grains aggressively, these meteorite samples (~500 mg) were placed in a polytetrafluoroethylene (PTFE) insert (50 mL vol.) in a high-pressure digestion system (DAB-2; Berghof, Germany), together with 6.8 mL 30 M HF (AAS grade with distillation; Kanto Chemical, Japan), 4.8 mL 16 M HNO_3 (EL grade with distillation; Mitsubishi Chemical, Japan), and 9.6 mL 96% H_2SO_4 (Ultrapur-grade; Kanto Chemical, Japan). A 500 mg of reference rock sample (JB-3) was also digested following this procedure to verify the accuracy of the aggressive digestion. Chondrite samples with the petrologic grade of 4 or greater were digested using the procedures without high-pressure digestion system as described in Yokoyama et al. (2017). Powdered samples (up to 2 g) were placed in Teflon vessels with a 1:1:1 mixture of 30 M HF, 12 M $HClO_4$ (AA–100 grade; TAMA Chemical, Japan), and 16 M HNO_3 in proportions of 1 mL of each acid per 0.1 g of sample.

For Sr isotope analysis, we conducted a 3-step column separation procedure. The sample solution was loaded onto a 1:1 mixture of two cation-exchange resins (AG50WX8 and AG50WX12; Bio-Rad, USA) in order to remove major elements (e.g., Mg, Al, Fe). Then, Sr was separated from Rb using Sr resin (100–150 μm; Eichrom

Technologies, USA) following Yokoyama et al. (2015). A fraction of REEs and other matrix elements was removed and dedicated for the separation of Nd from the other REEs. This procedure was repeated twice to purify Sr fraction. For Nd isotope analysis, Ce was removed from the remaining REEs by passing the solution through LN resin (50–100 μm; Eichrom Technologies), during which Ce^{3+} in the sample solution (10 M HNO_3) was oxidized to Ce^{4+} using $KBrO_3$ (Kagami and Yokoyama, 2016). Finally, Nd was separated from Sm using the LN resin in HCl media. The amounts of Sr and Nd in the blank resulting from the entire chemical procedure were 290 and 8.0 pg, respectively. Because we collected > ~10 μg of Sr and > ~250 ng of Nd from a single aliquot (> 500 mg), the observed quantities of blank do not affect the results of Sr and Nd isotopic ratios for the meteorite and terrestrial samples obtained in this study.

All isotope measurements were performed using TIMS instrument (Triton *Plus*; Thermo Fischer Scientific) installed at the Tokyo Institute of Technology. The instrument is equipped with nine Faraday cups and 10^{11} Ω resistors. Strontium was ionized using a single W filament (thickness: 0.0254 mm, width: 0.762 mm; Nilaco, Japan) that was outgassed under vacuum conditions prior to use. Then, 2 μL Ta_2O_5 activator dissolved in 0.5M HNO_3 was loaded onto each filament. We obtained $^{88}Sr^+$ beam intensity reaching 15–30 V during single measurement. Strontium isotopes were collected with a two-jump cup configuration within a single measurement run (Table 5.1), in which the $^{84}Sr/^{86}Sr$ ratio was obtained by the dynamic and multistatic methods while the $^{87}Sr/^{86}Sr$ ratio was obtained solely by the multistatic method. We performed two-jump isotopic measurements by two different settings (methods A and B) regarding

the integration time and idle time. The integration time was 8.389 and 16.777 s for Jumps 1 and 2 in method A, and 16.777 s for both Jumps 1 and 2 in method B, respectively. The idle time between Jumps 1 and 2 was 4.0 s in method A and 10 s in method B. Individual isotopic measurement consisted of 140 or 280 ratios. Mass-dependent isotopic fractionation during measurements was corrected by the exponential law and normalized using the ratio of $^{88}Sr/^{86}Sr = 8.37521$.

Table 5.1 *Analytical conditions for Sr and Nd isotope measurements with TIMS.*

	L4	L3	L2	L1	C	H1	H2	H3	H4	Integration time	Idle time
Sr isotope measurements – method A											
Jump 1			^{84}Sr	^{85}Rb	^{86}Sr	^{87}Sr	^{88}Sr			8.389 s	4.000 s
Jump 2					^{84}Sr	^{85}Rb	^{86}Sr	^{87}Sr	^{88}Sr	16.777 s	4.000 s
Sr isotope measurements – method B											
Jump 1			^{84}Sr	^{85}Rb	^{86}Sr	^{87}Sr	^{88}Sr			16.777 s	4.000 s
Jump 2					^{84}Sr	^{85}Rb	^{86}Sr	^{87}Sr	^{88}Sr	16.777 s	10.00 s
Nd isotope measurements											
Jump 1	^{140}Ce	^{142}Nd	^{143}Nd	^{144}Nd	^{145}Nd	^{146}Nd	^{147}Sm	^{148}Nd	^{150}Nd	16.777 s	4.000 s
Jump 2		^{140}Ce		^{142}Nd	^{143}Nd	^{144}Nd	^{145}Nd	^{146}Nd	^{148}Nd	16.777 s	4.000 s

Strontium and Nd isotope collection consisted of two lines in one cycle, 20 cycles in one block in a single measurement. The total analytical time for a single measurement were 3.0 h (Sr) and 4.5 h (Nd) including a baseline measurement (30 s) at the beginning of each block, beam focusing every 3 blocks, and peak centering every 5 blocks. Mass interferences for Sr from Rb are monitored at ^{85}Rb (Jumps 1 and 2) by assuming $^{87}Rb/^{85}Rb = 0.38571$. Mass interferences for Nd from Ce and Sm are monitored at ^{140}Ce (Jump 1 and 2) and ^{147}Sm (Jump 1) by assuming $^{142}Ce/^{140}Ce = 0.12565$, $^{144}Sm/^{147}Sm =$

0.20498, $^{148}Sm/^{147}Sm$ = 0.74970, and $^{150}Sm/^{147}Sm$ = 0.49219.

Generally, the static method is susceptible to the modification of Faraday cup efficiencies (Chapter 2). In contrast, the dynamic method can cancel out the effect of Faraday cup efficiencies. The multistatic method is a protocol for averaging the multiple isotopic ratios measured by the static method, which can reduce the effect of Faraday cups deterioration. In method A, the analytical reproducibilities (2 SDs) of $^{84}Sr/^{86}Sr$ ratio were ±32 ppm and ±21 ppm for Jumps 1 and 2 in the static method, respectively, ±25 ppm in the dynamic method, and ±18 ppm in the multistatic method. Those in method B were ±48 ppm and ±27 ppm for Jumps 1 and 2 in the static method, respectively, ±22 ppm in the dynamic method, and ±30 ppm in the multistatic method.

The protocol for Nd isotope measurements was similar to those described in Chapter 4. Fukai et al. (2017) and subsequent studies (e.g., Garçon et al., 2018) concluded that the dynamic method achieved the most precise and accurate measurements in the Nd isotope analysis. In this study, we only report the Nd isotope data calculated by the dynamic method except for $^{143}Nd/^{144}Nd$ and $^{145}Nd/^{144}Nd$ ratios, which cannot be calculated by the dynamic method in our two-jump cup configuration (Table 5.1). The reproducibilities of the Nd isotope ratios obtained by the dynamic method during each analytical campaign were ±4.8, ±5.6, and ±10 ppm (2 SDs) on average for $^{142}Nd/^{144}Nd$, $^{148}Nd/^{144}Nd$, and $^{150}Nd/^{144}Nd$ ratios, respectively. The Nd isotope ratio reproducibilities obtained by the multistatic method were ±10 ppm and ±20 ppm (2 SDs) on average for $^{143}Nd/^{144}Nd$ and $^{145}Nd/^{144}Nd$ ratios, respectively.

5.3 Results

Throughout this paper, the Sr and Nd isotope ratios (excluding $^{87}Sr/^{86}Sr$ and $^{143}Nd/^{144}Nd$) for meteorite and terrestrial rock samples are reported in μ notations, which represent parts per 10^6 deviations from the mean values of repeated analyses for NIST 987 ($\mu^{84}Sr = (R_{sample}/R_{standard} - 1) \times 10^6$, $R = {}^{84}Sr/^{86}Sr$) and JNdi-1 ($\mu^{i}Nd = (R_{sample}/R_{standard} - 1) \times 10^6$, $R = {}^{i}Nd/^{144}Nd$, i = 142, 145, 148, and 150). Tables 5.2 and 5.3 summarize the Sr and Nd isotope ratios for terrestrial and chondrite samples obtained in this study. For samples measured three times or more, the reported analytical errors are either 2 SDs of the multiple sample measurements or the average analytical uncertainties of multiple campaigns for the standards (2 SDs), whichever is larger. For samples measured twice, the analytical errors are represented as the average analytical uncertainties of multiple campaigns for the standards (2 SDs). For samples measured once, the analytical errors are either the internal error of a single measurement or the analytical uncertainty for the standards (2 SD) measured in the same analytical campaign, whichever is larger.

Table 5.2 *Strontium isotope compositions for the terrestrial materials and whole-rock chondrites.*

Sample	Type	Find or Fall	Method	N	$\mu^{84}Sr$ (dynamic)	$\mu^{84}Sr$ (multistatic)	$^{87}Sr/^{86}Sr$	$^{87}Rb/^{86}Sr$
Terrestrial samples								
JB-1a	Basalt		A	2	–21 ± 25	–24 ± 18	0.704085 (7)	-
JB-3 (high-T, high-P dig.)	Basalt		A	4	–10 ± 29	–19 ± 21	0.703397 (7)	-
			B	4	–18 ± 22	–17 ± 30	0.703389 (5)	-
JB-3	Basalt		A	4	–16 ± 36	–19 ± 26	0.703402 (7)	0.029 ± 0.001

Enstatite chondrites								
Y-691	EH3	Antarctic	A	3	–11 ± 25	–7.8 ± 21	0.773812 (15)	-
Y-980223	EH6	Antarctic	A	3	3.9 ± 33	3.9 ± 18	0.832588 (73)	1.36 ± 0.02
A-882039	EL6	Antarctic	A	3	5.9 ± 25	6.6 ± 18	0.747469 (14)	0.67 ± 0.03
SAH 97072	EH3	Desert	A	3	8.1 ± 25	–1.1 ± 30	0.777763 (2)	0.91 ± 0.01
Ordinary chondrites								
Forest City	H5	Fall	A	3	2.8 ± 25	–5.8 ± 18	0.750708 (7)	0.69 ± 0.01
Saratov	L4	Fall	A	3	8.5 ± 25	–1.9 ± 25	0.763204 (14)	0.764 ± 0.008
Modoc (1905)	L6	Fall	B	2	2.4 ± 24	11 ± 30	0.755593 (4)	0.842 ± 0.008
Tuxtuac	LL5	Fall	A	3	7.1 ± 25	7.0 ± 18	0.736231 (7)	0.54 ± 0.01
Saint-Séverin	LL6	Fall	B	2	4.5 ± 24	4.5 ± 30	0.708459 (4)	0.165 ± 0.003
Rumuruti chondrites								
NWA 753	R3.9	Desert	A	3	–21 ± 30	–10 ± 18	0.720526 (7)	0.196 ± 0.003
NWA 4814	R4	Desert	A	3	–4.5 ± 25	–11 ± 18	0.725842 (4)	0.19 ± 0.01
Carbonaceous chondrites								
Y-980115	CI1	Antarctic	A	4	18 ± 25	10 ± 18	0.762080 (11)	1.01 ± 0.02
Orgueil	CI1	Fall	A	2	–1.3 ± 25	0.8 ± 18	0.760183 (7)	1.01 ± 0.02
Kainsaz	CO3	Fall	B	2	42 ± 24	49 ± 30	0.719373 (4)	0.30 ± 0.01
Murchison	CM2	Fall	A	3	39 ± 30	46 ± 34	0.735977 (33)	
			B	2	39 ± 22	39 ± 30	0.735977 (8)	0.510 ± 0.009
Murchison ave.				*5*	*39 ± 24*	*43 ± 26*	*0.735977*	
Allende	CV3	Fall	A	3	66 ± 25	63 ± 24	0.714614 (9)	
			B	1	69 ± 22	54 ± 30	0.714608 (4)	0.224 ± 0.004
Allende ave.				*4*	*67 ± 24*	*61 ± 24*	*0.714612*	
Dho 1432	CR2	Desert	A	3	–11 ± 25	–6.4 ± 29	0.708274 (2)	0.0055 ± 0.0001
DaG 190	CO3	Desert	A	4	30 ± 25	24 ± 19	0.713490 (9)	0.081 ± 0.004
Jbilet Winselwan	CM2	Desert	B	1	–12 ± 22	–11 ± 30	0.715199 (4)	0.072 ± 0.001
SaU 290	CH3	Desert	A	2	–4.3 ± 25	–19 ± 18	0.709146 (7)	0.0185 ± 0.0008
DaG 412	CK5	Desert	A	3	41 ± 25	39 ± 18	0.708489 (10)	0.088 ± 0.003

Analytical errors for samples with N ≥ 3 are either 2 SDs of multiple measurements or average analytical uncertainties from multiple campaigns for NIST 987, whichever is

larger. Analytical errors with N = 2 are represented as average analytical uncertainties from multiple campaigns for NIST 987. Analytical errors for samples with N = 1 are either the internal uncertainties of a single measurement or the analytical uncertainty of NIST 987 (2 SDs) measured in the same analytical campaign, whichever is larger. The numbers in parentheses for $^{87}Sr/^{86}Sr$ ratios are individual analytical errors in the final digit.

Table 5.3 *Neodymium isotope compositions for the terrestrial materials and whole-rock chondrites measured in this study and Fukai and Yokoyama (2017).*

Sample	N	$\mu^{142}Nd$	$\mu^{142}Nd_{143Nd\_corr.}$	$\mu^{145}Nd$	$\mu^{148}Nd$	$\mu^{150}Nd$	$^{143}Nd/^{144}Nd$	$^{147}Sm/^{144}Nd$	Reference
Terrestrial samples									
JB-1a	4	–2.2 ± 4.8	-	–3.9 ± 20	–1.6 ± 8.8	1.5 ± 14	0.512781 (9)	-	This study
JB-3 (high-T, high-P dig.)	1	1.5 ± 3.0	-	–4.3 ± 3.6	3.4 ± 3.8	8.1 ± 8.9	0.513057 (3)	0.16 ± 0.05	This study
JB-3	5	–0.2 ± 5.5	-	2.3 ± 16	0.5 ± 8.6	4.6 ± 13	0.513060 (10)	-	F17 (1)
Enstatite chondrites									
Y-691	1	–14 ± 5.7	–12 ± 5.7	23 ± 37	8.8 ± 7.5	11 ± 12	0.512598 (4)	-	This study
Y-980223	1	–24 ± 5.1	–15 ± 5.1	–16 ± 27	5.7 ± 5.9	15 ± 11	0.512458 (5)	0.19 ± 0.03	This study
Ordinary chondrites									
Forest City	1	–12 ± 7.4	–12 ± 7.4	17 ± 27	11 ± 7.6	17 ± 19	0.512633 (3)	0.196 ± 0.003	F17
Saratov	2	–14 ± 5.1	–13 ± 5.1	6.8 ± 16	13 ± 5.9	20 ± 11	0.512616 (6)	0.196 ± 0.002	F17
Modoc (1905)	2	–11 ± 5.1	–12 ± 5.1	–6.1 ± 16	8.1 ± 5.9	6.0 ± 11	0.512510 (5)	0.195 ± 0.002	F17
Tuxtuac	2	–19 ± 5.1	–13 ± 5.1	–7.3 ± 16	6.4 ± 5.9	13 ± 11	0.512643 (5)	0.192 ± 0.002	F17
Saint-Séverin	1	–12 ± 7.8	–8.9 ± 7.8	–5.7 ± 14	10 ± 12	23 ± 12	0.512571 (7)	0.191 ± 0.002	F17
Carbonaceous chondrites									
Orgueil	1	–21 ± 3.0	–21 ± 3.0	5.8 ± 3.6	2.0 ± 4.8	–2.1 ± 8.9	0.512639 (3)	0.20 ± 0.06	This study
Kainsaz	2	–35 ± 4.8	–35 ± 4.8	3.7 ± 20	21 ± 5.6	26 ± 10	0.512633 (5)	0.21 ± 0.04	This study
Murchison	4	–31 ± 7.4	–31 ± 7.4	2.1 ± 16	23 ± 13	24 ± 24	0.512613 (5)	0.197 ± 0.002	F17
Allende	4	–32 ± 7.5	–31 ± 7.5	–1.1 ± 16	19 ± 16	27 ± 26	0.512608 (19)	0.195 ± 0.002	F17
Dho 1432	1	–28 ± 3.8	–30 ± 3.8	16 ± 15	18 ± 5.4	26 ± 9.5	0.512677 (5)	0.195 ± 0.003	F17
DaG 190	1	–34 ± 4.0	–34 ± 4.0	19 ± 27	22 ± 4.6	27 ± 7.4	0.512641 (5)	0.197 ± 0.002	F17

The numbers in parentheses for $^{143}Nd/^{144}Nd$ are individual analytical errors in the final digit. $\mu^{142}Nd_{143Nd\_corr.}$ denotes $\mu^{142}Nd$ corrected for radiogenic ^{142}Nd variations to a common chondritic value ($^{143}Nd/^{144}Nd$ = 0.512630; Bouvier et al. 2008). Errors for $\mu^{142}Nd_{143Nd\_corr.}$ are derived from the analytical errors of $\mu^{142}Nd$ propagated to the errors on the $^{143}Nd/^{144}Nd$ ratios, respectively.

References. *(1) Fukai and Yokoyama, 2017*

Table 5.4 *Mean $^{84}Sr/^{86}Sr$ ratios and the analytical reproducibilities of repeated analyses for NIST 987.*

Sample	Method	N	$^{84}Sr/^{86}Sr$ (dynamic)	2 SD (ppm)	$^{84}Sr/^{86}Sr$ (multistatic)	2 SD (ppm)	$^{84}Sr/^{86}Sr$ (static Jump 1)	2 SD (ppm)	$^{84}Sr/^{86}Sr$ (static Jump 2)	2 SD (ppm)
NIST 987	A	25	0.0564909	25	0.0564904	18	0.0564955	32	0.0564854	21
NIST 987 (separated)	A	8	0.0564913	21	0.0564903	17	0.0564954	29	0.0564852	22
NIST 987	B	8	0.0564923	22	0.0564905	30	0.0564958	48	0.0564853	27

5.3.1 Sr isotope measurements

5.3.1.1 Standard and terrestrial samples

The results of repeated analyses for NIST 987 are presented in Table 5.4. We conducted two-jump cup configuration measurements with two distinct idle time (4.0 s or 10 s). Notably, the mean $^{84}Sr/^{86}Sr$ ratio measured by the dynamic method with method B (10 s for idle time between Jumps 1 and 2) was higher by +20 ppm from that measured with method A (4.0 s for idle time). In contrast, the mean $^{84}Sr/^{86}Sr$ ratios calculated by the static and multistatic methods did not show any differences between methods A and B. The isotopic difference in the dynamic method would be caused by

the memory effects of amplifier noises generated by two-jump cup configuration measurements, which is called the "decay DAC problem" (Yobregat et al., 2017). In addition to NIST 987, we performed Sr isotopic measurements for the terrestrial basaltic sample (JB-3) by both of the methods. In spite of the different mean $^{84}Sr/^{86}Sr$ ratios for NIST 987, the $\mu^{84}Sr$ values of JB-3 measured by the method A and B are indistinguishable from each other (Table 5.2). This result implies that the difference of the idle time did not affect the results of the isotopic deviations from the standard.

In our results, the terrestrial basalts showed negative $\mu^{84}Sr$ values (–24 to –10 ppm) in the dynamic and multistatic method measurements (Table 5.2). This result is inconsistent with recent studies that performed high-precision Sr isotopic analyses by the dynamic method (Yobregat et al., 2017; Henshall et al., 2018). These studies argued that the Sr isotopic compositions of NIST 987 and terrestrial rocks were identical to each other when measured by the dynamic method. Yobregat et al. (2017) proposed a hypothesis that the inconsistency of $^{84}Sr/^{86}Sr$ ratios between NIST 987 and terrestrial rocks observed in some previous studies would be generated by the difference of mass fractionation factors during individual measurement run. In contrast to this argument, we did not observe any significant difference in the fractionation factors for NIST 987 and terrestrial rocks, whereas we obtained negative $\mu^{84}Sr$ values for terrestrial rocks. At this point, the presence of inconsistency regarding $\mu^{84}Sr$ between NIST 987 and terrestrial rocks is still uncertain. In this study, therefore, we consider that terrestrial rock samples possess Sr isotopic composition of the bulk Earth.

5.3.1.2 Bulk chondrites

The classification of "non-carbonaceous meteorites (NCs)" defined by Warren (2011) includes meteorites except for carbonaceous chondrites (CCs) and carbonaceous chondrites-like ungrouped achondrites such as NWA 011. The NCs measured in this study are enstatite, ordinary, and rumuruti chondrites, which presented invariable $\mu^{84}Sr$ values within individual groups. The mean $\mu^{84}Sr$ values for four enstatite chondrites, five ordinary chondrites, two rumuruti chondrites obtained with the dynamic method were 1.7 ± 25 ppm, 5.5 ± 24 ppm, –13 ± 25 ppm, respectively, and those obtained with the multistatic method were 0.4 ± 18 ppm, 2.9 ± 24 ppm, –11 ± 24 ppm, respectively (errors are 2 SDs). The $\mu^{84}Sr$ values of enstatite and ordinary chondrites were higher than those of the terrestrial rocks (–24 to –10 ppm) and indistinguishable from that of NIST 987. In contrast to the NCs, the CCs displayed variable $\mu^{84}Sr$ values (dynamic method: –11 to +67 ppm; multistatic method: –19 to +61 ppm).

5.3.2 Nd isotope measurements

In this study, we newly determined Nd isotopic compositions of four bulk meteorites (Y-691, EH3; Y-980223, EH6; Orgueil, CI; Kainsaz, CO3) and two terrestrial basalts (JB-1a and JB-3). The terrestrial sample (JB-3), digested by two distinct procedures, showed indistinguishable Nd isotopic ratios ($\mu^{142}Nd$, $\mu^{145}Nd$, $\mu^{148}Nd$, and $\mu^{150}Nd$ values). Kainsaz (CO3) had indistinguishable Nd isotopic composition from that of the same type of the CC (DaG 190, CO3) reported in Fukai and Yokoyama (2017).

5.3.3 Concentrations of trace elements

We determined the concentrations of trace elements including Rb, Sr, Nd, and Sm for bulk aliquots of chondrite samples. The meteorites measured here generally had uniform $^{147}Sm/^{144}Nd$ ratios (0.19–0.21) that are identical to the chondritic value (0.196; Bouvier et al., 2008) within analytical uncertainties (Table 5.3). In contrast, $^{87}Rb/^{86}Sr$ ratios of these meteorites varied significantly, ranging from 0.01 to 1.36 (Table 5.2). Similarly, Sr concentrations of these meteorites range from 7.8 to 470 ppm.

5.4 Discussion

As shown in Fig. 5.1, the $\mu^{84}Sr$ results obtained by the dynamic and multistatic methods are consistent with each other for all types of the terrestrial basalts, non-carbonaceous meteorites (NCs), and carbonaceous chondrites (CCs). For this reason, the isotopic deviation of meteorites and terrestrial rocks from the standard ($\mu^{84}Sr$, $\mu^{142}Nd$, $\mu^{148}Nd$, and $\mu^{150}Nd$ values) obtained by the dynamic method were used in the following discussion. The uncertainties of mean $\mu^{84}Sr$ and $\mu^{i}Nd$ values for a certain meteorite group (e.g., ordinary chondrites) are represented by the two standard deviations (2 SDs) unless noted otherwise.

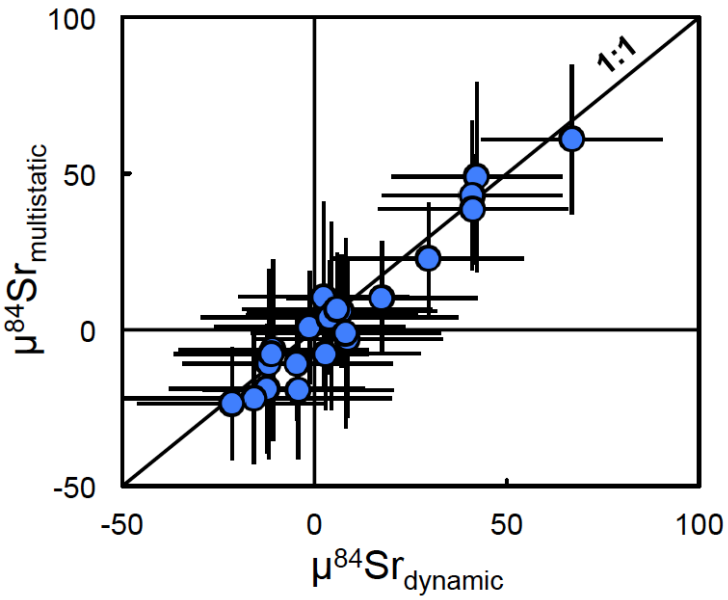

Fig. 5.1 *Diagram of $\mu^{84}Sr$ values for meteorite and terrestrial samples measured by the multistatic and dynamic methods. See the text in Section 5.3 and Tables 5.2–5.3 for error bars. Bold line represents 1:1 line passing the origin.*

5.4.1 Effect of terrestrial weathering to Sr isotopic measurements

The alteration of meteorites due to terrestrial weathering is problematic for isotopic measurements of meteorites except for samples classified into witness fall-types. Fluid-mobile trace elements such as Sr, Ba, and U are especially susceptible to terrestrial weathering occurring in hot deserts (e.g., Crozaz et al., 2003). In fact, the abundances of Sr in the majority of the desert meteorites measured in this study (DaG 190, DaG 412, Dho 1432, Jbilet Winselwan, NWA 753, NWA 4814, and SaU 290) are higher than those in fall meteorites (Fig. 5.2). In Fig. 5.2, the desert meteorites can be discriminated from the fall and Antarctic meteorites by the concentrations of Sr and Ba. This would be resulted by the addition of Sr and Ba into cation sites of constituent silicate minerals and/or into shock-induced cracks and veins. For this reason, the seven desert samples noted above are excluded from the following discussion. In contrast, the Sr concentration of SAH 97072 (9.5 ppm) was relatively low, not showing clear evidence for the addition of terrestrial Sr (Fig. 5.2), so that this meteorite is included in the following discussion. It should be noted that find meteorites on Antarctica measured in this study (Y-980115, Y-980223, and A-882039) did not show elevated abundances of fluid-mobile elements.

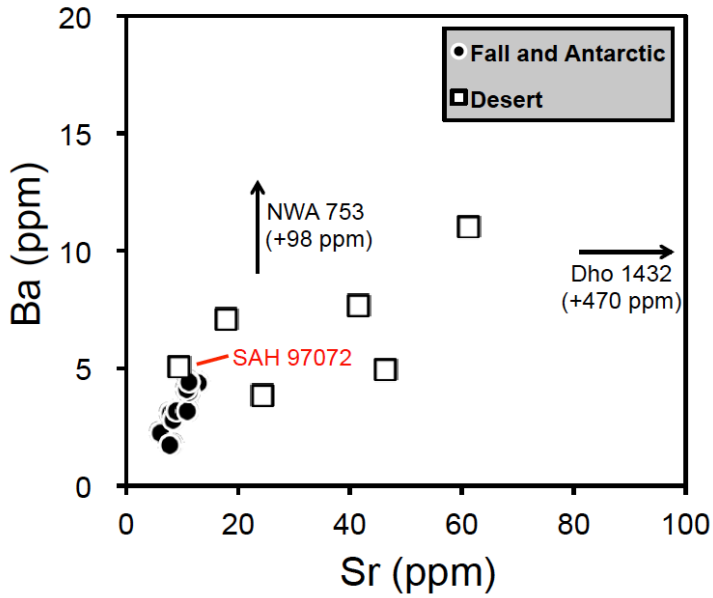

Fig. 5.2 *Diagram for Ba versus Sr concentrations (in ppm) for fall, Antarctic, and desert meteorites.*

5.4.2 Effect of acid digestion for presolar-grain-bearing samples

Different classes of CCs measured in this study (CI, CM, CO, and CV) displayed variable μ^{84}Sr values exceeding analytical uncertainties. It is noteworthy that all of the CCs measured here contain acid-resistant presolar grains such as silicon carbide. Yokoyama et al. (2015) determined the μ^{84}Sr values by TIMS with the static method for bulk aliquots of Allende (CV3; 58 ± 30 ppm) and Murchison (CM2; 52 ± 35 ppm) that were dissolved by the same aggressive sample digestion procedure as we performed in this study. The results for the isotopic measurements of Allende (67 ± 24 ppm) and Murchison (39 ± 24 ppm) with the dynamic method in this study were consistent with those in Yokoyama et al. (2015) within analytical uncertainties.

In this study, we newly provide the μ^{84}Sr values for CI and CO chondrites that

were dissolved by aggressive sample digestion procedure. The $\mu^{84}Sr$ values of Y-980115 (CI; 18 ± 25 ppm) and Orgueil (CI; –1.3 ± 25 ppm) were lower than the data of Orgueil (42 ± 31 ppm) and Ivuna (CI; 37 ± 30 ppm) reported in previous studies (Moynier et al., 2012; Paton et al., 2013). We consider that this inconsistency would be caused by the incomplete acid digestion for CI chondrites in previous studies. To assess the contribution of undissolved acid-resistant presolar grains, we determined the $\mu^{84}Sr$ value of presolar SiC-subtracted CI chondrite (Orgueil) by the mass-balance calculation in which we assumed $\mu^{84}Sr$ = –800,000 ppm for presolar SiC (Liu et al., 2015), 34 ppm for the abundance of presolar SiC in Orgueil (Davidson et al., 2014), and 5 ppm for Sr concentration in presolar SiC (Amari et al., 1995). This calculation resulted in $\mu^{84}Sr$ = +214 ppm for presolar-SiC-subtracted Orgueil, suggesting that ~80% of presolar SiC grains were dissolved in the analyses of CI chondrites in the previous study. In contrast to CI chondrites, Kainsaz (CO3) showed indistinguishable $\mu^{84}Sr$ value (42 ± 24 ppm) from that of Ornans (CO3; 41 ± 31 ppm) measured in the previous study (Moynier et al., 2012). This is attributed to the small abundance of presolar SiC in CO chondrites, likely less than 5 ppm, due to the thermal metamorphism on the CO chondrite parent body(ies).

5.4.3 Correlation in Sr and Nd isotope anomalies

To discuss the origin of nucleosynthetic Sr isotopic heterogeneities, the direct comparison of Sr isotope data with the other isotopic systems is specifically important. Here we first report the multiple isotopic data from the same sample aliquots including

high-precision Sr isotope measurements for the bulk meteorites with complete sample digestion. We plot the μ^{84}Sr value against the Nd isotopic ratios (μ^{148}Nd and μ^{150}Nd values) for the terrestrial rocks, enstatite, ordinary, and CCs in Figs. 5.3 and 5.4.

5.4.3.1 NCs

As shown in Fig. 5.3, NCs are characterized by excesses in μ^{84}Sr values as well as in μ^{148}Nd and μ^{150}Nd values relative to the terrestrial basalts. To deduce the carrier phases inducing the observed nucleosynthetic Sr and Nd isotopic anomalies in NCs, we performed mixing calculations between the terrestrial component and possible presolar components. As for the presolar end-member component, some previous studies (e.g., Dauphas et al., 2004; Yokoyama et al., 2010; Fukai and Yokoyama, 2017) have applied the pure *s*-process isotopic compositions of Mo, Ru, Nd, and Os in the mixing calculation, which were theoretically determined by assuming the main *s*-process occurring in AGB stars (e.g., Arlandini et al., 1999). In the case of Sr, however, theoretical of *s*-process isotopic composition is difficult to determine because ^{86}Sr, ^{87}Sr, and ^{88}Sr are synthesized not only by the main *s*-process but also by the weak *s*-process occurring in the hydrostatic evolutional phases of massive stars of which the actual contribution to the Solar System Sr is poorly constrained (40–60% for ^{86}Sr; Bisterzo et al., 2015). For this reason, we used the observed Sr and Nd isotopic compositions in the acid residual phases of the presolar grain-bearing meteorite Murchison (Qin et al., 2011b) as for the *s*-process component. As shown in Fig. 5.3, Sr and Nd isotopic data for NCs are generally plotted on the *s*-process mixing line. This result suggests that the

Sr and Nd isotopic anomalies of NCs were caused by the depletion of *s*-process enriched materials compared to the terrestrial rocks. Similarly, NCs showed an *s*-process-depleted trend in the μ^{i}Mo–μ^{i}Nd diagram (Render et al., 2017).

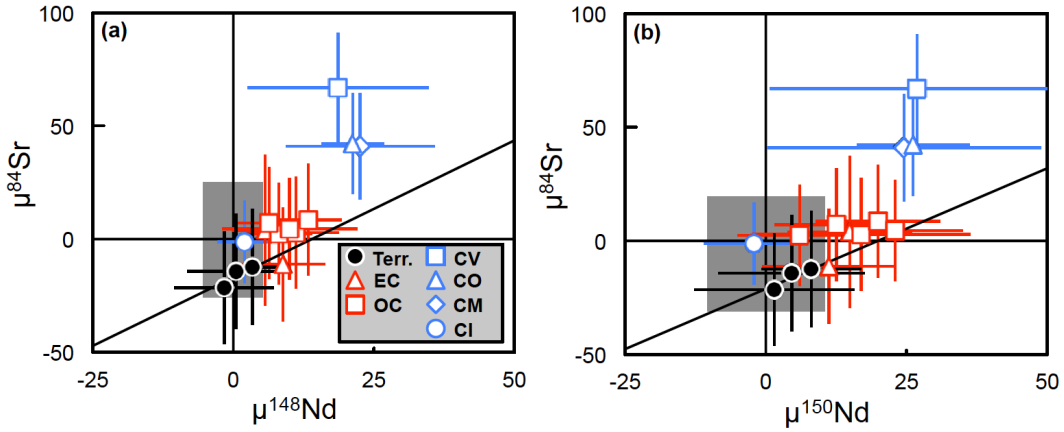

Fig. 5.3 *Diagrams of μ^{84}Sr versus (a) μ^{148}Nd and (b) μ^{150}Nd values plotting the data for terrestrial rocks, enstatite, ordinary, and CCs measured in this study. See the text in Section 5.3 and Tables 5.2 and 5.3 for error bars. Gray zones represent uncertainties of the terrestrial standards (2 SDs; NIST 987 for Sr, JNdi-1 for Nd). Bold lines are mixing lines between the s-process enriched component (Qin et al., 2011b) and terrestrial rocks.*

5.4.3.2 CCs

In contrast to the NCs, bulk aliquots of CM, CO, and CV chondrites show a positive μ^{84}Sr shift from the mixing line of *s*-process end-member and terrestrial rocks (Fig. 5.3). This result suggests that the bulk CCs do not plot on a single linear correlation where the NCs are plotted. In other words, this result points to the "isotopic dichotomy" between NCs and CCs in the diagrams of μ^{84}Sr versus μ^{148}Nd and μ^{84}Sr

versus μ^{150}Nd.

The cause for the nucleosynthetic isotopic dichotomy observed in various types of bulk meteorites has been discussed in previous studies (e.g., Budde et al., 2016; Worsham et al., 2017; Fukai and Yokoyama, 2017). One of the plausible causes for the isotopic dichotomy is the incorporation of CAIs in CCs. To assess this hypothesis, we performed a mass-balance calculation to determine the isotopic compositions of CCs excluding the composition of CAIs (CAI-subtracted CCs). As for the isotopic compositions for CAIs, Myojo et al. (2018) suggested that individual types of CAIs (type-A, type-B, and fine-grained spinel rich inclusions) possess different μ^{84}Sr compositions. The mass-balance calculation would be difficult if we assume that the isotopic compositions of CAI were variable, however, we consider that type-B CAIs represent the mean isotopic compositions for Sr and Nd across different types of CAIs because the isotopic compositions of type-B CAIs have been presumably homogenized via the melting of precursor minerals. We thus assume that CAIs contained in all types of CCs possess uniform Sr and Nd isotopic compositions reported in Brennecka et al. (2013) who performed multiple isotopic measurements for the same aliquots of CAIs. In addition, we assume uniform Sr and Nd concentrations in CAIs (Sr: 67 ppm, Hans et al., 2013; Nd: 9.1 ppm, Marks et al., 2014). In contrast, the abundances of CAIs in chondrites are not uniform across different types of CCs (CV: 2.98 %, CM: 1.21 %, CO: 0.99 %, CI: 0 %; Hezel et al., 2008). The Sr and Nd concentrations in individual bulk CC samples were determined by ICP-MS measurements, and the results for mass-balance calculations are listed in Table 5.5.

Table 5.5 *Parameters and the results of mass-balance calculations for carbonaceous chondrites.*

	CAI abundance (vol. %) (1)	Sr conc. (ppm)	Nd conc. (ppm)	$\mu^{84}Sr$	$\mu^{142}Nd$	$\mu^{148}Nd$	$\mu^{150}Nd$
CAI (2)		67 (3)	9.1 (4)	126 ± 14	–10 ± 4.5	–29 ± 5.4	–64 ± 11
$Murchison_{calc.}$	1.21	7.9	0.64	32 ± 10	–35 ± 5.0	34 ± 8.0	43 ± 15
$Kainsaz_{calc.}$	0.99	11	0.72	46 ± 19	–39 ± 5.0	29 ± 5.3	43 ± 10
$Allende_{calc.}$	2.98	13	0.89	59 ± 15	–41 ± 6.0	37 ± 13	65 ± 19

Uncertainties for Sr and Nd isotopic compositions (2 SEs) were derived by propagating the analytical errors of the isotopic measurements for CAIs.

References. *(1) Hezel et al., 2008; (2) Brennecka et al., 2013; (3) Hans et al., 2013; (4) Marks et al., 2014*

Consequently, the plots of CCs without CAIs show a positive trend in the $\mu^{84}Sr$ versus $\mu^{148}Nd$ and $\mu^{84}Sr$ versus $\mu^{150}Nd$ diagrams (Fig. 5.4). Although the parameters used in the mass-balance calculation contain some uncertainties that cannot be neglected (e.g., isotopic compositions of CAIs, Sr and Nd concentrations of CAIs, and modal abundances of CAIs), the data of CAI-subtracted CCs are generally plotted on the *s*-process mixing line. This result derives two important conclusions: (i) the major source of the isotopic dichotomy between NCs and CCs for Sr and Nd isotopes is CAIs, and (ii) the Sr and Nd isotopic heterogeneities in NCs and CAI-subtracted CCs were resulted by heterogeneous distribution of the *s*-process enriched materials in the early Solar System. These arguments are rationalized by the observation that different classes of CCs without CAIs are plotted on the mixing line in the $\mu^{142}Nd$ versus $\mu^{148}Nd$ and $\mu^{142}Nd$ versus $\mu^{150}Nd$ diagrams (Fukai and Yokoyama, 2017).

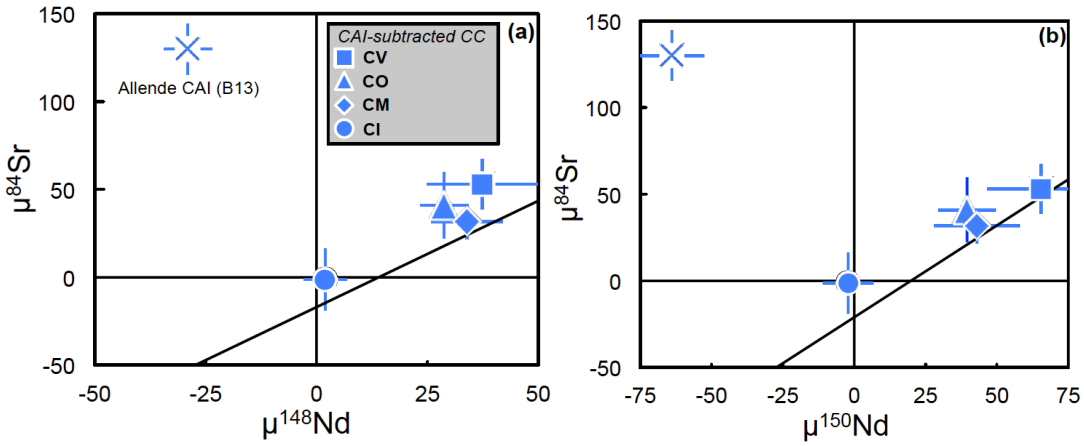

Fig. 5.4 *Diagrams of $\mu^{84}Sr$ versus (a) $\mu^{148}Nd$ and (b) $\mu^{150}Nd$ values plotting the data for CAI subtracted-carbonaceous chondrites. Error bars represent uncertainties (2 SEs) derived by propagating the analytical errors from Sr and Nd isotopic measurements on CAIs. Crosses are data for CAIs with analytical errors (2 SEs) obtained in the previous study (Brennecka et al., 2013).*

5.4.4 Nebular thermal processing and dust transportation

The variable Sr isotopic compositions across different chondrite groups and the linear correlation between Sr and Nd isotopic compositions for the NCs and CAI-subtracted CCs suggest that the early Solar System was not completely homogenized regarding Sr and Nd isotopes. Several scenarios have been proposed to explain the origin of planetary-scale isotopic heterogeneity for various heavy elements observed in bulk aliquots of meteorites and their components (overviewed in Dauphas and Schauble, 2016; Yokoyama and Walker, 2016).

The traditional model to explain the isotopic heterogeneity is that the homogenization of the molecular cloud and / or solar nebula was not complete before

the planetesimal formation (e.g., Dauphas et al., 2002). If the mixing of the solar nebula have not attained the isotopic homogeneity, however, nucleosynthetic isotopic anomalies would not form the correlation along the heliocentric distance (Earth–NC–CC). This model is also difficult to explain the variable degree of nucleosynthetic isotope anomalies among trans-iron elements.

Alternatively, a scenario regarding the late injection of presolar material from core-collapse supernovae (ccSNe) to isotopically homogeneous solar nebula has been proposed. The late injection model was mainly inferred from the evidence for heterogeneous distribution of short-lived nuclides (e.g., ^{26}Al: Boss, 2004). This model also could account for the Cr isotopic heterogeneity among bulk meteorites, induced by the injection for Cr-rich nanospinel formed via ccSNe (e.g., Dauphas et al., 2010; Qin et al., 2011a). Generally, *r*-process nuclides of some trans-iron elements are synthesized in the extremely neutron-rich environment of a ccSN. However, recent theoretical and observational studies suggest that ccSNe should not synthesize *r*-process nuclides with mass numbers (A) greater than ~110–130 (e.g., Fischer et al., 2010; Wanajo et al., 2013; Tsujimoto and Shigeyama, 2014). If this were the case, the late injection of supernovae materials would not have altered the isotopic compositions of *r*-process nuclides of Nd for the Earth and chondrites.

One of the plausible scenarios accounting for the isotopic heterogeneity in the early Solar System is the nebular thermal processing model, first suggested by Trinquier et al. (2009) to explain the Ti and Cr isotopic compositions of various types of bulk meteorites and chondritic components. In this model, the Solar System is assumed to be

initially homogeneous regarding Ti and Cr isotope compositions. Subsequently, presolar dust grains presented in the early Solar System were evaporated by nebular thermal processing and then incorporated into the gas reservoir. After the separation of gas phase and residual dusts, the gas phase was condensed to CAIs (and amoeboid olivine aggregates) that acquired the isotopic compositions of the evaporated presolar materials. This model was applied to explain the variation of Sr isotopic compositions in meteorites in previous studies (Paton et al., 2013; Yokoyama et al., 2015; Myojo et al., 2018).

However, the positive Sr–Nd correlation observed in the NCs and CAI-subtracted CCs (Figs. 5.3 and 5.4), as well as the Sr and Nd isotopic variations within the CAI-subtracted CCs, cannot be explained by the above-mentioned model. This is because that CAI shows an *s*-process-enriched signature for Nd isotopes (Brennecka et al., 2013; Burkhardt et al., 2016), whereas the gas phase evaporated through the nebular thermal processing should possess an *s*-process-deficit signature. In addition, nebular thermal processing could not explain the isotopic variation among CCs, because this process was assumed to occur solely in the inner Solar System.

Instead, we propose a new disk evolutionary model that accounts for the correlated nucleosynthetic isotope anomalies between Sr and Nd (Fig. 5.5). First, we assume an isotopically homogeneous molecular cloud core and early solar nebula. We consider two carrier dust grains for Sr and Nd existed in the early Solar System, based on the leaching experiments for CCs (Qin et al., 2011b; Paton et al., 2013; Yokoyama et al., 2015). One plausible carrier grain is mainstream presolar SiC that possessed

s-process enriched isotopic compositions. The residual phases for leached CCs most likely represent the isotopic compositions of presolar SiC, because these grains are highly acid-resistant. In addition, to explain the bulk Sr and Nd isotopic compositions for CAI-subtracted CCs, we need another single *s*-process depleted carrier grain. We consider that the carrier phase of positive $\mu^{84}Sr$, $\mu^{148}Nd$ and $\mu^{150}Nd$ values is not an intact presolar grain but would be dust grains that have experienced multiple physical processes including evaporation, mixing, and recondensation in the solar nebula and/or molecular cloud. Such grains, called "recycled silicates" were widespread in the solar nebula as a result of grain circulation that was triggered most likely by the turbulent diffusion (Morbidelli et al., 2016). Because most of the presolar SiC grains have condensed at ~1600 K (Lodders and Fegley, 1995) in AGB stars, SiC grains would be more refractory compared to the recycled silicates. By the progressive heating in the inner Solar System, recycled silicates would have been destroyed selectively. As the nebular temperature is expected to decrease along with the heliocentric distance, Earth has been accreted from the most thermally-processed (i.e., *s*-process rich) materials, while the parent bodies of CCs has been accreted from the least-processed (i.e., *s*-process depleted) materials that represent the mean Sr and Nd isotopic compositions in the early Solar System. This scenario explains the observed isotopic variation across the Earth, NCs parent bodies, and CAI-subtracted CCs parent bodies.

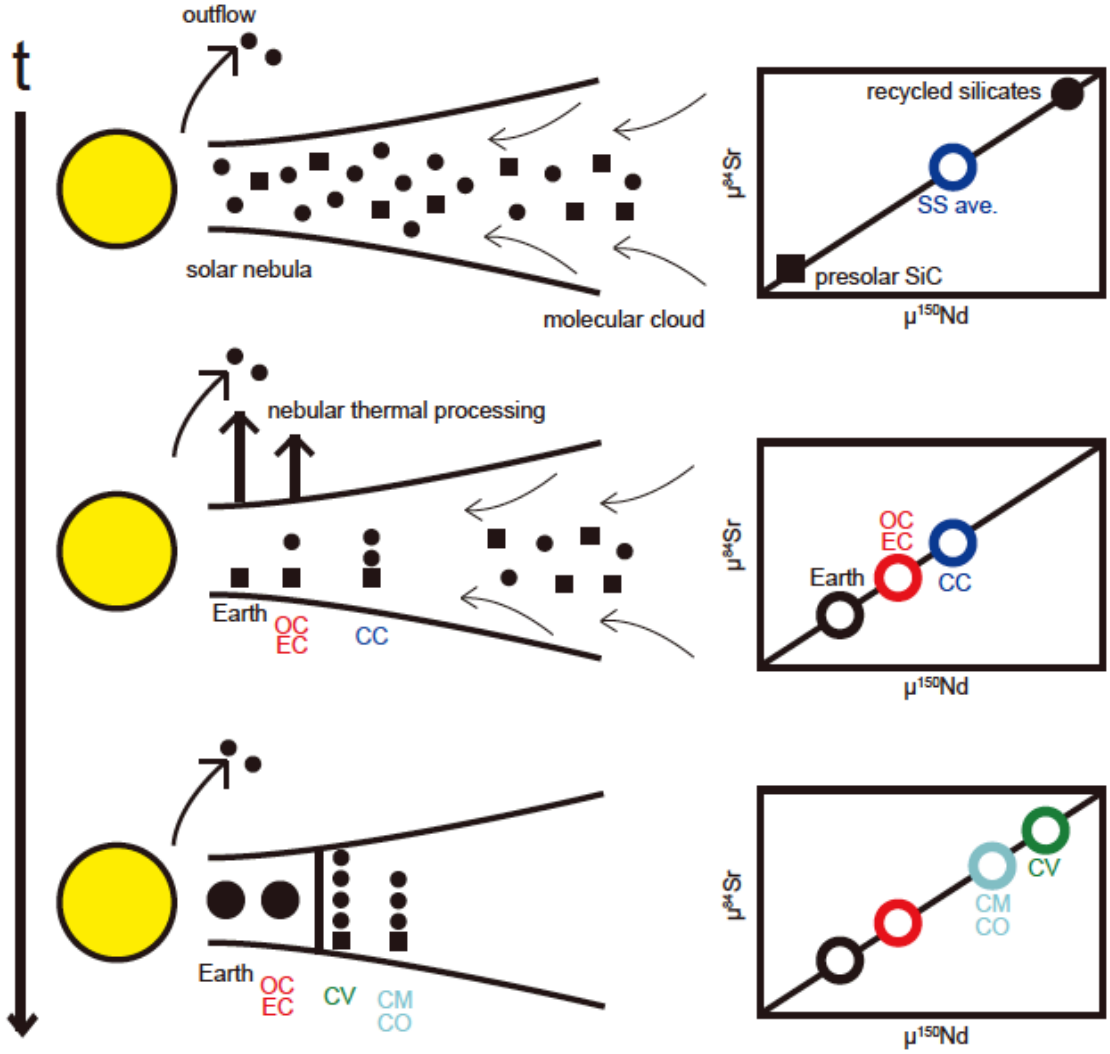

Fig. 5.5 *Schematic image of disk evolution associated with nebular thermal processing and dust transportation including the $\mu^{84}Sr$ versus $\mu^{150}Nd$ diagrams Initially, the solar nebula was isotopically homogeneous and consisted of recycled silicates and presolar SiC. Subsequently, nebular thermal processing occurred in the inner Solar System, inducing the isotopic heterogeneities among Earth, NC parent bodies, and CAI-subtracted CC parent bodies. Finally, the pressure bump by the mass of Jupiter core concentrated the recycled silicates mostly in the formation region of CV chondrite parent bodies.*

As the temperature of the solar nebula decreased, the nebular thermal processing

has terminated. On the other hand, recycled silicates continued to circulate throughout the solar nebula. The isotopic reservoirs of NCs and CCs have been separated, possibly due to the presence of Jupiter core that formed by ~1 Myr after CAI condensation (Kruijer et al., 2017). If this is the case, mm-scale relatively large dusts should be concentrated at the outside of Jupiter, because the pressure bump by the mass of Jupiter core concentrated the drifting dusts. Consequently, the parent bodies of CCs should have acquired growing (mm-scale) recycled silicates that are depleted in the *s*-process isotopes whereas μm-scale intact presolar grains enriched in the *s*-process isotopes were coupled to gas phase. This heterogeneous incorporation of recycled silicates accounts for the isotopic variation between CAI-subtracted CV chondrites and CM-CO chondrites, assuming that CV parent bodies were located closer to the Sun than CM-CO parent bodies. The transportation and concentration in CC formation regions of relatively large dusts (~2.5 mm) were assessed by the numerical calculation (Desch et al., 2018).

This model also explains homogeneous Os isotopic compositions of various types of bulk scale meteorites (Yokoyama et al., 2007). Because 50% condensation temperature of Os is ~1800 K (Lodders, 2003), Os isotopes would have avoided evaporating into the gas phase. Therefore, Os isotopic homogeneity has been preserved throughout the early Solar System so that the nebular thermal processing did not disturb Os isotopic compositions in NCs and CCs.

5.4.5 Isotopic anomalies of CI chondrites

Fig. 5.6 shows the Nd isotopic compositions of NCs and CAI-subtracted CCs in the $\mu^{142}Nd$–$\mu^{148}Nd$ and $\mu^{142}Nd$–$\mu^{150}Nd$ diagrams. As shown in this figure, the Nd isotopic anomalies of CAI-subtracted CV, CM, and CO chondrites can be explained by the heterogeneous distribution of the *s*-process enriched material. However, Orgueil (CI) shows an offset towards the lower side of y-axis ($\mu^{142}Nd$) from the *s*-process mixing lines in the $\mu^{142}Nd$–$\mu^{148}Nd$ and $\mu^{142}Nd$–$\mu^{150}Nd$ diagrams. The $\mu^{142}Nd$ values of meteorites can change along with the variable contribution of *s*- and *p*-process nuclides. In addition to this, the variation of $\mu^{142}Nd$ values can be explained by the fractionation of Sm and Nd that occurred in the early stage of the Solar System when the now-extinct nuclide of ^{146}Sm (half-life: 103 Myr) was alive. In the case of Orgueil, however, the Sm–Nd fractionation does not account for the offset from the *s*-process versus terrestrial mixing line because this meteorite is a CI chondrite that has a canonical Sm/Nd ratio of 0.20 ± 0.06, which is identical to those of the other unequilibrated primitive chondrites (0.196; Bouvier et al., 2008). Therefore, this offset suggests that the CI chondrite possesses a *p*-process-depleted composition compared not only to the terrestrial rocks, but also to NCs and the other types of CAI-subtracted CCs.

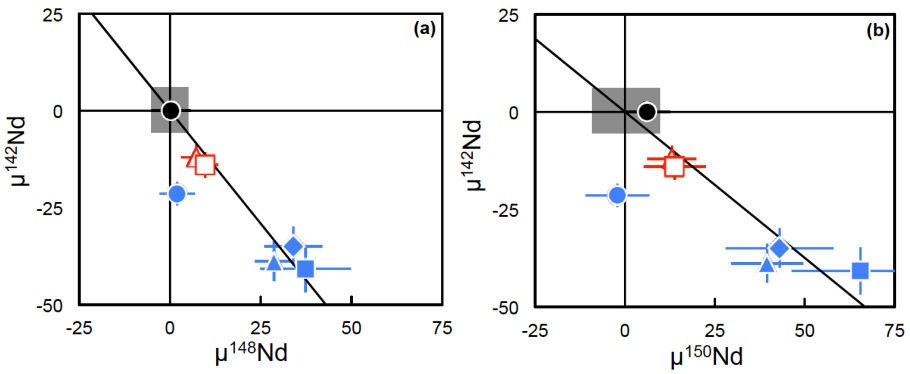

Fig. 5.6 *Diagrams of (a) μ^{142}Nd versus μ^{148}Nd and (b) μ^{142}Nd versus μ^{150}Nd values for terrestrial rocks, enstatite, ordinary, and carbonaceous chondrites. Symbols, gray zones, error bars, and bold lines are the same as in Figs. 5.3–5.4. The μ^{142}Nd values for meteorite samples are corrected for radiogenic ^{142}Nd variations to a common chondritic value of ^{143}Nd/^{144}Nd = 0.512630 (Bouvier et al., 2008).*

On the other hand, the data points of CI chondrite do not show any *p*-process depleted signature in the μ^{84}Sr–$\mu^{148,150}$Nd diagrams (Figs. 5.3–5.4). This result seems to be inconsistent with the deficit of *p*-process Nd isotopes (i.e., ^{142}Nd) as deduced from the μ^{142}Nd–μ^{148}Nd and μ^{142}Nd–μ^{150}Nd diagrams. However, it has been argued that the nucleosynthetic origins for *p*-nuclides of Sr and Nd are decoupled; recent model calculations suggested that the light *p*-process nuclides including ^{84}Sr were dominantly synthesized by the α-rich freeze out during core-collapse supernovae, whereas heavier nuclides including ^{142}Nd were dominantly synthesized via γ-process in Type Ia supernovae (Lugaro et al., 2016). The reason for the different behavior regarding the *p*-nuclides between the CI chondrite and the other types of CCs is still uncertain. Because CI chondrites possess most abundant matrix components in CCs (Scott and Krot, 2014), the parent bodies of CI chondrites were likely formed in the outer region of the Solar System compared to the CV-CM-CO parent bodies. The outer region of the solar nebula may be more affected by the injection of supernovae materials and/or input from molecular cloud compared to the inner region. To reveal the cause for the isotopic heterogeneity among CCs, further investigation for the isotope anomalies of *p*-process nuclides is needed.

5.5 Conclusion

We conducted high-precision Sr and Nd isotopic analyses on bulk aliquots of enstatite, ordinary, and carbonaceous chondrites by applying a high-pressure and high-temperature digestion technique to achieve complete dissolution of acid-resistant presolar grains. From the results of this study, we reached the following four conclusions:

- Enstatite and ordinary chondrites possess small, but resolvable isotopic shifts of μ^{84}Sr values from the terrestrial rocks. In μ^{84}Sr versus μ^{148}Nd and μ^{84}Sr versus μ^{150}Nd diagrams, these samples are plotted on the mixing line of *s*-process endmember and terrestrial rocks. The Sr and Nd isotopic anomalies observed in enstatite and ordinary chondrites were caused by the heterogeneous distribution of *s*-process enriched materials in the early Solar System.
- Carbonaceous chondrites (CCs) display variable μ^{84}Sr values (–1.3 to +67 ppm). These meteorites are not plotted on the *s*-process versus terrestrial mixing line in the Sr–Nd diagrams. However, the Sr and Nd isotopic compositions of CAI subtracted-CCs, determined by the mass-balance calculation, are generally plotted on the *s*-process mixing line. This observation suggests that Sr and Nd isotopic dichotomy observed between NCs (enstatite and ordinary chondrites) and CCs was caused by the incorporation of CAIs into the location where parent bodies of CCs were formed.
- The Sr and Nd isotopic heterogeneities among terrestrial rocks, NCs, and CAI-subtracted CCs were likely caused by the nebular thermal processing. This

process could selectively destroy the recycled silicates possessing *s*-process depleted signature in the inner Solar System. The Sr and Nd isotopic heterogeneities among each class of CAI-subtracted CCs (CM, CO, and CV) were likely caused by the non-uniform incorporation of recycled silicates that were concentrated in the CC formation region due to the formation of pressure bump by Jupiter core.

- Orgueil (CI) shows an offset towards the lower side of y-axis (μ^{142}Nd) from the *s*-process mixing lines in the μ^{142}Nd–μ^{148}Nd and μ^{142}Nd–μ^{150}Nd diagrams. This observation implies that CI chondrites have *p*-deficit Nd isotope anomalies whereas these meteorites do not show any *p*-deficit signature in Sr isotopes. The isotopic compositions for CI chondrites are not explained by our disk evolutionary model, most likely due to the injection of supernovae materials and/or input of materials from the molecular cloud.

References

Amari, S., Hoppe, P., Zinner, E., Lewis, R.S., 1995. Trace-element concentrations in single circumstellar silicon-carbide grains from the Murchison meteorite. Meteoritics 30, 679-693.

Andreasen, R., Sharma, M., 2007. Mixing and homogenization in the early solar system: Clues from Sr, Ba, Nd, and Sm isotopes in meteorites. Astrophysical Journal 665, 874-883.

Arlandini, C., Kappeler, F., Wisshak, K., Gallino, R., Lugaro, M., Busso, M., Straniero, O., 1999. Neutron capture in low-mass asymptotic giant branch stars: Cross sections and abundance signatures. Astrophysical Journal 525, 886-900.

Bermingham, K.R., Mezger, K., Scherer, E.E., Horan, M.F., Carlson, R.W., Upadhyay, D., Magna, T., Pack, A., 2016. Barium isotope abundances in meteorites and their implications for early Solar System evolution. Geochimica et Cosmochimica Acta 175, 282-298.

Bisterzo, S., Gallino, R., Kappeler, F., Wiescher, M., Imbriani, G., Straniero, O., Cristallo, S., Gorres, J., deBoer, R.J., 2015. The branchings of the main s-process: their sensitivity to alpha-induced reactions on ^{13}C and ^{22}Ne and to the uncertainties of the nuclear network. Monthly Notices of the Royal Astronomical Society 449, 506-527.

Bouvier, A., Vervoort, J.D., Patchett, P.J., 2008. The Lu-Hf and Sm-Nd isotopic composition of CHUR: Constraints from unequilibrated chondrites and

implications for the bulk composition of terrestrial planets. Earth and Planetary Science Letters 273, 48-57.

Boss, A.P., 2004. Evolution of the solar nebula. VI. Mixing and transport of isotopic heterogeneity. Astrophysical Journal 616, 1265-1277.

Brennecka, G.A., Borg, L.E., Wadhwa, M., 2013. Evidence for supernova injection into the solar nebula and the decoupling of r-process nucleosynthesis. Proceedings of the National Academy of Sciences of the United States of America 110, 17241-17246.

Budde, G., Burkhardt, C., Brennecka, G.A., Fischer-Gödde, M., Kruijer, T.S., Kleine, T., 2016. Molybdenum isotopic evidence for the origin of chondrules and a distinct genetic heritage of carbonaceous and non-carbonaceous meteorites. Earth and Planetary Science Letters 454, 293-303.

Burkhardt, C., Borg, L.E., Brennecka, G.A., Shollenberger, Q.R., Dauphas, N., Kleine, T., 2016. A nucleosynthetic origin for the Earth's anomalous ^{142}Nd composition. Nature 537, 394-398.

Crozaz, G., Floss, C., Wadhwa, M., 2003. Chemical alteration and REE mobilization in meteorites from hot and cold deserts. Geochimica et Cosmochimica Acta 67, 4727-4741.

Dauphas, N., Marty, B., Reisberg, L., 2002. Molybdenum evidence for inherited planetary scale isotope heterogeneity of the protosolar nebula. Astrophysical Journal 565, 640-644.

Dauphas, N., Davis, A.M., Marty, B., Reisberg, L., 2004. The cosmic molybdenum-ruthenium isotope correlation. Earth and Planetary Science Letters 226, 465-475.

Dauphas, N., Remusat, L., Chen, J.H., Roskosz, M., Papanastassiou, D.A., Stodolna, J., Guan, Y., Ma, C., Eiler, J.M., 2010. Neutron-rich chromium isotope anomalies in supernova nanoparticles. Astrophysical Journal 720, 1577-1591.

Dauphas, N., Schauble, E.A., 2016. Mass Fractionation Laws, Mass-Independent Effects, and Isotopic Anomalies. Annual Review of Earth and Planetary Sciences 44, 709-783.

Davidson, J., Busemann, H., Nittler, L.R., Alexander, C.M.O., Orthous-Daunay, F.R., Franchi, I.A., Hoppe, P., 2014. Abundances of presolar silicon carbide grains in primitive meteorites determined by NanoSIMS. Geochimica et Cosmochimica Acta 139, 248-266.

Desch, S.J., Kalyaan, A., Alexander, C.M.O., 2018. The Effect of Jupiter's Formation on the Distribution of Refractory Elements and Inclusions in Meteorites. Astrophysical Journal Supplement Series 238.

Fischer, T., Whitehouse, S.C., Mezzacappa, A., Thielemann, F.K., Liebendorfer, M., 2010. Protoneutron star evolution and the neutrino-driven wind in general relativistic neutrino radiation hydrodynamics simulations. Astronomy & Astrophysics 517.

Fukai, R., Yokoyama, T., 2017. Neodymium isotope heterogeneity of ordinary and carbonaceous chondrites and the origin of non-chondritic ^{142}Nd compositions in the Earth. Earth and Planetary Science Letters 474, 206-214.

Fukai, R., Yokoyama, T., Kagami, S., 2017. Evaluation of the long-term fluctuation in isotope ratios measured by TIMS with the static, dynamic, and multistatic methods: A case study for Nd isotope measurements. International Journal of Mass Spectrometry 414, 1-7.

Garcon, M., Boyet, M., Carlson, R.W., Horan, M.F., Auclair, D., Mock, T.D., 2018. Factors influencing the precision and accuracy of Nd isotope measurements by thermal ionization mass spectrometry. Chemical Geology 476, 493-514.

Hans, U., Kleine, T., Bourdon, B., 2013. Rb-Sr chronology of volatile depletion in differentiated protoplanets: BABI, ADOR and ALL revisited. Earth and Planetary Science Letters 374, 204-214.

Henshall, T., Cook, D.L., Garcon, M., Schonbachler, M., 2018. High-precision strontium isotope analysis of geological samples by thermal ionisation mass spectrometry. Chemical Geology 482, 113-120.

Hezel, D.C., Russell, S.S., Ross, A.J., Kearsley, A.T., 2008. Modal abundances of CAIs: Implications for bulk chondrite element abundances and fractionations. Meteoritics & Planetary Science 43, 1879-1894.

Kagami, S., Yokoyama, T., 2016. Chemical separation of Nd from geological samples for chronological studies using ^{146}Sm–^{142}Nd and ^{147}Sm–^{143}Nd systematics. Analytica Chimica Acta 937, 151-159.

Kruijer, T.S., Burkhardt, C., Budde, G., Kleine, T., 2017. Age of Jupiter inferred from the distinct genetics and formation times of meteorites. Proceedings of the National Academy of Sciences of the United States of America 114, 6712-6716.

Liu, N., Savina, M.R., Gallino, R., Davis, A.M., Bisterzo, S., Gyngard, F., Kappeler, F., Cristallo, S., Dauphas, N., Pellin, M.J., Dillmann, I., 2015. Correlated strontium and barium isotopic compositions of acid-cleaned single mainstream silicon carbides from Murchison. Astrophysical Journal 803.

Lodders, K., 2003. Solar system abundances and condensation temperatures of the elements. Astrophysical Journal 591, 1220-1247.

Lodders, K., Fegley, B., 1995. The origin of circumstellar silicon-carbide grains found in meteorites. Meteoritics 30, 661-678.

Lugaro, M., Pignatari, M., Ott, U., Zuber, K., Travaglio, C., Gyurky, G., Fulop, Z., 2016. Origin of the p-process radionuclides ^{92}Nb and ^{146}Sm in the early solar system and inferences on the birth of the Sun. Proceedings of the National Academy of Sciences of the United States of America 113, 907-912.

Marks, N.E., Borg, L.E., Hutcheon, I.D., Jacobsen, B., Clayton, R.N., 2014. Samarium-neodymium chronology and rubidium-strontium systematics of an Allende calcium-aluminum-rich inclusion with implications for ^{146}Sm half-life. Earth and Planetary Science Letters 405, 15-24.

Morbidelli, A., Bitsch, B., Crida, A., Gounelle, M., Guillot, T., Jacobson, S., Johansen, A., Lambrechts, M., Lega, E., 2016. Fossilized condensation lines in the Solar System protoplanetary disk. Icarus 267, 368-376.

Moynier, F., Day, J.M.D., Okui, W., Yokoyama, T., Bouvier, A., Walker, R.J., Podosek, F.A., 2012. Planetary-scale strontium isotopic heterogeneity and the age of volatile depletion of early solar system materials. Astrophysical Journal 758.

Myojo, K., Yokoyama, T., Okabayashi, S., Wakaki, S., Sugiura, N., Iwamori, H., 2018. The origin and evolution of nucleosynthetic Sr isotope variability in Calcium and Aluminum-rich refractory inclusions. Astrophysical Journal 853.

Paton, C., Schiller, M., Bizzarro, M., 2013. Identification of an ^{84}Sr-depleted carrier in primitive meteorites and implications for thermal processing in the solar protoplanetary disk. Astrophysical Journal Letters 763.

Poole, G.M., Rehkamper, M., Coles, B.J., Goldberg, T., Smith, C.L., 2017. Nucleosynthetic molybdenum isotope anomalies in iron meteorites - new evidence for thermal processing of solar nebula material. Earth and Planetary Science Letters 473, 215-226.

Qin, L., Nittler, L.R., Alexander, C.M.O., Wang, J., Stadermann, F.J., Carlson, R.W., 2011. Extreme ^{54}Cr-rich nano-oxides in the CI chondrite Orgueil - Implication for a late supernova injection into the solar system. Geochimica Et Cosmochimica Acta 75, 629-644.

Qin, L., Carlson, R.W., Alexander, C.M.O.D., 2011. Correlated nucleosynthetic isotopic variability in Cr, Sr, Ba, Sm, Nd and Hf in Murchison and QUE 97008. Geochimica et Cosmochimica Acta 75, 7806-7828.

Render, J., Fischer-Gödde, M., Burkhardt, C., Kleine, T., 2017. The cosmic molybdenum-neodymium isotope correlation and the building material of the Earth. Geochemical Perspectives Letters 3, 170-178.

Scott, E.R.D., Krot, A.N., 2014. Chondrites and Their components, 2nd edition. Treatise on Geochemistry, 65-137.

Trinquier, A., Elliott, T., Ulfbeck, D., Coath, C., Krot, A.N., Bizzarro, M., 2009. Origin of Nucleosynthetic Isotope Heterogeneity in the Solar Protoplanetary Disk. Science 324, 374-376.

Tsujimoto, T., Shigeyama, T., 2014. Enrichment history of r-process elements shaped by a merger of neutron star pairs. Astronomy & Astrophysics 565.

Wanajo, S., 2013. The r-process in proto-neutron-star wind revisited. Astrophysical Journal Letters 770.

Warren, P.H., 2011. Stable-isotopic anomalies and the accretionary assemblage of the Earth and Mars: A subordinate role for carbonaceous chondrites. Earth and Planetary Science Letters 311, 93-100.

Worsham, E.A., Bermingham, K.R., Walker, R.J., 2017. Characterizing cosmochemical materials with genetic affinities to the Earth: Genetic and chronological diversity within the IAB iron meteorite complex. Earth and Planetary Science Letters 467, 157-166.

Yobregat, E., Fitoussi, C., Bourdon, B., 2017. A new method for TIMS high precision analysis of Ba and Sr isotopes for cosmochemical studies. Journal of Analytical Atomic Spectrometry 32, 1388-1399.

Yokoyama, T., Alexander, C.M.O.D., Walker, R.J., 2010. Osmium isotope anomalies in chondrites: Results for acid residues and related leachates. Earth and Planetary Science Letters 291, 48-59.

Yokoyama, T., Fukami, Y., Okui, W., Ito, N., Yamazaki, H., 2015. Nucleosynthetic strontium isotope anomalies in carbonaceous chondrites. Earth and Planetary Science Letters 416, 46-55.

Yokoyama, T., Nagai, Y., Hinohara, Y., Mori, T., 2017. Investigating the Influence of Non-Spectral Matrix Effects in the Determination of Twenty-Two Trace Elements in Rock Samples by ICP-QMS. Geostandards and Geoanalytical Research 41, 221-242.

Yokoyama, T., Rai, V.K., Alexander, M.O.D., Lewis, R.S., Carlson, R.W., Shirey, S.B., Thiemens, M.H., Walker, R.J., 2007. Osmium isotope evidence for uniform distribution of s- and r-process components in the early solar system. Earth and Planetary Science Letters 259, 567-580.

Yokoyama, T., Walker, R.J., 2016. Nucleosynthetic isotope variations of siderophile and chalcophile elements in the Solar System. Highly siderophile and strongly chalcophile elements in high-temperature geochemistry and cosmochemistry 81, 107-160.

Chapter 6:
Future perspective

In this doctor thesis, we performed Sr and Nd isotopic measurements for various types of bulk chondrites with thermal ionization mass spectrometry (TIMS). We concluded that the Sr and Nd isotopic heterogeneities among terrestrial rocks, non-carbonaceous meteorites and carbonaceous chondrites were likely caused by the nebular thermal processing and dust transportation to carbonaceous chondrites formation region. However, several unsolved problems still remained in our model regarding the physicochemical evolution of the early Solar System. In this chapter, we introduce the future perspective on the issues that have been discussed in the previous chapters of this thesis.

6.1 Samples to investigate

To construct more precise and realistic disk evolutionary model, it is vital to identify the nucleosynthetic isotopic anomalies for various trans-iron elements not only in bulk chondrites, but also in chondritic constituents. The samples that should be measured to this end are carrier phases that possess significantly large isotope anomalies within chondrites; those include presolar grains (compiled in Hoppe and Ott, 1997) and acid leaching/residual phases (e.g., Qin et al., 2011). Previous studies have revealed that the mainstream SiC is the dominant carrier grain of the *s*-process components. In contrast, the information for the carrier phases of *r*-process nuclides has been scarcely obtained. One of the candidates for the *r*-process carrier phases is the grains that derived from core-collapse supernovae (e.g., type-X SiC, low-density graphite, oxide grains). Because the abundances of these grains in chondrites are

relatively low (~1–80 ppm) compared to mainstream SiC (150 ppm), precise isotopic measurements of trans-iron elements for these grains are difficult to achieve at the current level of mass spectrometric techniques (Zinner, 2014).

In addition to mainstream SiC, we proposed that the recycled silicates in the solar nebula should possess *s*-depleted Sr and Nd compositions (Chapter 5). However, any *s*-depleted phases were not found in the sequential acid leaching experiments for Sr and Nd isotopic measurements (Qin et al., 2011; Paton et al., 2013; Boyet and Gannoun, 2013; Yokoyama et al., 2015). The reason for this inconsistency may arise from that the *s*-depleted phases are so tiny that they dissolved simultaneously with the other labile presolar/solar phases in the early leaching steps using relatively weak acids. A potential procedure to detect the *s*-depleted phases in chondrites is the imaging technique by high-resolution mass spectrometers (e.g., NanoSIMS, laser-ablation ICP-MS).

In addition to presolar grains, the isotopic compositions of trans-iron elements in various petrologic types of calcium-and aluminum-rich inclusions (CAIs) are key to understand the isotopic evolution in the early Solar System. In our model, we assumed that type-B CAIs represent the average isotopic compositions for all CAIs included in carbonaceous chondrites (Chapter 5). However, several previous studies reported that fluffy type-A (FTA) CAIs possess distinct isotopic compositions from type-B CAIs (Sr: Myojo et al., 2018; Mo: Burkhardt et al., 2011; W: Kruijer et al., 2014). In addition, chondrules that are enriched in refractory elements possess the nucleosynthetic Ti isotope anomalies that are indistinguishable from CAIs (Gerber et al., 2017). This result indicates that relict CAI-like materials were incorporated into other chondritic

components as a form of chondrules and matrices. Therefore, simultaneous isotopic measurements of various elements for each chondritic component are important to consider the isotopic heterogeneities among CAIs and CAI-like materials.

Furthermore, sample return missions will provide crucial information in planetary sciences. The Hayabusa-2 mission launched by Japan Aerospace Exploration Agency (JAXA) aims to collect μm to mm-size grains (up to ~1 g) from the surface of a C-type asteroid "Ryugu". In addition, the OSIRIS-REx (Origins, Spectral, Interpretation, Resource Identification, Security, Regolith Explorer) project launched by National Aeronautics and Space Administration (NASA) will bring rock samples back from a B-type asteroid "Bennu". In contrast to meteorites, the returned samples possess direct linkage to its parent body, providing information regarding the evolution of orbit and the records of alteration and irradiation by the Solar wind. Most importantly, unlike meteorite samples, the returned samples are not suffered from terrestrial weathering. We consider that the formation region of C-type asteroid can be estimated by the combination of the remote-sensing data and nucleosynthetic isotopic anomalies for trans-iron elements in the returned samples.

6.2 Improvement of mass spectrometry

In order to precisely analyze chemical and isotopic compositions in μm to mm-scale chondritic components and the small amount samples returned from asteroids, mass spectrometric techniques must be further improved. We introduce here the possibilities of the development of mass spectrometry techniques.

In the present TIMS instrument, secondary electron multipliers (SEM) are used to measure small amount samples (< ~1 ng). For example, very small amounts of Os (~50 fg) can be measured at the precision of ~3 % using SEM (Seo et al., 2018). The isotopic measurements with SEM have not been applied to measure nucleosynthetic isotopic anomalies in chondritic constituents, which is considered to be advantageous when measuring small samples with extremely anomalous samples such as presolar grains.

Alternatively, using high-ohmage feedback resistors (10^{12} or 10^{13} Ω) connected to Faraday cups are effective to detect low ion signal with TIMS. However, compared to normal feedback resistor (10^{11} Ω), these resistors have a disadvantage regarding the idle time, which is the time interval required to completely reset the memory of previous ion signal. In general, compared to 10^{10} or 10^{11} Ω resistors, a longer idle time (~30 s) is required for high-ohmage feedback resistors to avoid the effect of incoming ions measured in a former block. If a part of multiple resistors is replaced by high-ohmage resistors, isotopes with relatively small abundances (e.g., ^{84}Sr) can be measured more precisely. In that case, the dynamic-multicollection method cannot be applied, therefore the surface of Faraday cups should be all fresh.

To obtain the information of nucleosynthetic isotopic anomalies from single particles (e.g., presolar grains, interplanetary dusts), high-resolution mass spectrometry is required. In particular, a new-generation Resonance Ionization Mass Spectrometry (RIMS) instrument, Chicago Instrument for Laser Ionization (CHILI) was designed to measure the isotopic compositions of presolar grains at high spatial resolution and high sensitivity (Stephan et al., 2016). CHILI can measure various elements with a wide

mass range including trans-iron elements (e.g., Sr, Zr, Ba), providing direct information for the origin and nucleosynthetic processes of trans-iron elements that occurred in various stellar environments.

References

Boyet, M., Gannoun, A., 2013. Nucleosynthetic Nd isotope anomalies in primitive enstatite chondrites. Geochimica et Cosmochimica Acta 121, 652-666.

Burkhardt, C., Kleine, T., Oberli, F., Pack, A., Bourdon, B., Wieler, R., 2011. Molybdenum isotope anomalies in meteorites: Constraints on solar nebula evolution and origin of the Earth. Earth and Planetary Science Letters 312, 390-400.

Gerber, S., Burkhardt, C., Budde, G., Metzler, K., Kleine, T., 2017. Mixing and Transport of Dust in the Early Solar Nebula as Inferred from Titanium Isotope Variations among Chondrules. Astrophysical Journal Letters 841.

Hoppe, P., Ott, U., 1996. Mainstream silicon carbide grains from meteorites, International Conference on Astrophysical Implications of the Laboratory Study of Presolar Materials, Washington Univ., Steinberg Gallery, St Louis, Mo, 27-58.

Kruijer, T.S., Kleine, T., Fischer-Gödde, M., Burkhardt, C., Wieler, R., 2014. Nucleosynthetic W isotope anomalies and the Hf-W chronometry of Ca-Al-rich inclusions. Earth and Planetary Science Letters 403, 317-327.

Myojo, K., Yokoyama, T., Okabayashi, S., Wakaki, S., Sugiura, N., Iwamori, H., 2018. The origin and evolution of nucleosynthetic Sr isotope variability in Calcium and Aluminum-rich refractory inclusions. Astrophysical Journal 853.

Paton, C., Schiller, M., Bizzarro, M., 2013. Identification of an ^{84}Sr-depleted carrier in primitive meteorites and implications for thermal processing in the solar protoplanetary disk. Astrophysical Journal Letters 763.

Qin, L., Carlson, R.W., Alexander, C.M.O.D., 2011. Correlated nucleosynthetic isotopic variability in Cr, Sr, Ba, Sm, Nd and Hf in Murchison and QUE 97008. Geochimica et Cosmochimica Acta 75, 7806-7828.

Seo, J.H., Sharma, M., Osterberg, E.C., Jackson, B.P., 2018. Determination of osmium concentration and isotope composition at ultra-low level in polar ice and snow. Analytical Chemistry 90, 5781-5787.

Stephan, T., Trappitsch, R., Davis, A.M., Pellin, M.J., Rost, D., Savina, M.R., Yokochi, R., Liu, N., 2016. CHILI - the Chicago Instrument for Laser Ionization - a new tool for isotope measurements in cosmochemistry. International Journal of Mass Spectrometry 407, 1-15.

Yokoyama, T., Fukami, Y., Okui, W., Ito, N., Yamazaki, H., 2015. Nucleosynthetic strontium isotope anomalies in carbonaceous chondrites. Earth and Planetary Science Letters 416, 46-55.

Zinner, E., 2014. Presolar grains. 2nd edition. Treatise on Geochemistry, 181–213.

Conclusion

From all the results of this doctor thesis, we reached the following conclusion.

- We developed a new two-jump dynamic method that can obtain $^{142}Nd/^{144}Nd$, $^{148}Nd/^{144}Nd$, and $^{150}Nd/^{144}Nd$ ratios simultaneously with TIMS. The analytical reproducibilities for $^{142}Nd/^{144}Nd$, $^{148}Nd/^{144}Nd$, and $^{150}Nd/^{144}Nd$ ratios in this study are ±4.1, ±6.3, and ±8.8 ppm (2 SDs), respectively, which are 1.5–4.1 times better than those obtained in previous studies.
- We confirmed the first evidence for the occurrence of the secondary instrumental fractionation in the high-precision Nd isotope measurement with the latest-generation TIMS instrument. The secondary instrumental fractionation was caused by the modification of fractionation mechanism in the ion lens system as a result of the accumulation of materials emitted from measured samples onto the surface of ion source assemblage. After the correction of the fractionation, reproducibilities for $^{142}Nd/^{144}Nd$ ratio were 1.4 times improved.
- We conducted high-precision Nd isotopic analysis on bulk aliquots of ordinary and carbonaceous chondrites by applying a high-pressure and high-temperature digestion technique to achieve complete dissolution of acid-resistant presolar grains. Our new Nd isotopic data gave the mean intercept value of −2.4 ± 4.8 ppm for regression lines in the $\mu^{142}Nd$ versus $\mu^{148}Nd$ and $\mu^{150}Nd$ diagrams, representing an identical match for the ^{142}Nd composition between chondrites and the accessible silicate Earth. The excess ^{142}Nd signature of the Earth would not necessarily require the existence of a hidden mantle reservoir with a subchondritic Sm/Nd ratio deep in

the Earth's mantle as proposed previously.

- We conducted high-precision Sr and Nd isotopic analyses on bulk aliquots of enstatite, ordinary, and carbonaceous chondrites by applying a high-pressure and high-temperature digestion technique. The Sr and Nd isotopic heterogeneities among terrestrial rocks, enstatite, ordinary, and CAI-subtracted carbonaceous chondrites are likely caused by the nebular thermal processing. This process could selectively destroy the recycled silicates possessing *s*-process depleted signature in the inner Solar System. The Sr and Nd isotopic heterogeneities among each class of CAI-subtracted carbonaceous chondrites (CM, CO, and CV) are likely caused by the non-uniform incorporation of recycled silicates that were concentrated in the carbonaceous chondrites formation region due to the formation of pressure bump by Jupiter core.

Acknowledgment

I am grateful to Dr. Tetsuya Yokoyama for many instructive advices, providing the environments for all the experiment in my doctor thesis. I am also grateful to Dr. Tomohiro Usui and Dr. Makiko Haba for many useful advices and constructive discussion. National Institute of Polar Research (NIPR) is thanked for providing meteorite samples. I also thank Dr. Kenji Notsu for providing meteorite samples. Saya Kagami contributed to the development of Nd isotopic measurements in Chapters 2–5. Kei Sugimoto contributed to the development of Sr isotopic measurements in Chapter 5.

I am also grateful to staffs, students, and graduates in Yokoyama laboratory throughout my Ph. D. course, Dr. Yusuke Fukami, Dr. Asobo Nkengmatia Elvis Asaah, Dr. Satoki Okabayashi, Dr. Yuichiro Nagai, Dr. Wataru Fujisaki, Dr. Nao Nakanishi, Dr. Kunihiro Myojo, Dr. Hisashi Asanuma, Dr. Ryota Moriwaki, Saya Kagami, Minato Tobita, Masashi Shidare, Gaku Tanabe, Kei Sugimoto, Mayu Nakamura, Tomoya Baba, Yusuke Morimitsu, Iori Kajitani, Motoi Okada, and Yuki Masuda for many useful comments and technical supports.